Towards optical readout of spin-states in Si:Se^+

by

Camille Bowness

B.Sc., McGill University, 2016

Thesis Submitted in Partial Fulfillment of the
Requirements for the Degree of
Master of Science

in the
Department of Physics
Faculty of Science

SIMON FRASER UNIVERSITY
Fall 2018

Approval

Name:	**Camille Bowness**
Degree:	**Master of Science (Physics)**
Title:	**Towards optical readout of spin-states in Si:Se$^+$**
Examining Committee:	**Chair:** Malcolm Kennett Associate Professor
	Stephanie Simmons Senior supervisor Assistant Professor
	Michael L. W. Thewalt Supervisor Professor
	David Broun Internal examiner Associate Professor
Date Defended:	**November 28, 2018**

Abstract

The demonstration of a qubit system in silicon, with efficient optical control and readout of robust electronic and nuclear spin states, would change the current dominant industrial trends in quantum devices. Singly ionized deep double donors in silicon (Si:Se^+) have shown promise as examples of such industry-changing qubit candidates. The Si:Se^+ system possesses a long-lived spin qubit with photonic access through a spin-selective optical transition. Under the assumption that this optical transition is radiatively efficient, it has been proposed that this optical transition be exploited for direct emission-based spin-state readout, or alternatively used as a much-sought-after silicon-integrated single-photon source. In the first part of this thesis, we present the measurement of the T_1 lifetime of the optically excited state which in turn allowed us to determine a natural radiative efficiency of 0.80(1)%. Fortunately, this spin-photon interface can be coupled to photonic cavity modes for indirect spin-state read-out or to improve the emission rate through the Purcell effect. In the second part of this thesis, we present the hardware and software details of an adaptable automated photonics testing system that can be used to characterize integrated photonic devices.

Keywords: quantum information, concentration modulation spectroscopy, silicon photonics, automated testing

Dedication

To my Nonna, my Nonno, my Granny, my Grandpa.
Your struggles gave me the opportunities I have today, this is for you.

Acknowledgements

I would like to respectfully acknowledge that SFU is on unceded Coast Salish Territory; the traditional territories of the Musqueam, Squamish and Tsleil-Waututh Nations.

Contributions to content: A few contributions to the content in this thesis should be acknowledged. Adam DeAbreu made the sample used to take lifetime measurements presented in Chapter 4. Alex Kurkjian took the transmission data and the microscope picture of the fibre array as presented in Section 6.1. Kevin J. Morse performed the extraction of fibre-core spacing from an image of the fibre face. He is also responsible for sourcing and constructing the 'purge box' used in RITA. A vaccuum tight optical fibre feedthrough to the FTIR spectrometer was designed by Kevin J. Morse and constructed by Ken Van Wieren. This box was used for RITA measurements with the FTIR spectrometer presented in Chapter 6. The main author on the 'chiprun.py' file presented in the appendix and discussed in Section 7.3 is Timothy S. Richards. Timothy S. Richards also designed the grating couplers and determined the optimal insertion angle.

SUPER acknowledgments: I am indebted to an amazing team of researchers that helped make SUPER a reality after a year of dreaming about it: Kevin J. Morse, Alex Kurjikan, James Klein, Laurent Bergeron, Adam DeAbreu, Timothy Richards, Camille Chartrand, Leea Stott, Stephen Harrigan, and Joshua Kanaganayagam. It would take me pages to describe the full contribution from everyone, we would not have the product that we have today were it not for you. Experiments will never be Basic again.

I have been fortunate enough to have Dr. Stephanie Simmons as my supervisor these last two years. Her guidance with respect to my project has been invaluable. Dr. Simmons' leadership, patience, and dedication towards her students fosters an incredible environment of collaboration that has allowed me to complete the work presented here. When I first sat down in her office over two years ago, she informed me that there would be a steep learning curve during my MSc. I have thankfully had her to help me navigate the most challenging parts of it.

Equally deserving of my appreciation is my co-supervisor Dr. Michael Thewalt. He spent many hours helping me in the lab, and I would still be trying to take lifetime measurements

were it not for his guidance. Never once were my questions dismissed, and they most certainly never went unanswered. Despite having worked closely with him, he remains a lab wizard in my eyes. His daily presence in the lab was both educational and inspirational.

SQT members: The sun never sets on SQT lab, and all members have played a vital role, both in and out of the lab, towards this thesis and the work presented.
Rohan Abraham: I am unsure quite how our group will function a smoothly without you around. Your company (on runs and in the (new) grotto) through this process has been almost as thesis-crucial as the long discussions on EMT, donor spins, ...and all that.
Laurent Bergeron: The 'import wizard', the 'python guy', the 'lab master', the 'beef'. Your contributions to the SUPER work were essential, as was your company through long bike rides and space-trucker voyages.
Camille Chartrand: Your help in discussions on three-level systems were indispensable to my understanding of the system. Always up to chat through some science, your enthusiasm opens up the grotto to great discussions, science and otherwise.
Adam DeAbreu: The one and only Lab Champ, you continue to inspire me with your both your intellect and your dedication. You have consistently helped me through hard conceptual problems in the lab and on the white board. Thank you for help with the helium transfers, the math, the python, the edits, the coffee, the gifs (hard g).
Daniel Higgenbottom: You swept in here very recently, but your help many edits and conversations about my thesis and the weekend writing company has been very much appreciated!
Alex Kurkjian: After working hard with me on both RITA and SUPER, you continued to help me, despite your own hectic schedule, with edits and references, and all around support. Thank you, for your time both in and out of the lab, your friendship has been just as crucial as your edits. RIP Experiment Basics.
Kevin Morse: This thesis would not exist were it not for your help. You have been there to help from day one, with seemingly infinite patience for repeated questions. I cannot count how many times I've swiveled my chair around to ask 'Hey Kevin can I ask you a question?'. I tried listing all the things you helped me with, but I had no space left for science.
Timothy Richards: The thoughtfulness you bring to your work carries over to the contributions you have to the group. I appreciate not only our long discussions on photonics, that have been integral to this work, but also all the wild tangents our discussions took in between, often a needed reprieve from the daily grind.

There has be an enormous number of people who have been absolutely indispensable on my path to graduate school but I only have space to thank those closest to my academic path. Caryn Cameron, thank you for the grammar and spelling edits early on in the thesis project as well as the blankets, the pillows, and the help with laundry when I first moved here. A big thank you to my first coaches, Anne Lockwell and Lyne Piche, thank you for

not only tolerating my academic career but actively encouraging me to pursue it and never letting me believe that I had to choose. Francois Laurin, were it not for kind words over long workouts I may never have applied to graduate school in the first place. Jamal Zigby, you made an impact on a young student in high school physics back in 2008, and 10 years later she is submitting her MSc thesis. You may not always know the impact you have, but I can assure you it is an important one.

Nathan Smith, who would have thought that your decision to help me solve an ODE five years ago would have led to you helping me check over an ODE I needed to solve for my MSc. Thankfully this time we weren't in a cramped stairwell before class, but in our apartment that you graciously kept together as a home during the wild tornado of thesis time. Thank you for your seemingly infinite patience, for the warm meals waiting for me after late nights and weekends spent in the lab, and for your active interest in the details of my projects. My appreciation of your support could never be overstated. Thank you.

Finally, I must thank my family. Rita Crivici (Mom), David Bowness (Dad), and Damian Bowness (person I had to share attention with). It's quite difficult to express the depth of gratitude I feel for having been lucky enough to call the three of you my family. Thank you for every e-mail you helped me edit, every late night phone call to help me get through the stressful days, the care packages, the cute animal videos, the endless debates. Thank you for fostering the sense of curiosity that lead me here, you have been the most important influences in my life. Thank you for always supporting me. It has made all the difference.

Table of Contents

List of Tables

List of Figures

Chapter 1

Introduction

1.1 Quantum computers

Quantum computers allow for a fundamentally new type of computing compared to today's classical computer. In classical computers, transistors carry information in a binary state of either 'logical high', 1, or 'logical low', 0. Calculations are performed using logic gates to process the information. Quantum computers, on the other hand, use 2-level quantum systems called qubits to carry information. The advantage of quantum computers over classical computers rests in their ability to perform 'quantum algorithms', step-by-step processes that exploit the non-classical properties of qubits. In theory, quantum algorithms can be used to solve classically intractable problems [1, 2]. To implement a quantum algorithm, a viable qubit system must accommodate initialization (preparation of a qubit in a target quantum state), readout (measurement of the quantum state projected onto a '1' or '0'), single-qubit gates (manipulation of the 2-level quantum state), and inter-qubit coupling schemes (multi-qubit gates) [3]. These operations must be fast enough to occur within the qubit's coherence time—the time it takes for the qubit's stored information to be lost.

Quantum information is stored in non-equilibrium states. Decoherence from these states can occur in two ways: first, we lose information as a distribution of states decays to thermal equilibrium [4]. This has a characteristic timescale called T_1. Secondly, local field fluctuations cause 'dephasing' of the quantum state with characteristic timescale called T_2 [4]. Information can be encoded onto multiple degrees of freedom and each degree of freedom will have distinct T_1 and T_2 coherence times [5]. A discussion on the distinction between T_1 and T_2 is presented in Chapter 2. To date, many candidate qubits have been proposed and characterized including superconducting flux qubits [6, 7], trapped ions [8, 9], photons [10, 11], and defects in semiconductors and insulators [12–18]. Many of these systems have shown success at the small scale. Efforts to scale-up these systems are underway, however, to-date, none have irrefutably demonstrated a scalable architecture for quantum processing that simultaneously achieves long coherence times, a robust readout method, and fast, high fidelity gates [3].

1.2 Donors in silicon

One class of candidate qubits are atomic defect sites in silicon [19]. One type of defect that can occur in silicon is a substitutional defect where one element in a lattice is replaced by a different element [20]. Group V substitutional defects in silicon (a Group IV element) have an extra electron that can be ionized and 'donated' to the lattice [20]. Conversely, Group III substitutional defects have an extra hole that can 'accept' an electron from the lattice [20]. Under specific temperature and pressure conditions the extra electron from a donor can remain bound to the donor site with an approximately hydrogenic energy-level structure [21, 22]. The nuclear and electron spin degrees of freedom of such a system have the potential to be exploited as qubits [23].

Kane first proposed using the nuclear spin state of a phosphorus (^{31}P, nuclear spin 1/2) donor as a qubit in his 1998 seminal paper [23]. Exploration of Kane's proposed architecture revealed experimental challenges impeding large scale operation [19, 24]. Other donor systems are being investigated in an effort to avoid these challenges [25]. One promising proposal involves Group VI chalcogen 'deep' double donors in silicon with large binding energy on the order of a few hundred meV [26]. Double donors have two bound electrons, one or both of which may be ionized [22]. When a silicon sample has both double donors and acceptors, the acceptors 'compensate' the double donors by ionizing one of the bound electrons [27]. A compensated system of 'singly-ionized' double donors occurs when the donor sites are left with only one bound electron [28]. Singly-ionized selenium in silicon (Si:Se^+), has shown particular promise as a candidate qubit [29, 30]. The spin degrees of freedom hosted by this system have been shown to have long coherence times and fast manipulation times [29]. Moreover, Si:Se^+ has an optical degree of freedom due to the large splitting between the orbital states of the bound electron [26]. The wavelength of the ground to first excited state orbital transition of the Si:Se^+ donor-bound electron is in the mid-infrared (MIR) [26]. Si:Se^+ has a hyperfine-split ground state which forms a two-level spin qubit [25]. Under the right conditions, discussed in Chapter 2, the hyperfine-split ground state can be resolved optically [26]. A discussion of the orbital, optical, and spin characteristics of Si:Se^+ is presented in Chapter 2.

1.3 Thesis motivation and outline

Detection of the emitted light from the first excited state to ground state orbital transition of the Si:Se^+ bound electron could be a direct way of measuring the state of the spin qubit. Specifically, the Si:Se^+ system may permit the direct optical readout of spin states using techniques previously demonstrated in the nitrogen-vacancy (NV^-) centre in diamond [31]. Direct optical readout requires a transition with a high radiative efficiency where the dominant decay mechanism is photon emission [32]. However, even for an efficient transition, direct optical readout would be practically impossible unless the Si:Se^+ optical degree of

freedom has a 'cycling transition' that would permit using multiple photons to reveal the original spin state of the system. For example, in NV^- centres, the radiative efficiency is dependent on the initial spin-state of the system. Furthermore, many engineering challenges would also need to be overcome in order to use a direct optical readout scheme including fabrication of high efficiency single photon detectors at the transition energy.

Previous experiments have determined the radiative lifetime of the Si:Se^+ optical degree of freedom to be 0.90(7) µs and a lower bound on the natural T_1 lifetime of 5.5 ns [30]. If the decay mechanisms were 100% radiative then we would expect the natural T_1 lifetime to match the radiative lifetime of 0.9 µs. The goal of the work presented in Part I of this thesis was to directly measure the optical T_1 of the Si:Se^+ system and hence determine the radiative efficiency. To this end we were successful and determined a lifetime of 7.7(4) ns corresponding to a radiative efficiency of 0.80(9)%. The theory behind the T_1 measurement method is described in Chapter 3 and a full discussion of the experimental details and results are presented in Chapter 4.

Low radiative efficiency necessitates alternative methods to directly measure the spin degree of freedom by way of the optical degree of freedom. Fortunately, optical degrees of freedom in silicon naturally lend themselves to be used within an integrated photonics architecture. The strong light-matter interactions of the specific Si:Se^+ optical transitions of interest mean that these donor sites can couple to photonic crystal cavity and waveguide modes to enhance the spontaneous emission rate according to the Purcell effect [33–36]. This process is described in more detail in Chapter 5. Cavity-coupled spin degrees of freedom can be exploited within a quantum circuit architecture and as optical switches within an all-optical computing architecture [34, 37, 38].

Silicon photonic devices at near-infrared (NIR) wavelengths are employed extensively within the telecoms industry with established designs for basic and complex devices [39–41]. However, photonic devices operating at 2900 nm, the wavelength of the Si:Se^+ orbital transition of interest, remain largely unexplored [42, 43]. Simulation software for photonics is readily available [44], yet, fabrication techniques for structures operating in the MIR on non-standard substrates better suited for 2900 nm operation, have not been optimized. The first step towards cavity-qubit coupling and all optical switches is to develop a technique for efficient, high-volume characterization of silicon photonic devices. To this end, we constructed and automated a measurement station for photonics in the mid-infrared, discussed in detail in Chapters 6 and 7.

Part I

Si:Se^+ excited state lifetime measurement

Chapter 2

Fundamentals of Si:Se$^+$

Singly ionized selenium donors (Si:Se$^+$) in silicon have demonstrated promising spin characteristics with applications in a quantum computing network as a qubit [29]. One promising characteristic of Si:Se$^+$ is the optical degree of freedom that can be used to initialize and readout the state of the spin degree of freedom. This chapter presents the background theory of the Si:Se$^+$ system and is broken down as follows: Section 2.1 briefly discusses relevant electronic properties and terms. Section 2.2 presents a detailed picture of the energy spectrum of singly-ionized selenium donors in silicon. Section 2.3 presents a description of lifetimes and coherence times of two-level quantum systems. Section 2.4 presents the relevant spin characteristics of Si:Se$^+$ that motivated the interest in this system as a potential qubit. Section 2.5 presents the relevant optical properties of Si:Se$^+$.

2.1 Electronic properties

To determine the radiative efficiency of the optical two-level system in Si:Se$^+$, described briefly in Chapter 1, we probed the system with light at optical frequencies [45]. Determining a viable experimental procedure that measures the lifetime of the optical excited state requires an understanding of the electronic energy levels available to electrons bound to singly ionized selenium subsitutional donors in silicon.

The 'conduction band' is the collection of energy eigenstates available to mobile electrons. The 'valence band' is the collection of energy eigenstates available to mobile holes. The 'band gap' represents the energy difference between the lowest energy conduction band states and the highest energy valence band states [20]. Bound electron states of a subsitutional donor are localized states of a donor electron around the nucleus of the substitutional site. These bound states have energies within the band gap [46]. The bound electronic states of singly ionized selenium in silicon are presented in the next section.

2.2 Level structure

We are interested in the energy and degeneracy of available donor-bound electron states in Si:Se^+. These characteristics are effected by the electrostatic Coulomb force between valence electron and nucleus, and interactions with the surrounding lattice [47] . The energy levels of a system are given by the eigenvalues of the system's associated Hamiltonian. These energy values (E) and their associated electronic wave functions ($\psi(\mathbf{r})$) for a donor atom or singly-ionized double-donor in silicon can be approximated using effective mass theory (EMT) to solve Schrodinger's equation [21]

$$\left(-\frac{\hbar^2}{2m^*_{\mathbf{r}}}\nabla^2 + V(\mathbf{r}) + U(\mathbf{r})\right)\psi(\mathbf{r}) = E\psi(\mathbf{r}) \ , \tag{2.1}$$

where $\mathbf{r}$ is the vector from the donor nucleus or 'central cell', $\hbar$ is the reduced Planck's constant, $V(\mathbf{r})$ is the periodic potential experienced by an electron in a perfect lattice, $U(\mathbf{r})$ is the potential that arises from a substitutional defect and $m^*_{\mathbf{r}}$ is the effective mass in the direction of $\mathbf{r}$. EMT assumes the effective mass of the donor-bound valence electron is equal to the effective mass of conduction band electrons [46]. This results in donor-bound electronic wavefunctions larger than the lattice spacing. This means that EMT accurately approximates the bound-electron energy levels that have energy close to the energy of the conduction band minima, such as the higher excited states of deep donors. However, EMT is less accurate for the ground and first excited states of deep donors which have a more tightly localized wavefunction around the donor nucleus [21]. Ignoring spin, and without $V(\mathbf{r})$, this equation is analogous to Schrodinger's equation for the Se^+ atom where $U(\mathbf{r})$ is the potential felt by a charged particle in a Coulomb potential adjusted by the dielectric constant for silicon (κ) [21],

$$U(\mathbf{r}) = -\frac{e^2}{\kappa\mathbf{r}} \ , \tag{2.2}$$

where e is the charge of an electron.

Ignoring the lattice contribution of Equation 2.1 results in degenerate hydrogenic orbital state solutions. These states are labelled by their energy and symmetry, with the three lowest energy orbital states labelled '1s', '2s', and '2p' in order of increasing energy. For the purpose of this thesis, the rest of this discussion will focus on the 1s states and 2p states. The 1s and 2p states and their relative energies are illustrated in the leftmost column of Figure 2.2.

We introduce $V(\mathbf{r})$ into the Hamiltonian to account for the interaction with the surrounding lattice. Including contributions from the lattice introduces degeneracy in the orbital states from k-space symmetry of the conduction band. The conduction band has 6 energy minima (valleys) along the (100) lattice direction and equivalents ((-100), (010), (010), (001), (00-1)). The symmetry of the conduction band minima is illustrated in Figure 2.1.

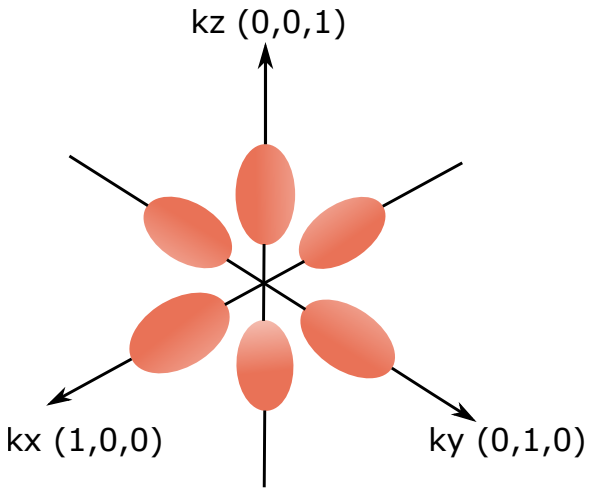

Figure 2.1: Illustration of the conduction band symmetry in k-space

This sixfold degeneracy of the 1s state is split due to valley-orbit interactions into states 1s:A, 1s:T_2, and 1s:E in increasing order of energy. The relative positions of these states are presented in Figure 2.2. We can form an approximate eigenbasis for the 1s solution to Equation 2.1 by forming linear combinations of solutions to the unperturbed periodic potential and the unperturbed coulomb potential [48]. These linear combinations take the form

$$\Psi(\mathbf{r})_j = \sum_{i=1}^{6} \alpha_i^{(j)} F_i(\mathbf{r})\phi_i(\mathbf{r}) \ , \ j = 1, 2...6 \ , \tag{2.3}$$

where the sum is over the six conduction band minima, $\phi_i(\mathbf{r})$ are the periodic Bloch wave solutions, and F_j are the hydrogenic envelope functions in each direction. The α_i coefficients can be written using the valleys in momentum-space as a basis ({kx, -kx, ky, -ky, kz, -kz})

$$\begin{array}{ll} (A) & a_i^{(1)} = \frac{1}{\sqrt{6}}(1,1,1,1,1,1) \\ (E) & a_i^{(2)} = \frac{1}{2}(1,1,-1,-1,0,0) \\ & a_i^{(3)} = \frac{1}{2}(1,1,0,0,-1,-1) \\ (T_2) & a_i^{(4)} = \frac{1}{\sqrt{2}}(1,-1,0,0,0,0) \\ & a_i^{(5)} = \frac{1}{\sqrt{2}}(0,0,1,-1,0,0) \\ & a_i^{(6)} = \frac{1}{\sqrt{2}}(0,0,0,0,1,-1) \end{array} \ . \tag{2.4}$$

The 1s:A state is an even superposition of all valley states meaning it has both an s-like envelope and s-like valley structure. 1s:T_2 states are odd superpositions of opposing valley states (e.g. kx,−kx) meaning these states are p-like in valley structure. EMT predicts that transitions between levels within 1s are forbidden. However, EMT is not a good approximation for deep energy levels, and due to the p-like substructure of 1s:T_2, the 1s:A $\Rightarrow$ 1s:T_2 transitions are symmetry allowed.

The bound electron has a spin degree of freedom that is not taken into account in Equation 2.1. Interactions between the electron spin and the conduction-band minima are called 'spin-valley' interactions.

This spin degree of freedom increases the degeneracy of the states by a factor of 2. Moreover, the inclusion of electron spin means that Equation 2.4 is no longer the eigenbasis for this system [48]. Spin-valley interactions do not effect the two degenerate 1s:A states. However these interactions split the degeneracy of the 1s:T_2 state into 1s:T_2:Γ_7 (hereafter referred to as 1s:Γ_7 in this thesis) and 1s:T_2:Γ_8 (hereafter referred to as 1s:Γ_8 in this thesis) with degeneracy 2 and 4 respectively. The relative positions of these levels are illustrated in the third column of Figure 2.2.

The symmetric 1s:A states are the only 1s states with non-zero amplitude at the donor nucleus ($\psi(0)$) [49]. When the selenium isotope has non-zero nuclear spin, the overlap induces a hyperfine interaction between the electron and nuclear spin. The hyperfine interaction splits the fourfold spin degeneracy of 1s:A into threefold degenerate triplet (T) states and a singly degenerate singlet (S) state, discussed in more detail in Section 2.4. In Si:$^{77}Se^+$ the hyperfine splitting is 6.87 µeV (0.06 cm^{-1}, 0.05 nm, 1.66 GHz) [26]. This splitting is displayed relative to the other levels in Figure 2.2.

The 2p states are well approximated by EMT [21]. EMT predicts the splitting of the 2p degeneracy into '$2p_\pm$' and '$2p_0$' due to anisotropy in the effective mass tensor.

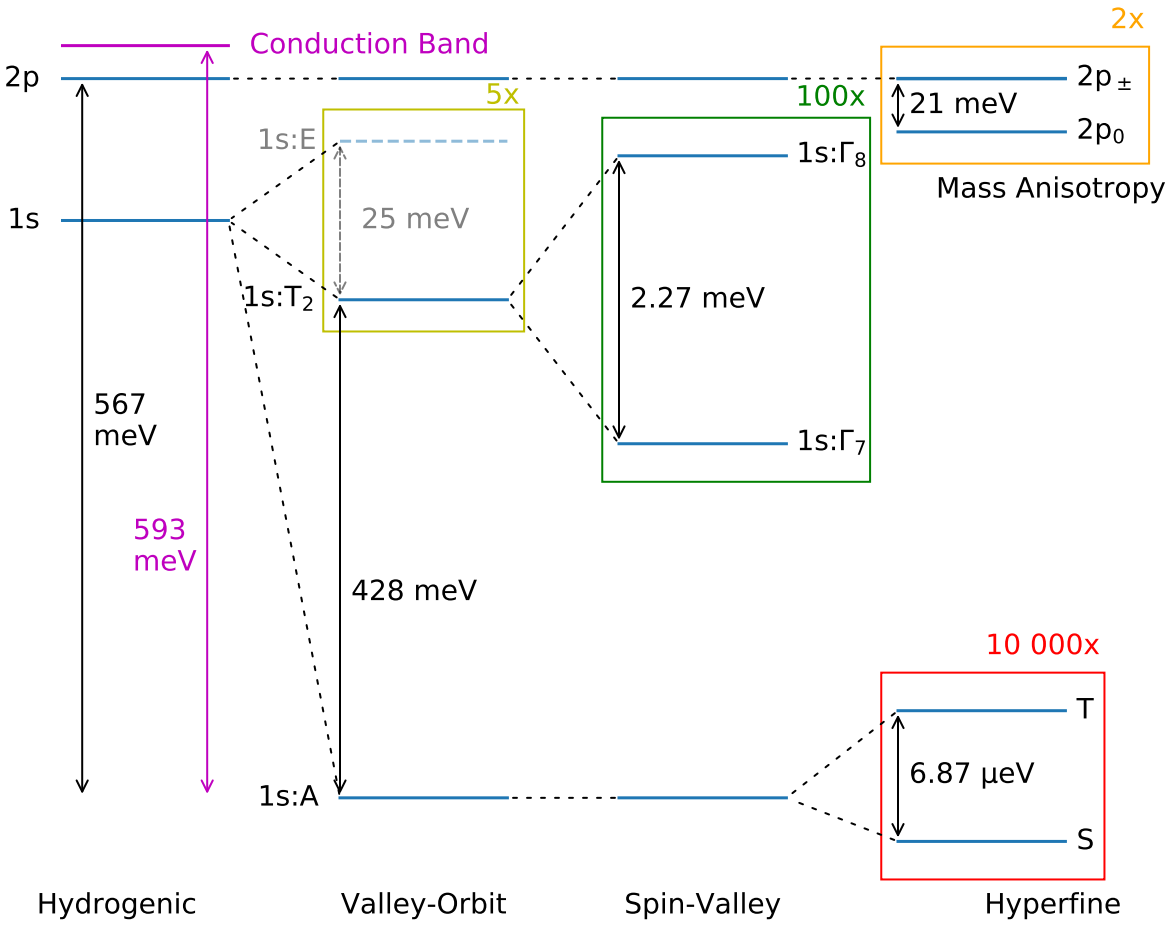

Figure 2.2: The level structure of Se^+. Valley-orbit interactions split the twelvefold degeneracy of the 1s:A state into 1s:E, 1s:T_2, and 1s:A. With the exception of 1s:E energy level (faded), all energy values displayed have been experimentally verified [22, 26, 27]. Spin-valley interactions further split the 1s:T_2 state into 1s:Γ_7 and 1s:Γ_8. The 1s:A degeneracy is lifted by a contact hyperfine interaction for selenium isotopes with nuclear spin-1/2. This results in T and S states. The degeneracy of the 2p orbital state into $2p_\pm$ and $2p_0$ is lifted dude to anisotropy in the effective mass tensor. 2s orbital states with energy levels between 1s and 2p are not shown in this diagram.

Coherent light at the transition energy, 'resonant' light, can be used to stimulate population changes between two orbital states. The energy of a transition refers to the difference in energy between the two states involved in the transition. The transition energy of 1s:A $\Rightarrow$ 1s:Γ_7 in Si:Se^+ is in the mid-infrared (MIR) band of the electromagnetic spectrum [26]. MIR has a variable definition with a range that falls between 50-1550 meV (0.8 - 25 µm) [50], for this thesis we will use MIR to refer to the region between 200-620 meV (2-6 µm). The more narrow definition of MIR is important to distinguish between MIR and near infrared (NIR) 620-1240 (1-2 µm). A range of sources, detectors, and photonics devices in the NIR are readily available compared to the MIR. The challenge of working with MIR light is a recurring theme in Chapters 4 and 6.

2.3 Bloch sphere, T_1, T_2

A two-level system can be represented geometrically by a 'Bloch sphere' [4], where one eigenstate $|1\rangle$ is at the south pole and the other eigenstate $|0\rangle$ is at the north pole, as illustrated in Figure 2.3. We can write any state on the sphere as a superposition of $|1\rangle$ and $|0\rangle$,

$$|\psi\rangle = \cos(\theta/2)|0\rangle + e^{i\phi}\sin(\theta/2)|1\rangle \ , \tag{2.5}$$

where θ is the polar angle and ϕ is the azimuthal angle as shown in Figure 2.3. We map this state onto the Bloch sphere according to the unit vector

$$\vec{r} = (\sin\theta\cos\phi, \sin\theta\sin\phi, \cos\theta) \tag{2.6}$$

A pure state is depicted by a vector of length unity, corresponding to a point at the surface of the Bloch sphere. A 50/50 mixed state, in which half the population is in state $|0\rangle$ and half in $|1\rangle$, is depicted by a vector of 0 length on the Bloch sphere [4]. Operations on a system correspond to rotations on the Bloch sphere.

An 'ensemble' of physical systems is a collection of near-identical two-level systems. We often use the term 'bulk sample' to refer to a spatial ensemble of many systems all acted upon in tandem. However, an ensemble can also refer to a temporal ensemble in which the statistical behaviour of a single system in determined through repeated interrogation. A bulk sample of two-level systems will have a thermal equilibrium distribution of states according to the temperature and energy splitting of the two-level system. Any non-equilibrium distribution will then decay back to this thermal equilibrium distribution. For example, an ensemble may have a thermal equilibrium distribution of states that are half $|0\rangle$ and half $|1\rangle$. If this system is polarized so that the entire population is in state $|0\rangle$, the population of $|0\rangle$ states will decay exponentially back to the half-half distribution. This is depicted on the Bloch sphere as a decrease in vector-length along the quantization axis as illustrated in

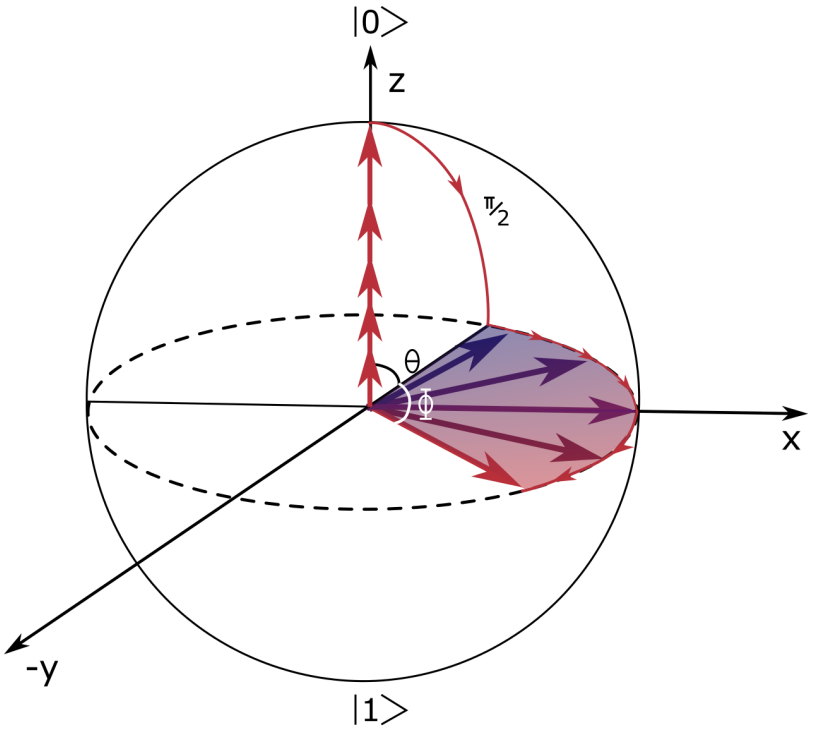

Figure 2.3: A two-level system can be represented geometrically with states on a sphere, where the excited state $|0\rangle$ is at the north pole, and ground state $|1\rangle$ is at the south pole. T_1 can be illustrated by a decay in the radial direction. T_2 can be illustrated by decoherence in the equatorial plane.

Figure 2.3 as a decay along the 'z' axis in red. The time it takes for the polarized population to decay by 1/e is the characteristic timescale of this process. It is referred to as the T_1 lifetime of the system [4].

An ensemble can be polarized along a direction perpendicular to the quantization axis in a superposition state described by Equation 2.5. This ensemble superposition state will decohere as the phase, ϕ, changes for different members of the population and the ensemble polarization becomes increasingly mixed. This behaviour, referred to as 'dephasing', is illustrated in colour in Figure 2.3 as a 'fanning out' of states in the xy plane of the Bloch sphere. The time it takes for 1/e of an initially polarized population to dephase is the characteristic time scale of this process. This characteristic timescale is called the 'pure' dephasing time, T_2^* [51].

The experimental procedure to initialize, manipulate and readout the state of a system varies across physical systems. For example, a spin-1/2 particle forms a two level system with 'spin-down' $|1\rangle$ states and 'spin-up' $|0\rangle$ states. In this system, we can initialize, manipulate, and read out spin states using radio-frequency (RF) magnetic field pulses. Application of an RF field, perpendicular to the quantization axis, with frequency equal to the transition

frequency between the spin-up and spin-down state will rotate the state on the Bloch sphere [4]. For example, RF field applied in the 'x' direction in Figure 2.3 to a system initially polarized along z will result in a rotation in the zy plane. The length of the pulse determines the angle of rotation. We refer to RF pulse that result in rotations of 90° on the Bloch sphere as '$\pi/2$' pulses. A $\pi/2$ pulse from a population of $|0\rangle$ states into a superposition state along 'y' is shown in Figure 2.3. RF pulse sequences can be used to manipulate ensembles of spins between initialization and readout in a way that increases the coherence time [52]. The characteristic time scale of natural dephasing will not change but the effective decoherence time will. This effective decoherence time is called T_2 and will often be quoted with the particular pulse sequence that was used. T_2 is bounded by T_1 according to [53]

$$T_2 \leq 2T_1 \ . \tag{2.7}$$

In order to leverage a qubit's quantum behaviour, operations must be performed within the lifetime of a qubit, limited by whichever is shortest in a specific system between T_2 and T_1. These characteristic timescales are therefore important metrics when characterizing a qubit candidate.

2.4 Spin properties

The optical ground state of Si:Se^+, 1s:A, has a spin Hamiltonian is given by,

$$\mathcal{H} = \frac{g_e \mu_B}{h} B_0 S_z - \frac{g_n \mu_N}{h} B_0 I_z + A\vec{S} \cdot \vec{I} \tag{2.8}$$

where g_e and g_n are the electron and nuclear g-factors, respectively, μ_B and μ_N are the Bohr and nuclear magnetons, respectively, h is Planck's constant, A is the hyperfine constant, and $\vec{S}$ and $\vec{I}$ are the spin operators of the electron and nucleus, respectively [29]. In the absence of a magnetic field, the spin triplet ($|\mathrm{T}\rangle$) and singlet ($|\mathrm{S}\rangle$) states are eigenstates of Equation 2.8 in Si:$^{77}Se^+$, where $^{77}Se^+$ has nuclear spin-$\frac{1}{2}$. The magnitude of this splitting is 6.87 µeV as displayed in Figure 2.2. In a small magnetic field, the triplet state degeneracy is split into three states ($|\mathrm{T}_+\rangle$, $|\mathrm{T}_0\rangle$, $|\mathrm{T}_-\rangle$). It has been proposed to use the $|S\rangle$ and $|T_0\rangle$ two-level spin-system in Earth's magnetic field as a qubit [29].

Recent efforts explored the coherence times of the $|S\rangle$ and $|T_0\rangle$ spin qubit by performing magnetic resonance experiments on bulk samples of ^{28}Si:$^{77}Se^+$ [29, 30]. Morse et al. measured a pure spin dephasing time, T_2^* of 0.91 ± 0.02 ms [29]. The authors also measured a 'Hahn-echo' T_2 of 2.14 ± 0.04 s [29], where a Hahn-echo is a dynamic decoupling sequence [54]. A follow-up study measured a spin T_1 lifetime of 4.6(1.5) hours at temperatures near 1.2 K [30]. These dephasing times and lifetime are longer than many other widely studied optically accessible solid-state centres. The promising spin characteristics of Si:Se^+ motivated further characterization of the optical properties of the system.

2.5 Optical properties

An optical two-level system can be excited from its ground state by absorbing a photon with energy (E) corresponding to the transition frequency. The energy of a photon can be expressed in terms of temporal frequency (ν), spatial frequency ($\tilde{\nu}$), angular (temporal) frequency (ω), or wavelength (λ) according to

$$E = h\nu = hc\tilde{\nu} = \frac{hc}{\lambda} = \hbar\omega \ . \tag{2.9}$$

where h is Planck's constant and $\hbar$ is the reduced Planck's constant. Frequently these quantities are used interchangeably, with common units, $[\nu]$ = MHz, $[\tilde{\nu}] = \text{cm}^{-1}$, $[\lambda]$ = nm or µm, and $[\omega]$ = rad/s. Within this text conversions will be presented where appropriate.

An optical two-level system can emit a photon when it decays from its excited state to its ground state. In an optical two level system within an electromagnetic field, the excited state has a finite lifetime, Δt. This implies a distribution of transition energies due to the time-energy uncertainty

$$\Delta E \Delta t \geq \frac{1}{2}\hbar \ . \tag{2.10}$$

For a given Δt this means that we will have range of resonant optical frequencies according to [55]:

$$\Delta\nu \geq \frac{1}{2\pi\Delta t} \tag{2.11}$$

For a single transition, the full-width-half-maximum (FWHM) of the the distribution of transition energies is referred to as a linewidth. A 'lifetime limited' transition has a linewidth dictated by Equation 2.11. In solid-state systems, at low temperatures, this is often referred to as the 'homogeneous' linewidth, where the term homogeneous arises from the similarity of the environment each oscillator experiences [5]. At high temperatures in solid-state systems, and in gaseous systems, there are additional homogeneous broadening mechanisms such as phonon-broadening, collisional broadening, or pressure broadening [5]. There are other mechanisms that can additionally broaden a linewidth as compared to its homogeneous linewidth called inhomogeneous broadening mechanisms. Inhomogeneous broadening mechanisms arise from local spatial or temporal (for a temporal ensemble) fluctuations, resulting in oscillator-specific line shapes and peak positions [5].

When an excited state decays to the ground state, energy is released from the system to the surroundings. A transition energy corresponding to an optical frequency does not guarantee that each decay from the excited state will result in the emission of a photon. For the Si:Se^+ system, decay of 1s:Γ_7 to 1s:A can happen spontaneously through purely radiative mechanisms in which only a photon is emitted or through purely non-radiative emission of one or multiple phonons (acoustic modes in a solid-state system) [56]. Spontaneous decay

can also occur as a mixture of a photon and one or more phonons, this is called 'phonon-assisted' decay [56]. The time it takes for an ensemble of optical two-level systems to decay to 1/e of the initial excited state population due to spontaneous decay mechanisms is the natural lifetime of the excited state, T_1 [57]. It is important when discussing the Si:Se^+ system in particular to note that this optical T_1 is distinct from the spin T_1 discussed in Section 2.3. Decay from an excited state can also occur due to stimulation from an external driving signal and/or from thermal and acoustic energy applied to the system [5]. The time it takes for an ensemble of optical two-level systems to decay to 1/e of the initial excited state population due to both stimulated and spontaneous decay mechanisms is the optical population recovery time τ_{pr} (distinct from the optical population recovery time T_1) [5]. The impact of stimulated decay is discussed further in Chapter 3.

The radiative lifetime (τ_{rad}) is the time it takes for a system of emitters to decay to 1/e of the initially excited population through radiative mechanisms only. τ_{rad} includes decays that are both purely radiative or phonon-assisted. The radiative efficiency of a system is characterized by the probability of radiative decay. We can determine the radiative efficiency by comparing relative decay rates of radiative decays $1/\tau_{rad}$ to total decays $1/T_1$. We can write the efficiency, ϵ_{rad} as

$$\epsilon_{rad} = \frac{T_1}{\tau_{rad}} \tag{2.12}$$

A system that decays radiatively is called an 'emitter'. Purely radiative emission will have a well defined distribution of energies or frequencies due to homogeneous and inhomogeneous broadening. The purely radiative emission distribution is called the 'zero-phonon line' (ZPL) to distinguish it from the distribution of phonon-assisted decay, called the 'phonon sideband' [58]. The emitted or absorbed light intensity as a function of energy or frequency is called a luminescence or absorption spectrum respectively.

Two transitions within a spectrum, close in energy and with similar FWHM, will only be 'resolvable' if the energy difference between the spectral peaks is larger than the FWHM of the transitions. Historically, silicon impurity transitions with separations on the order of the T and S splitting, have not been optically resolvable due to inhomogeneous broadening from variable host isotope concentrations around the defect site [26]. Specifically, the presence of ^{29}Si and ^{30}Si change the local environment of each defect site among the more abundant ^{28}Si. This means that the transition energy at each defect site may be slightly shifted due to the different masses and spin characteristics. Fortunately, previous efforts to redefine the kilogram have produced isotopically purified ^{28}Si [59]. In ^{28}Si, the 1s:A hyperfine splitting is optically resolvable [26]. In ensembles, these optical transitions can be exploited for initialization and readout of the triplet-singlet spin state [25, 29]. Direct optical readout for a single Si:Se^+ centre additionally requires the transition to be radiatively efficient.

The highest available phonon (acoustic mode) energy in silicon is approximately 65 meV, almost 7x smaller than the 1s:$\Gamma_7 \Rightarrow$ 1s:A transition energy of 428 meV [60]. This means that at least 7 phonons must be emitted for a completely non-radiative decay process due to phonons alone. The probability of a purely acoustic decay process decreases exponentially with the number of phonons required [56, 61]. Moreover, the common non-radiative decay pathway of shallow donors, the Auger-decay process does not apply to our system [32]. Therefore, upon initial inspection, a radiatively inefficient 1s:$\Gamma_7 \Rightarrow$ 1s:A transition would seem unlikely.

DeAbreu et al. measured the phonon sideband of the 1s:$\Gamma_7 \Rightarrow$ 1s:A transition in the Si:Se^+ system, showing that only 16(1)% of the radiation is emitted in the ZPL [30]. The authors further calculated a purely radiative lifetime of 5.9 µs and a total radiative lifetime including the phonon sideband (τ_{rad}) of 0.90(7) µs [30]. A 100% efficient emitter would be expected to have an optical $T_1 = \tau_{rad}$. However, Morse et al. determined a lower bound on the optical T_1 of 5.5 ns [29]. A lifetime equal to the lower bound presented in Morse et al. would indicate a radiative efficiency of only 0.6%. This inconsistency has important consequences on the applications of direct spin state readout. For comparison, nitrogen vacancy (NV^-) centres in diamond have demonstrated direct spin-based optical readout and they have been shown to have radiative efficiencies on the order of 70% [62, 63]. Given experimental challenges described more fully in Chapter 4, we used an indirect technique to measure T_1 of the 1s:Γ_7 excited state called 'concentration modulation spectroscopy'. This result allowed us to conclusively determine the radiative efficiency of the 1s:$\Gamma_7 \Rightarrow$ 1s:A transition of Si:Se^+. The theory behind this technique is presented in Chapter 3 and the experimental details and results of the measurement are presented in Chapter 4.

2.6 FTIR measurement

In this work, we use a Fourier Transform InfraRed (FTIR) spectrometer is to measure the optical spectrum of transmitted light through a a bulk sample of absorbers, emitted light from a bulk sample of emitters, or transmitted light through photonic devices. The FTIR spectrometer used in this work (Bruker IFS 125HR) is based on a two beam Michelson interferometer with four arms: a source arm, detector arm, a stationary arm, and a moving arm, depicted in Figure 2.4.

Light incident from the source arm is split by a beam splitter into the stationary and moving arm. At the end of the moving and stationary arms are mirrors, our FTIR system uses corner cubes, that reflect light back towards the beam splitter. The recombined light from the beam splitter is then incident on the detector. In an FTIR spectrometer one of the arms can move. The intensity at the detector will change as a function of the difference in length of the two arms (d). If the length of the two stationary arms is the same ($d = 0$) the light from the two arms will interfere constructively at the detector. If the moving arm

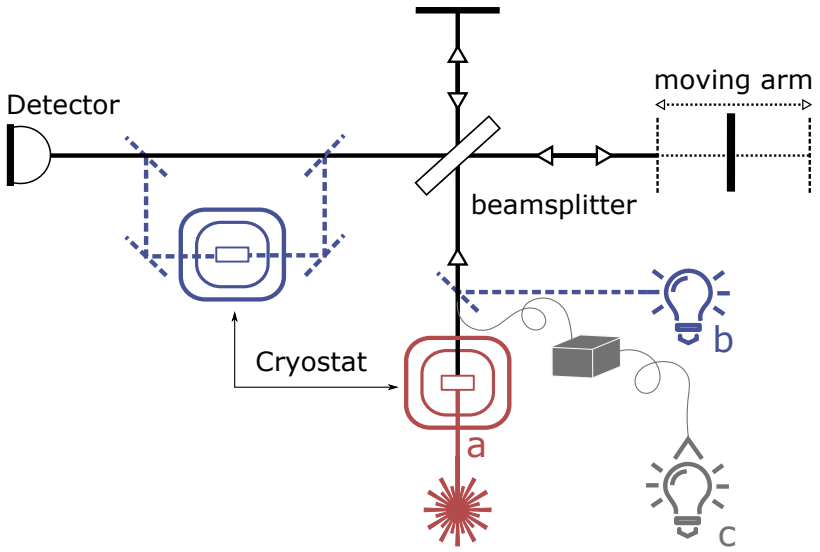

Figure 2.4: Illustration of an FTIR spectrometer. **(a):** A luminescence experiment illuminates a sample in the source arm cryostat with narrow-band light (red). The emitted light from a sample acts as the source for the interferometer and the spectrum of the luminescence signal is measured. **(b):** An absorption or transmission measurement uses a white light source internal to the FTIR set-up to illuminate a sample in a cryostat located in the detector arm. The spectrum of the transmitted light is measured. **(c):** A RITA FTIR measurement (see Chapter 6) uses a broadband infrared Supercontinuum source that couples through optical fibres into integrated photonic chip devices. The transmission through the devices is measured by FTIR to obtain a spectrum of the transmitted light through a photonic device.

is displaced from the $d = 0$ position to $d = \frac{c\tau}{2}$, where c is the speed of light in the medium of the spectrometer, the electric field at the detector E_d will be

$$E_d = \frac{E(t)}{2} + \frac{E(t+\tau)}{2} \ , \tag{2.13}$$

for incident electric field $E(t)$ and an ideal 50/50 beam splitter.

If monochromatic light is coupled into the FTIR with electric field $E(t) = \mathbb{R}\left(E_0 \exp -i\omega t\right)$ then Equation 2.14 becomes

$$E_d = \frac{E_0 e^{-i\omega t}}{2} + \frac{E_0 e^{-i\omega(t+\tau)}}{2} \ . \tag{2.14}$$

Therefore the intensity at the detector, $I_d = |E_d|^2$ is

$$I_d = \frac{I_0}{2}\left(1 + \cos\frac{2\omega d}{c}\right) \ , \tag{2.15}$$

where $I_0 = E_0^2$.

If more than one frequency of light is incident from the source arm, the intensity at the detector will be

$$I_d = \frac{I_0}{2}\left(1 + \sum_j C_j \cos\frac{2\omega_j d}{c}\right) , \tag{2.16}$$

where C_j is the fraction of total energy in frequency j.

Taking the modulus of the Fourier transform of I_d will give us the power spectrum of the incident light in frequency. With an ideal, infinite, system, we would get delta function spikes at each ω_j present in the incident light. In a real system, our resolution is limited by the length of the moving arm, the spatial coherence of the incident light, and the quality of the optics of the system.

When we take luminescence spectra, the incident light is the signal emitted from a sample, often mounted in a cryostat at temperatures below 4 K. When performing transmission measurements on bulk samples, we use the internal broadband source and a liquid helium cryostat in the detector arm. Our photonic testing apparatus, presented in Chapter 6, uses an external MIR-specific broadband source and is fibre coupled to the source arm.

Chapter 3

Concentration modulation spectroscopy

In order to determine the radiative efficiency of the 1s:A $\Leftrightarrow$ 1s:Γ_7 transition in the Si:Se^+ system, we need to determine the T_1 lifetime of the optical excited state and compare it to the known radiative lifetime (0.90(7) µs [30]) according to Equation 2.12. For clarity, references to ground and excited states in this Section refer uniquely to optical ground and excited states of the bound electron in the Si:Se^+ system, namely 1s:A and 1s:Γ_7.

The typical approach to measuring optical excited state lifetimes in two level systems is to use 'pump-probe' techniques which measure T_1 through transient detection [64]. Resonant pump-probe techniques use two pulsed radiation sources: a strong pump beam and a weaker probe beam [65]. The pump generates a non-equilibrium state within the sample by redistributing the population of excited and ground states [65]. Specifically, the pump beam will excite a subset of the ground state population to the excited state. Pump-probe techniques measure the decay rate directly by measuring changes in probe-beam transmission as a function of time-delay following the pump pulse [65]. In order to measure lifetimes on the order of 5.5 ns (the lower bound on T_1 [29]), this style of experiment requires short-pulsed sources and equally fast detectors. Unfortunately, pulsed narrowband sources and fast, sensitive, detectors are not routinely available in the MIR making this technique impractical to measure the T_1 of the 1s:Γ_7 $\Rightarrow$ 1s:A transition.

Fortunately, an alternate technique of measuring T_1, referred to as concentration modulation spectroscopy (CMS), relaxes constraints on the source and detector. CMS measures lifetime using a two-level system's response to the sinusoidal modulation of a continuous-wave, resonant signal. The steady state excited state population will depend on the period of the sinusoidal modulation of the driving signal as compared to T_1. The following sections describe the theory of CMS by deriving the population distribution as a function of modulation frequency. The final equation we derive shows that the steady-state population difference between excited and ground state populations, as a function of modulation frequency, will decay at a timescale dependent on the T_1 of the transition.

The derivation will be presented as follows: we will define the population-recovery time for an ensemble of optical two level systems and show that at low temperatures and MIR transition energies this is equivalent to T_1. Then we will introduce a resonant driving signal and derive the rate equation that describes the dynamics of a driven ensemble of two-level systems. This first part of the derivation follows the derivation in Siegman's textbook 'Lasers' [5]. We then solve this rate equation for an ensemble of two level systems illuminated with sinusoidally modulated resonant radiation. The result of this calculation is a functional relationship between the source modulation frequency and luminescence signal of the system.

3.1 Rate equations of a two-level system

In a closed ensemble of optical two level systems, decreasing the population in the ground state and increasing the population in the excited state is referred to as excitation. Excitation in a solid state system can occur through stimulation from background thermal sources. In principle, these sources can be both 'radiative', from blackblody electromagnetic radiation, or 'non-radiatve', from acoustic sources. Increasing the population in the ground state and decreasing the population in the excited state is called relaxation. Relaxation can occur through stimulation, from the same sources as excitation, or spontaneously, as described in Chapter 2.

In the absence of an external driving signal, the rate equations for ground state population (N_1) and excited state population (N_2) of a two level system are [5]:

$$\begin{aligned} \frac{dN_1}{dt} &= \left(M_{21,\mathrm{bbr}} + \gamma_{\mathrm{rad}} + M_{21,\mathrm{nr}} + \gamma_{\mathrm{nr}}\right) N_2 \\ &\equiv w_{21} N_2 \ , \\ \frac{dN_2}{dt} &= \left(M_{12,\mathrm{bbr}} + M_{12,\mathrm{nr}}\right) N_1 \\ &\equiv w_{12} N_1 \ . \end{aligned} \tag{3.1}$$

where M_{ij} is the stimulated transition rate from state i to state j due to blackbody electromagnetic radiation *bbr* or non-radiative sources nr, and γ_{rad}, γ_{nr} are the spontaneous radiative and non-radiative decay rates respectively. To satisfy conservation of energy, the stimulated transition rates for excitation and relaxation of each type of transition must be equal. Namely,

$$M_{12,nr} = M_{21,nr} \quad \text{and} \quad M_{12,bbr} = M_{21,bbr} \ . \tag{3.2}$$

The total rate of spontaneous decay is given by

$$\gamma_{rad} + \gamma_{nr} = \gamma_{tot} \tag{3.3}$$

We define the population recovery time τ_{pr} as

$$\frac{1}{\tau_{pr}} \equiv w_{12} + w_{21} \tag{3.4}$$

By the principle of detailed balance, when the sample and surroundings are at thermal equilibrium in the absence of a driving signal, the ratio between excitation and relaxation rates are given by the Boltzmann factor,

$$\frac{w_{12}(\text{excitation})}{w_{21}(\text{relaxation})} = \frac{g_2}{g_1} \exp\left(\frac{(E_2 - E_1)}{kT}\right) \ , \tag{3.5}$$

where g_i is the degeneracy of state i, E_1 and E_2 are the energies of the ground and excited state respectively, k is the Boltzmann constant, and T is the temperature of the system and surroundings. For the selenium system, the degeneracy of the ground and excited states are the same, meaning $g_2/g_1 = 1$. At the 1s:A$\Rightarrow$ 1s:Γ_7 transition energy (427 meV) and at 4 K the Bolzmann factor is very small,

$$\exp\left(-\frac{E_1 - E_2}{kT}\right) \approx \exp\left(\frac{-427 \times 10^{-3}}{8 \times 10^{-5} \times 4}\right) \approx 10^{-580} \ . \tag{3.6}$$

Which implies

$$M_{12,bbr} + M_{12,nr} \ll M_{21,\text{bbr}} + \gamma_{\text{rad}} + M_{21,\text{nr}} + \gamma_{\text{nr}} \ . \tag{3.7}$$

By equation 3.2, this means

$$\frac{1}{\tau_{pr}} \equiv \omega_{12} + \omega_{21} \approx \gamma_{tot} \equiv \frac{1}{\mathrm{T}_1} \ , \tag{3.8}$$

for T_1 the natural lifetime of the excited state due to spontaneous decay as defined in Chapter 2.

To properly model the system that we will be using in our CMS experiment we need to introduce an external driving signal. We denote W_{ij} the signal-induced stimulated transition rate between state i and j. Equation 3.1 becomes

$$\begin{aligned} \frac{dN_1}{dt} &= -W_{12}N_1 + (W_{21} + w_{21})\, N_2 \\ \frac{dN_2}{dt} &= W_{12}N_1 - (W_{21} + w_{21})\, N_2 \ . \end{aligned} \tag{3.9}$$

In a two level system with fixed total population we can combine the rate equations for the populations of each individual energy level into a single differential equation for the difference in population $(N_1 - N_2) = \Delta N(t)$. Using the fact that signal-stimulated transition probability $W_{12} = W_{21}$, we get [5]

$$\frac{d}{dt}\Delta N(t) = -2W_{12}\Delta N(t) - (w_{12} + w_{21})\left(\Delta N(t) - \Delta N_0\right) \tag{3.10}$$

where ΔN_0 is the equilibrium population difference. The factor of 2 in the first term of equation 3.10 comes from the fact that a decrease in population of the ground state by 1 increases the population of the excited state by 1 and changes the difference in population by 2. Applying our definition of T_1 from Equation 3.4 we arrive at a linear inhomogeneous differential equation in $\Delta N(t)$,

$$\frac{d}{dt}\Delta N(t) = -2W_{12}\Delta N(t) - \frac{\Delta N(t) - \Delta N_0}{\mathrm{T}_1} \ . \tag{3.11}$$

3.2 Solution to rate equation

To determine the effect of a sinusoidally modulated driving signal we assume the form of the stimulated transition rate to be

$$W_{12} = W_a + W_b \cos\omega_m t \ . \tag{3.12}$$

where [5]

$$W_{12} \ll W_{12}^{sat} = \frac{1}{2\mathrm{T}_1} \ , \tag{3.13}$$

for saturation transition probability W_{12}^{sat}. We assume a similar form for $\Delta N(t)$

$$\Delta N(t) = N_a + N_b(t) \tag{3.14}$$

Substituting the functional form of W_{12} and $\Delta N(t)$ from Equations 3.12 and 3.14 into Equation 3.11 we get

$$\begin{aligned}\frac{d}{dt}\Delta N_b(t) = &- 2N_aW_a + \frac{\Delta N_0 - N_a}{\mathrm{T}_1} - 2N_aW_b\cos\omega_m t \\ &- \left(2W_a + 2W_b\cos\omega_m t + \frac{1}{\mathrm{T}_1}\right) N_b(t) \ .\end{aligned} \tag{3.15}$$

By 3.13

$$W_a + W_b \ll \frac{1}{2\mathrm{T}_1} \ , \tag{3.16}$$

and we get

$$\frac{d}{dt}\Delta N_b(t) \approx -2N_aW_a + \frac{\Delta N_0 - N_a}{\mathrm{T}_1} - 2N_aW_b\cos\omega_m t - \frac{N_b(t)}{\mathrm{T}_1} \ . \tag{3.17}$$

We can solve this differential equation using the method of integrating factors with solution

$$\begin{aligned} N_b(t) = &(-2N_aW_aT_1 + \Delta N_0 - N_a)\,(1 - \exp -t/\mathrm{T}_1) \\ &- \frac{2N_aW_b}{\omega_m^2 + (1/T_1)^2}\left[\omega_m \sin\omega_m t + (1/\mathrm{T}_1)\cos\omega_m t - (1/\mathrm{T}_1)\right] \ . \end{aligned} \tag{3.18}$$

This implies that the frequency-dependent response of the system when compared to the input signal has amplitude, R,

$$\mathrm{R}(\omega_m) = \frac{2N_aW_b\mathrm{T}_1}{\sqrt{1 + (\omega_m\mathrm{T}_1)^2}} \ , \tag{3.19}$$

and phase ϕ

$$\phi(\omega_m) = \tan^{-1}(\omega_\mathrm{m}\mathrm{T}_1) \ . \tag{3.20}$$

3.3 Interpretation of the physical system

Equation 3.18 has important implications when we consider the physical set-up of a sample illuminated with sinusoidally modulated driving signal according to Equation 3.12, with constraints on power given by Equation 3.13. In this circumstance, the luminescence signal from radiative decay would be proportional to the instantaneous population of excited states. If the luminescence signal from this sample is collected using a phase-sensitive detection method with reference frequency ω_m, we would expect to see the amplitude of this signal, A, change as

$$A(\omega_m) \propto R(\omega_m) = \frac{2N_aW_bT_1}{\sqrt{1 + (\omega_m T_1)^2}} \tag{3.21}$$

and phase delay defined by Equation 3.20.

As described in Chapter 4, a lock-in amplifier can be used to perform phase sensitive detection to an external reference frequency, in this case the sinusoidal modulation frequency. Therefore, we can monitor A and ϕ as functions of ω_m as long as the detector is faster than the modulation frequencies. With a lower bound on the T_1 of 5.5 ns, this requires source modulation and detector frequencies on the order of 30 MHz, an easier constraint to meet in the MIR than the narrow-band, nanosecond pulsed sources required for pump-probe methods. CMS can be implemented using a continuous-wave single frequency source with commercially available acousto-optic modulators.

Chapter 4

Measuring the excited state lifetime of Si:Se$^+$

In this chapter we present the CMS measurement of the excited state lifetime of the 1s:A $\Leftrightarrow$ 1s:Γ_7 transition. Here we will refer to 1s:A as the ground state and 1s:Γ_7 as the excited state. Section 4.1 presents the assumptions that we made about our system and how well it approximates the ideal two-level system used in the derivation of CMS (see Chapter 3). Section 4.2 presents a description of the sample used for all measurements. Section 4.3 presents a description of the experimental set-up. Section 4.4 presents the measurement procedure and results including a description of the different sources of noise and how they were removed from our signal in post-processing. Section 4.5 presents an interpretation of these results with regards to the viability of direct optical readout of the triplet and singlet spin states in Si:Se$^+$.

4.1 Assumptions

Our measurement used a sinusoidally modulated source resonant with the 1s:A $\Rightarrow$ 2p$_\pm$ transition instead of driving 1s:A $\Rightarrow$ 1s:Γ_7 directly for experimental reasons described in Section 4.3. This means our system deviates from the isolated two-level model presented in Chapter 3. In order to remain consistent with the theory developed in Section 3.1, we make the following assumptions about our system.

First, we assume that 2p$_\pm$ decays to 1s:Γ_7 on a timescale much faster than the T$_1$ of the 1s:Γ_7 $\Rightarrow$ 1s:A transition. The energy of the 1s:Γ_7 $\Leftrightarrow$ 2p$_\pm$ is approximately 139 meV, with a number of intermediate states (1s:Γ_8, 1s:E, 2p$_0$, 2s, etc). The highest energy phonon mode in silicon is approximately 65 meV [60]. This transition therefore corresponds to a 2-3 phonon transition. Phonon transitions of 3 or less are typically associated with lifetimes on the order of picoseconds [66]. This means that our lower bound on the 1s:Γ_7 $\Leftrightarrow$ 1s:A liftetime of 5.5 ns [30] is 1000x larger than our estimated 1s:Γ_7 $\Leftrightarrow$ 2p$_\pm$ transition.

CMS measures the limiting (longest) lifetime of the multilevel system that includes 1s:Γ_7. Therefore, if this assumption is invalid, our measurement is not a true lifetime but only an upper-bound on T_1 of the 1s:$\Gamma_7 \Rightarrow$ 1s:A transition. The 5.5 ns determined by Morse et al. remains a known lower bound [29].

As a consequence of our first assumption, we can assume that incident powers that do not saturate the 1s:$\Gamma_7 \Leftrightarrow$ 1s:A transition will not saturate the 1s:$\Gamma_7 \Leftrightarrow 2p_\pm$ transition. The saturation power decreases with increasing lifetime, therefore a much shorter 1s:$\Gamma_7 \Leftrightarrow 2p_\pm$ transition lifetime would indicate much higher incident powers to achieve saturation. Recall, CMS requires the source populating 1s:Γ_7 to be operating at low powers compared to the power required to achieve saturation of the two level system.

Lastly, we assume the 'branching ratio', the ratio of $2p_\pm$ decays that populate 1s:Γ_7 compared to any other state, is independent of the modulation frequency of the source.

4.2 Sample

To perfrom CMS, we need a sample with large enough concentration to give us a detectable luminescence signal with below-saturation radiation powers. The sample should ideally have no hyperfine splitting of the 1s:A optical ground state. If the energy difference between the T and S states of 1s:A (see Figure 2.2) which is larger than the linewidth of our source, the sample will become hyperpolarized in either the T or S state causing our luminescence signal to decay according to the time scale of hyperpolarization and not of the excited state lifetime.

We used a polygon shaped wafer sample of natural selenium doped natural silicon (^{nat}Si:^{nat}Se) with dimensions shown below in Figure 4.1. The effects of isotopic impurities will be more prominent in ^{nat}Si compared to that of ^{28}Si. Isotopic broadening is an inhomogeneous broadening mechanism which causes the spectral peaks from a ^{nat}Si:^{nat}Se sample to appear broader than those from a ^{28}Si:^{nat}Se sample with minimal silicon isotopic impurities [26]. However, the T_1 of each of these emitters remains the same regardless of host isotope concentration and the modulation frequency response of the system remains unchanged.

We illuminated only a small portion of the sample, indicated by the red circle in Figure 4.1. The luminescence signal strength will depend on the concentration of emitters and the incident radiation intensity.

The sample was prepared using a diffusion technique. Specifically, ^{nat}Se was diffused into a float-zone silicon (^{nat}Si) wafer using selenium dioxide $^{nat}SeO_2$ as a source [67]. The diffusion into the thin wafer took 7 days at 1200° C in order to achieve a near uniform concentration of Se^+. We could have, in theory, increased the luminescence signal strength by using a thicker sample. However, the slow diffusion rate of Selenium, means that a thicker sample with uniform concentration of Se^+ was not available. The sample has a uniform

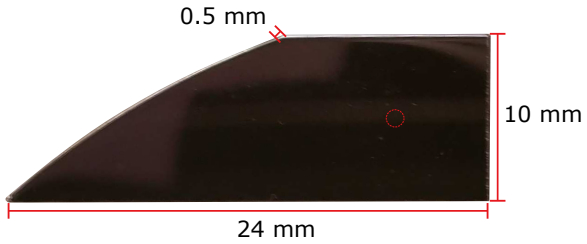

Figure 4.1: Wafer sample of ^{nat}Si:^{nat}Se. Red circle indicates approximate maximum beam size incident on sample for scale.

concentration of natural selenium of 5×10^{16} cm^{-3} with natural isotope concentrations and nuclear spin given in Table 4.1 [68]. Working with ^{nat}Se means that our sample had selenium isotopes with predominantly 0 nuclear spin.

Isotope	**Abundance (%)**	**Nuclear Spin**
^{74}Se	0.89 ± 0.04	0
^{76}Se	9.37 ± 0.3	0
^{77}Se	7.63 ± 0.16	$1/2$
^{78}Se	23.77 ± 0.3	0
^{80}Se	49.61 ± 0.4	0

Table 4.1: Isotopes of selenium

4.3 Experimental set-up

We used the experimental set-up shown in Figure 4.2 (a) and (b) to take FTIR luminescence spectra of our sample and perform CMS respectively. During all measurements the sample was kept below temperatures of 2 K in a cryostat of superfluid helium. At these temperatures, all of the population of Se^+ unpaired electrons are in the optical ground state, 1s:A.

The most direct method to populate 1s:Γ_7 would be to tune the laser source to the 1s:A $\Rightarrow$ 1s:Γ_7 transition energy to excite some of the ground state population. However, this method would make measurement very difficult since the luminescence signal would be indistinguishable amid the transmitted source radiation. Instead, we tuned the laser to a higher energy transition, 1s:A $\Rightarrow 2p_{\pm}$.

CMS requires a continuous wave source that can be used to populate 1s:Γ_7. We used an IPG Photonics CLT-2400 continuous wave, mid-infrared laser as our source. This laser is tuneable over the range 400-660 meV (1880-3050 nm, 5319-3279 cm^{-1}) [26]. The source was modulated sinusoidally by a 10 MHz bandwidth germanium acousto-optic modulator (AOM) (IntraAction AGM-802A9).

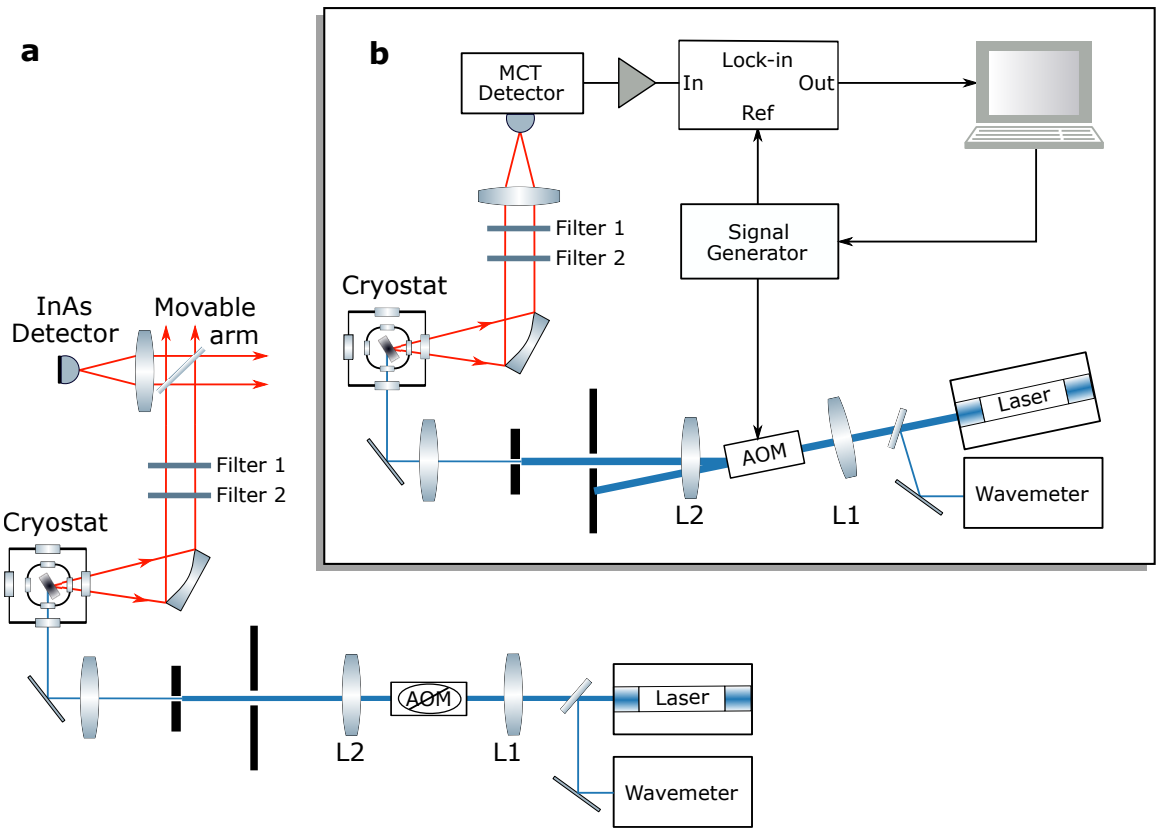

Figure 4.2: Schematic of experimental set-up. Incident laser light tuned to the Se^+ 1s:A $\Rightarrow$ $2p_\pm$ transition (4578 cm^{-1}) was focused through a lens (L1) to minimize the beam width within a 10 MHz bandwidth germanium AOM. **(a) Set-up to take FTIR spectra:** The driver to the AOM was off and the main beam was refocused (L2) into a 1 mm aperture and a vertical slit. The beam was directed to the sample immersed in superfluid Helium (< 2 K) at an angle for maximum rejection of the transmitted source signal. The luminescence signal is collected by an elliptic mirror that collimates the incoming signal through two LP filters (Filter 1: 2440 nm and Filter 2: 2850 nm) into the input arm of the Bruker FTIR spectrometer. A liquid-nitrogen cooled InAs detector was used to measure the luminescence spectrum of the sample. **(b) Set-up to perform CMS:** The first diffracted beam of the AOM was refocused (L2) into a 1 mm aperture to reject the main beam and higher order diffracted beams. A vertical slit was used to reject unreliably modulated contributions to the beam that come from angled edge rays incident on the AOM. The light that makes it through the slit was incident on the ^{nat}Si:^{nat}Se sample. A lock-in measurement was made using the driving frequency of the AOM as reference.

We required sinusoidal amplitude modulation of the laser signal with frequencies up to the suspected T_1^{-1}. These high modulation frequencies are necessary in order to observe a significant, here $1/\sqrt{2}$, drop in the luminescence signal compared to the signal produced when the sample is illuminated using an un-modulated source. This means that for a T_1 of 5.5 ns (the lower bound presented in Morse et al. [29]), we would ideally be able to

modulate with frequencies up to 28 MHz. The bandwidth of an AOM is limited by how fast an acoustic wave can travel across the diameter of the incident beam of light. Therefore, we were able to reliably increase the operating range of the AOM from 10 MHz to 20 MHz by reducing the spot size through the AOM. We used a converging lens pair of focal length 15 cm and 10 cm, labeled as L1 and L2, respectively, in Figure 4.2. The first diffracted beam (which sinusoidally modulates from 0-80% maximum amplitude) was isolated using a 1 mm diameter aperture. A second slit was used to block the edges of the beam that were modulated unreliably at the highest frequencies.

To perform the CMS measurement, the source was brought into resonance with the 1s:A $\Leftrightarrow$ $2p_{\pm}$ transition at 567 meV (2185 nm , 4577 cm^{-1}). We used two long pass filters, 508 meV (2440 nm , 4098 cm^{-1}) and 435 meV (2850 nm , 3508 cm^{-1}) to filter out the source signal (labeled 'Filter 1' and 'Filter 2' respectively in Figure 4.2 (b)). To confirm this configuration was successful in removing contributions from the source signal while still populating 1s:Γ_7, we took an FTIR luminscence spectrum of the sample. To obtain the spectrum, the AOM was turned off and the external collection optics were realigned to route the collected signal into the FTIR spectrometer (Bruker IFS 125HR). This configuration is illustrated in Figure 4.2 (a). We observed strong luminescence at the 1s:A $\Leftrightarrow$ 1s:Γ_7 transition while observing no signal at the 1s:A $\Leftrightarrow$ $2p_{\pm}$ transition, as shown in Figure 4.3. This figure simultaneously shows 1s:Γ_7 $\Rightarrow$ 1s:A luminescence resulting from excitation of 1s:A $\Leftrightarrow$ $2p_{\pm}$ and the successful filtering out of the source signal.

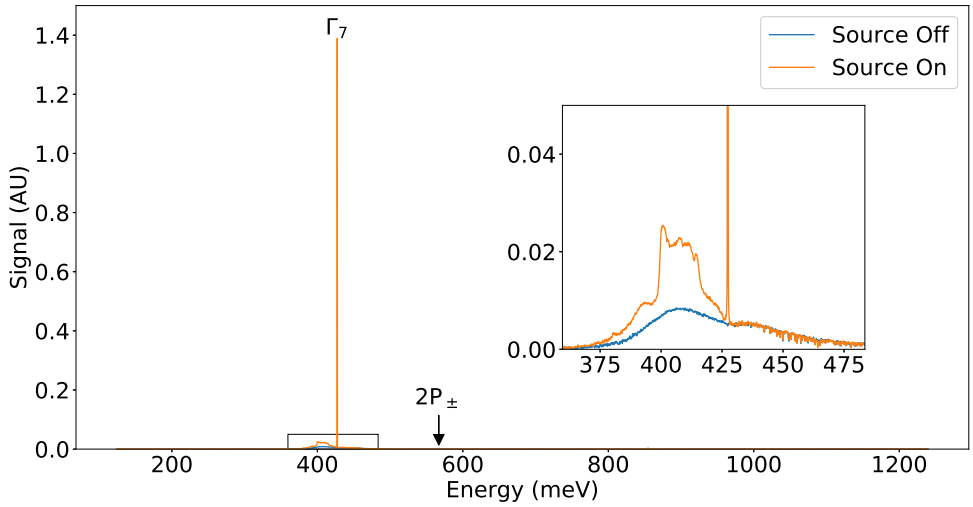

Figure 4.3: In order to verify the effect of exciting our sample at 1s:A $\Rightarrow$ $2p_{\pm}$ transition (4578 cm^{-1}) and the effect of our filters we took spectra using an FTIR spectrometer to analyze the luminescence response. We see a clear zero phonon line at the 1s:A $\Rightarrow$ 1s:Γ_7 transition as well as a phonon sideband to the left.

When the AOM was on for CMS measurements we estimated the incident power on the sample was < 400 mW over a < 1 mm diameter beam. Previous attempts to observe saturation of the 1s:A $\Leftrightarrow$ 1s:Γ_7 transition under comparable conditions were unsuccessful. Therefore, by the assumptions presented in Section 4.1, we were operating in the appropriate regime to perform CMS as described in Chapter 3.

We used a 10 kHz - 815 MHz mercury-cadmium-telluride (MCT) (VIGO PVI-4TE-3-0.5x0.5) detector. The detector compartment was evacuated and external collection optics were purged with nitrogen to reduce water absorption in the collection beam path.

A lock-in amplifier outputs a DC signal proportional to the AC signal amplitude under investigation as defined by an AC reference signal with a phase offset. For this experiment, the AC reference signal was the sinusoidal AOM driving frequency (0-20 MHz). The AC signal under investigation was our detected luminesence signal. The luminesence signal had a sinusoidal response to the input signal with an amplitude and phase relative to the reference defined by Equations 3.21 and 3.20 respectively. The source, resonant with the 1s:A $\Leftrightarrow$ $2p_{\pm}$ transition, was modulated using the AOM. We swept the modulation frequency from 0.1 to 20 MHz in 100 kHz steps. We performed a lock-in measurement at each step with the modulation frequency as reference. The lock-in amplifier measured this phase and amplitude. At each frequency step we first waited 3 seconds to allow the system to equilibrate. The lock-in amplifier was set to have a time-constant of 300 ms. The luminescence amplitude and phase value at each frequency is the average of measurements taken in a 12 second interval.

4.4 Measurement and analysis

We measured the luminesence signal response of the sample for modulation frequencies between 0.1 and 20 MHz. There were two main sources of background signal that needed to be corrected for: Radio-frequency (RF) noise from the environment and the contribution to signal decay from reduced transmission through the AOM as we increased the modulation frequency, ω_m, near and beyond its cutoff frequency.

The sensitivity of our detector to high frequency signals made it susceptible to RF pick-up, distorting our luminscence signal. The RF signal was a coherent signal, meaning it had a coherent phase with respect to the reference signal, but it did not have the same phase as the luminesence signal. The result of this noise is oscillation in the luminescence signal at high source modulation frequencies. Attempts to completely remove this noise using RF filters were unsuccessful. An example of the raw data without the RF noise removed is shown in Figure 4.4. In order to measure the contribution to the signal from RF pick-up, we swept ω_m from 0.1-20 MHz with the laser off and recorded this non-zero contribution. We subtracted the RF contribution from the luminescence signal in the complex plane to

account for the difference in phase between the phase of the RF contribution and the phase of the signal. An example of this correction is shown in Figure 4.4.

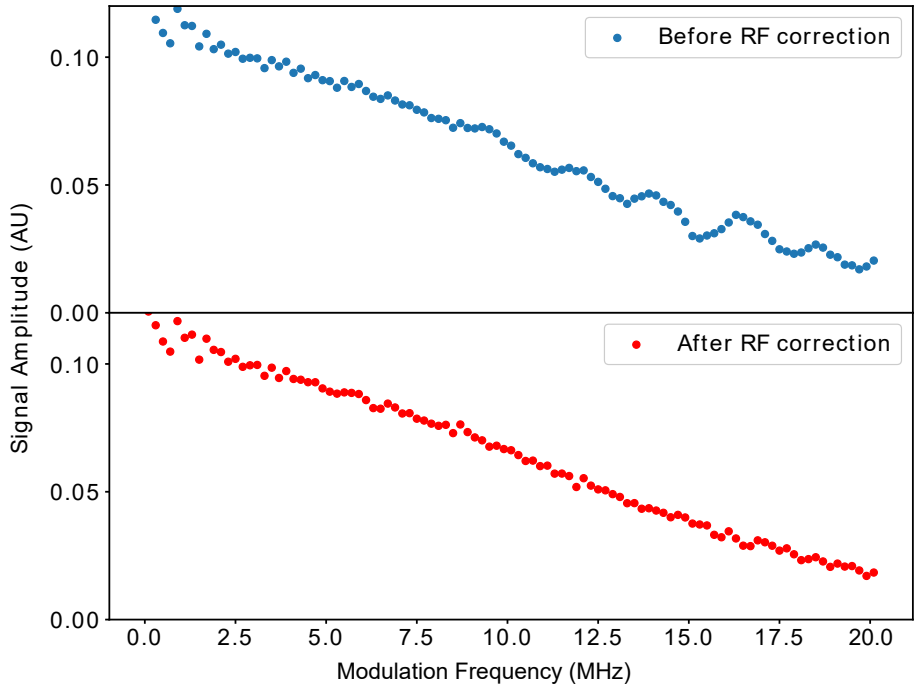

Figure 4.4: RF correction. A modulation frequency sweep was performed with the laser off measuring just the RF noise caused by the AOM driver. The top plot shows an example of a luminescence sweep before correction and the bottom plot shows the result of subtracting the RF signal from the luminescence signal in the complex plane to account for phase differences.

The modulation efficiency of the AOM decreased with increasing frequency of modulation. Therefore we collected a reference of the source through the AOM without the sample to measure the frequency response of the AOM tranmsission. We removed the sample, removed both filters and used white paper on the front and back side of the cryostat (labeled 'cryostat' in Figure 4.2 (b)) to scatter the modulated source light. This way we could keep the source at the same powers that we used during the CMS scans without saturating the detector. In this configuration, we swept the modulation frequency from 0.1-20 MHz in 100 kHz steps. The RF-corrected luminescence signal was divided by the scattered laser signal to obtain the final data that was then analyzed.

We performed the three scans (Luminescence, RF contribution, and, scattered source) five times. We performed a least-squares fit of the RF and background corrected amplitude and phase data to Equations 3.21 and 3.20 respectively. With this we extracted T_1 lifetime for the 1s:Γ_7 excited state of 7.7 ± 0.4 ns. The fit-amplitude-normalized raw data, and fits, are shown below in Figure 4.5.

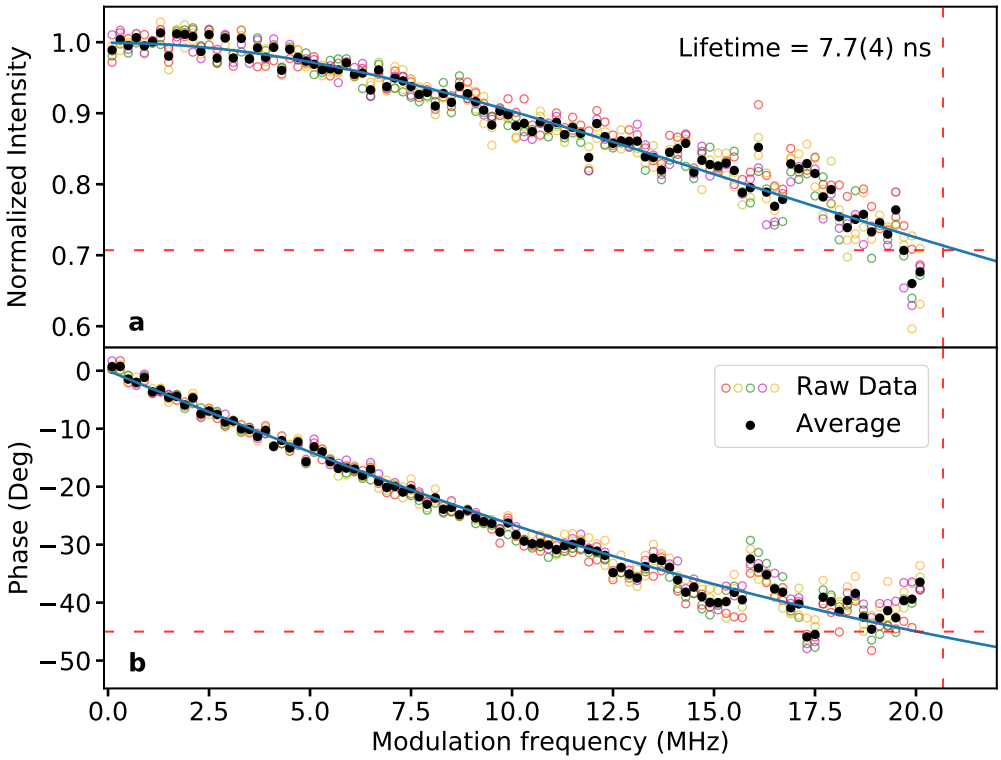

Figure 4.5: (**a**) Photoluminescence signal normalized to the low-frequency limit, fit with Eqn. 3.21. (**b**) Phase lag between the modulation frequency and the luminescence signal, fit with Eqn. 3.20. Red dashed lines intersect the data at the critical modulation frequencies in which the signal has dropped to $1/\sqrt{2}$ and phase has lagged by 45°.

4.5 Conclusions and discussion

We compare the measured T_1 with the upper bound radiative lifetime of 0.90 ± 0.07 µs [30] to get a lower bound on resonant radiative efficiency of 0.80(9)%. With 16(1)% of the overall emission spectrum in the ZPL [30], we calculate the efficiency of purely radiative photon decay to be 0.125%. These results indicate that the transition is dominated by a nonradiative process. This was unexpected given the low probabilities typically associated with the $>$ 7-phonon decay processes discussed in Section 2.5. These low efficiencies, however surprising, rule out the possibility of direct, emission based coupling and readout schemes for the Si:Se^+qubit.

Nonetheless, we can enhance the spontaneous emission rate of this qubit by manipulating the environment around it according to the Purcell effect [33, 69]. Working in silicon at optical wavelengths gives this system an advantage when it comes to engineering its environment. We can leverage fabrication methods of the emergent silicon photonics industry based on those used in the field of integrated circuit technology. Similarly, we can envision the cavity quantum-electrodynamics (cQED) architecture employing an indirect coupling approach using silicon photonic networks described in the recent proposal paper by Morse et al. Such an approach does not rely upon having a high efficiency emitter [29].

Despite extensive research into silicon photonics at telecom wavelengths, there is still development that needs to be done in the MIR. The best method to reliably develop new photonic devices is to collect statistics on fabrication reliability and performance using large numbers of fabricated devices. There are many experimental challenges associated with measuring and characterizing large numbers of silicon photonic devices efficiently. The second-half of this thesis will focus on an automated photonics characterization system that was built to expedite the experimental process associated with developing MIR-based photonic devices.

Part II

Room-temperature infrared photonics testing apparatus (RITA)

Chapter 5

Mid-infrared photonics

5.1 Photonics applications in quantum computing

Silicon photonics is an emergent industry that takes advantage of established foundries and etching techniques from the electronics industry to fabricate optical devices on silicon wafers [70]. The most commonly available silicon-on-insulator (SOI) wafers consist of a 220 nm thick float-zone or Czochralski silicon 'device' layer on top of a 2 µm 'buried oxide' layer of silicon dioxide referred to as the 'BOX' layer. Below the BOX layer is the 'handle', a layer of silicon that is approximately 500 µm thick [70]. Often, external optical sources are used to drive these optical circuits. However, having an 'on-chip' source directly in the silicon device layer of the SOI would reduce coupling losses and improve the efficiency of chip-scale optical interconnects [71]. A previous study proposed using the 1s:A $\Leftrightarrow$ 1s:Γ_7 transition of Se^+ implanted in the silicon device layer as an on-chip source [29]. The work presented in Part I of this thesis determined a resonant radiative efficiency of 0.125%, eliminating the possibility of using an implanted donor as a source directly. However, coupling the 1s:A $\Leftrightarrow$ 1s:Γ_7 transition to the electromagnetic field modes supported by a cavity can enhance the rate of spontaneous emission according to the 'Purcell effect' [33]. When the emitter linewidth is narrow compared to the cavity linewidth, the dipole is aligned with the polarization of the cavity, and the fundamental mode of the cavity is resonant with the transition frequency of interest, the spontaneous emission rate of the coupled transition is enhanced by the 'Purcell factor' (F_p):

$$F_p = \frac{\gamma_{cavity}}{\gamma} = \frac{3}{4\pi^2}\left(\frac{\lambda}{n}\right)^3 \frac{Q}{V} \ . \tag{5.1}$$

γ_{rad} is the radiative decay rate of the excited state outside of a cavity structure, γ_{cavity} is the radiative decay rate of the excited state inside the cavity, λ is the wavelength of the transition in vacuum, and n is the index of refraction of the material. Q is the quality factor and V is the modal volume of the cavity. The quality factor characterizes the temporal losses of the cavity and is given by [72],

$$Q = \frac{\omega_c}{\Delta\omega_{\mathrm{FWHM}}} \ . \tag{5.2}$$

ω_c is the resonant frequency of the cavity and $\Delta\omega_{\mathrm{FWHM}}$ is the FWHM of the resonance intensity spectrum. V characterizes the spatial confinement of the electromagnetic mode in the cavity and is given by [72],

$$V = \frac{\int \varepsilon(\mathbf{r})|\mathbf{E}(\mathbf{r})|^2 d\mathbf{r}}{\max\left[\varepsilon(\mathbf{r})|\mathbf{E}(\mathbf{r})|^2\right]} \tag{5.3}$$

where $|\mathbf{E}(\mathbf{r})|$ is the amplitude of the electric field at position $\mathbf{r}$, and $\varepsilon(\mathbf{r})$ is the permittivity at position $\mathbf{r}$.

An ideal cavity-coupled system with cavity modal volumes of $V = \left(\frac{\lambda}{n}\right)^3$ and $Q = 10^4$ could increase the resonant radiative efficiency of the 1s:$\Gamma_7 \Rightarrow$ 1s:A transition by 86.0%, from 0.125% to 10.625 %. For the ideal cavity-coupled system, the donor site must be spatially located at the mode maximum of the cavity, and the cavity and transition must have the same resonance frequency. Previous estimates predict $\sim$ 80 nm straggle in implantation depth and $\sim$ 50 nm straggle in implantation width. This corresponds to less than a 10% deviation in donor-cavity coupling strength [29].

Similarly, we can use cavity-coupled structures to perform readout of the spin state. Strong coupling of a cavity occurs when the cavity-atom coupling constant, g, is much greater than loss-rate of the cavity, $\kappa = \omega_c/Q$ and the atomic decay rate, γ [73],

$$g = \mu\sqrt{\left(\frac{\omega}{\epsilon_0\epsilon_r\hbar V}\right)} \gg \kappa\gamma \ . \tag{5.4}$$

μ is the transition dipole moment, ϵ_0 is the permittivity of free space, ϵ_r is the relative permittivity of silicon, and ω is the angular temporal frequency of the transition. A strongly-coupled cavity-atom system will have transmission (T) dependent on the cooperativity C [74],

$$\begin{aligned} C &= \frac{4g^2}{\kappa\gamma} = \frac{2\mu^2}{\hbar\epsilon_0\epsilon_r\Delta\omega_{\mathrm{hom}}}\frac{Q}{V} \\ T &= \frac{1}{(1+C)^2} \end{aligned} \tag{5.5}$$

where $\Delta\omega_{\mathrm{hom}}$ is the homogeneous linewidth of the transition. The change in transmission characteristics for a strongly coupled system can be exploited for spin-state readout of the Si:Se^+ system. A cavity-atom system where a cavity that is strongly coupled to a singly ionized $^{77}Se^+$ donor and resonant with either the 1s:A:S $\Leftrightarrow$ 1s:Γ_7 or 1s:A:T $\Leftrightarrow$ 1s:Γ_7 transition will exhibit spin-state dependent transmission. Previous work determined the transmission dipole moment of the 1s:A$\Leftrightarrow$ 1s:Γ_7 transtion to be 1.96(8) Debye [30]. Using Equation 2.11 and $T_1 = 7.7(4)$ ns we estimate a homogeneous line width of 0.00058(3) nm

(0.00068(4) cm^{-1}). This value is a lower bound since the homogeneous linewidth will be broadened at higher temperatures due to thermal activation to the 1s:Γ_8 state. For this system, a cavity with modal volumes of $\left(\frac{\lambda}{n}\right)^3$ and $Q = 10^4$ would have a 42% change in transmission when the donor site is in the resonant state compared to the non-resonant state.

Cavity structures in the MIR with resonance at 4.4 µm have already been demonstrated to have Q-factors of 7×10^4 and modal volumes of $\left(\frac{\lambda}{n}\right)^3$, making a promising case for being able to use the cavity-coupled Si:Se^+ system as an on-chip source [72]. However, cavity behaviour relies heavily on understanding losses in the system, which have not been completely characterized near the transition energy of the 1s:A $\Leftrightarrow$ 1s:Γ_7 transition (2900 nm). Specifically, there has been little investigation into the losses associated with O-H bonds in the BOX layer of SOI near at these wavelengths. The O-H bonds have local vibrational modes which absorb light at wavelengths near of 2900 nm which need to be quantified in SOI photonic devices [75]. Moreover, devices operating at 2900 nm on typical SOI (220nm device layer and 2 µm BOX) wafers will suffer high losses due to evanescent coupling into the silicon handle layer. Therefore we will need to characterize the losses of different types of wafers, and potentially different fabrication processes. In order to characterize the losses in photonics devices operating near 2900 nm we developed an automated testing station to efficiently measure fabricated batches of photonics devices. The hardware and automation software are described in Chapters 6 and Chapters 7 respectively.

5.2 Light injection

Waveguides are a standard photonic structure used to control the direction of propagation of light [70]. The most basic waveguide is a strip waveguide that consists of a small 'strip' of silicon with one side adjacent to the BOX layer and the three other sides exposed to air or to an oxide 'cladding' layer [76], as shown in Figure 5.1. Solving Maxwell's equations with appropriate boundary conditions corresponding to the above geometry results in a propagating wave solution within the boundaries of the waveguide and exponential decay outside the boundaries of the waveguide. For small enough waveguides, only the fundamental spatial frequency or 'mode' is allowed to propagate within the structure for a given polarization [70]. We call this configuration a 'single-mode' waveguide. These structures can be used to guide light from a source to a device, like a nano-beam cavity [77], and then guide the transmitted light to a detector. The exponential decay outside the boundaries of the waveguide can also be used to couple to nearby devices, a technique referred to as evanescent coupling [78, 79].

The ideal materials with which to guide and confine light have a large index contrast ratio. The larger this ratio, the smaller the waveguide dimensions can be. Therefore, the

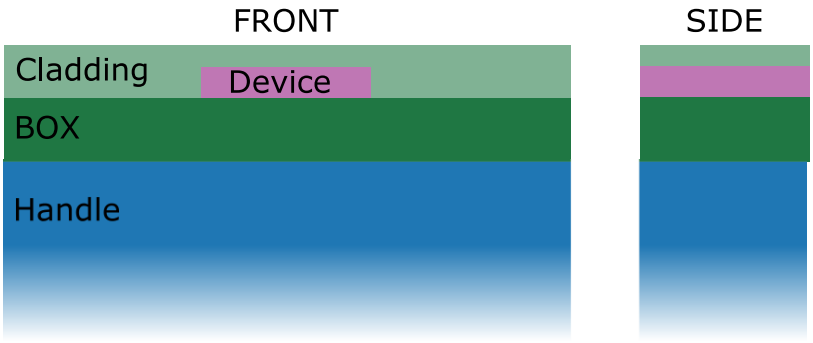

Figure 5.1: Structure of a strip waveguide: a small strip of silicon made out of the device layer of an SOI wafer will guide light confined within the strip. A device layer made with float-zone or Czochralski silicon. The BOX layer is silicon dioxide. The handle is made of crystalline silicon.

large difference in index between silicon (3.43 at 3 µm and 295 K [80]) and silicon dioxide (1.43 at 2.6 µm and 295 K [81]) allow silicon photonic waveguides to have small dimensions (0.5 x 0.22 µm). These small dimensions allow for dense packing of on-chip devices, but make it challenging to couple into the waveguides from large core fibre optic cables ($>$ 9 µm diameter) connected to external sources or detectors [82].

Structures made within the silicon device layer can be used to enhance coupling efficiency between a single-mode waveguide and an optical fibre. Light 'injection' into the chip, from an external source to an on-chip device, can be performed using 'edge coupling' techniques [83]. These structures are often broadband, capable of coupling light over a wavelength range of 500 nm, and have low insertion loss ($<$ 0.5 dB) [70, 83]. A diagram of this technique is displayed in Figure 5.2.

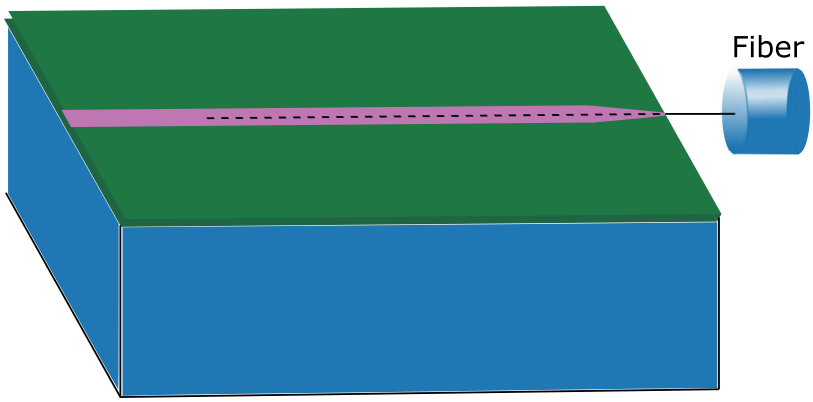

Figure 5.2: Illustration of edge coupling technique: a fibre is brought close to the edge of the chip, a taper guides light into the waveguide.

Unfortunately, edge-coupling techniques are very sensitive to misalignment and often require multiple post-fabrication processes. To reduce alignment sensitivity and increase

on-chip device density, a family of structures have been developed that couple light injected from above the plane of the chip into waveguides. These coupling structures are called 'grating couplers' (GCs). An illustration of a grating coupler is shown in Figure 5.3 [82].

GCs permit a denser packing of photonic devices than edge-couplers since they are not constrained to the edges of the chip and can therefore act as input and output ports anywhere on the surface of the chip. A denser packing of devices is both more economically efficient and time efficient for testing a large number of devices [71]. Grating couplers have a large alignment tolerance which reduces the total time needed to measure each device and reduces variability in device performance due to poor alignment.

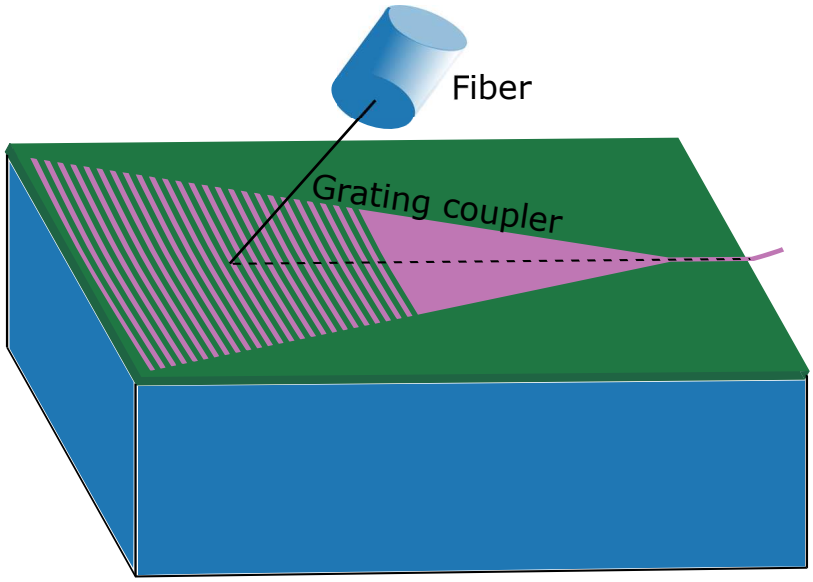

Figure 5.3: Structure of a grating coupler: Sub-wavelength confocal ellipitical strips act with an effective index of refraction. Constructive interference helps to guide incident light into the waveguide for increased efficiency.

The limited bandwidth of the GCs and inefficient geometry of the edge-couplers mean that waveguide coupling may not be the easiest way to measure preliminary cavity structures. Instead, we can use a free-space method that employs a confocal microscopy set-up to measure wavelength dependent reflection off a cavity [84]. A confocal microscope is an imaging apparatus that exploits spatial filtering to increase resolution. By employing small apertures, 'out of focus' light is eliminated, constraining the depth of field to points on the focal plane. This filtering reduces background noise from sources not in the focal plane [85]. Such a set-up located over top of a cavity could measure the reflection of light from a cavity. The intensity of reflected light from a cavity will change when the light is resonant with the cavity compared to non-resonant frequencies of incident light. Frequency-dependent reflectivity can be used to characterize Q-factor values of a cavity. This set-up could prove

useful in the early stages of development when the resonance of our cavities are not within the bandwidth of our coupling structures.

The first step to developing photonics designed for wavelengths near 2900 nm is to simulate these devices. However, there are limitations to the accuracy of simulation. Therefore, we need to develop a system capable of efficiently characterizing a large number of photonic devices with minimal supervision. Such an automated measurement system would ideally be adaptable to the different techniques for light injection and measurement. Moreover, to streamline photonics development for use in the low temperature environments necessary to obtain long spin coherence times, the automated measurement system should also adapt easily to operation within a cryogenic environment. Chapter 6 describes the hardware set-up that will be used to process chips and Chapter 7 describes the software implemented for automation.

Chapter 6

Hardware design and performance

We constructed a room-temperature integrated-photonics testing apparatus (RITA) in order to automate characterization of silicon photonic devices. The design for RITA, illustrated in Figure 6.1, is based on CMC microsystem's *MIP Si-variant* [86]. RITA takes advantage of out-of-plane light injection by using a multi-channel fibre array (FA) to bring evenly spaced optical fibres close to the chip which then couple light in and out of silicon photonic devices through grating couplers (GCs). In this chapter we introduce the design, alignment, and operation of RITA for integrated photonic device testing. Section 6.1 describes the fibre array in detail. Alignment between the GCs and the FA is acheived using motorized linear stages and manual rotational stages. Two telescopic systems provide visual feedback. The stages and telescopic system are described in detail in Section 6.2. RITA can be used to measure transmission at one wavelength at a time, or take a spectrum using, for example, an FTIR system. These two configurations are described in Section 6.3. Operating RITA requires alignment between a FA and a secured photonic chip sample. Section 6.4 describes how samples are secured and outlines a protocol for determining the absolute distance between the FA face and the surface of the photonic chip. Finally, Section 6.5 summarizes the applications of RITA and improvements that could be made on the system.

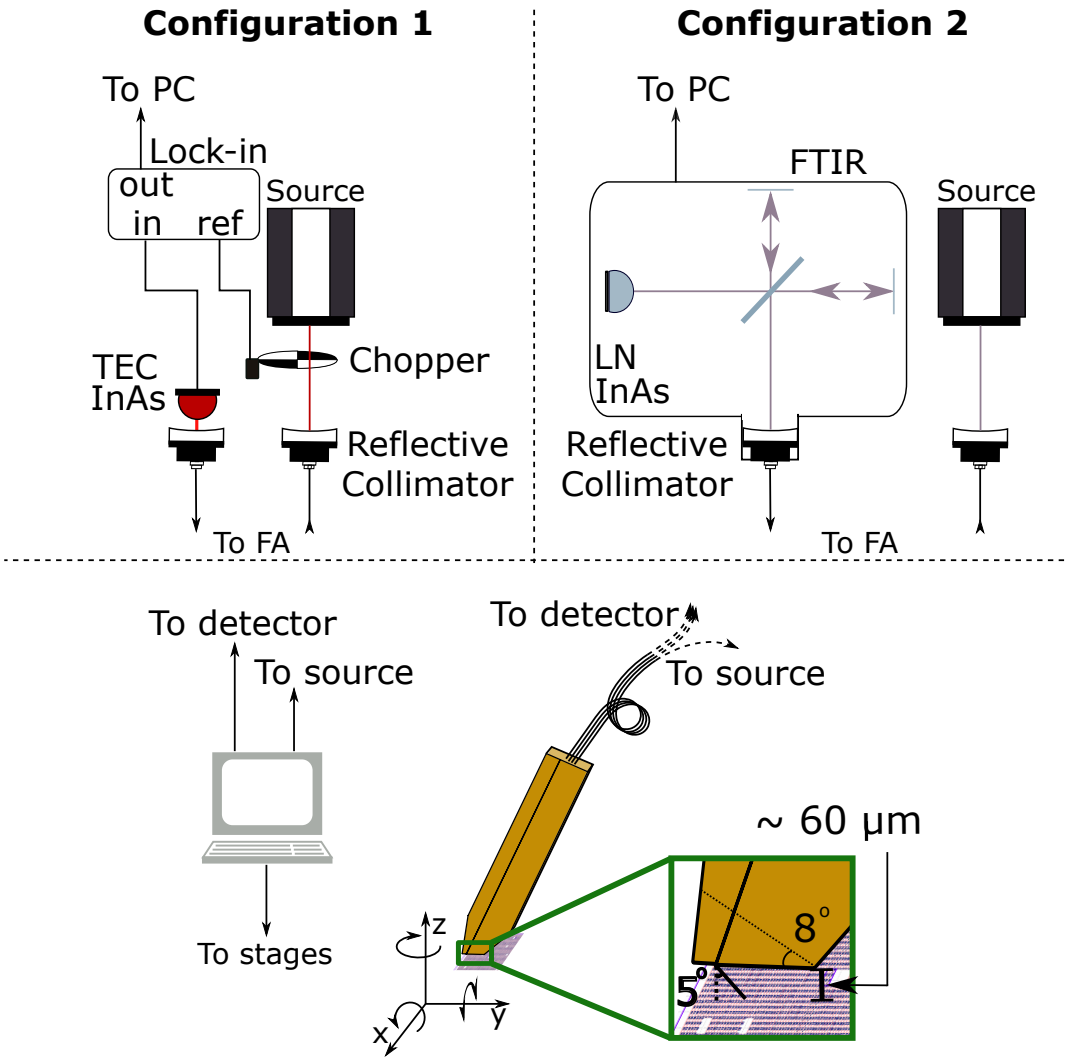

Figure 6.1: RITA uses 3 motorized linear stages with analog feedback in order to move the photonic chip in the horizontal plane (x, y) and the FA in the vertical plane (z). Manual rotation stages (not shown) are used to adjust the insertion angle (360° about the x axis) and in-plane rotation of the chip (360° about the z axis). A goniometer is used to adjust tip-tilt of the fibre array (2°around the y axis). 1 m of Bundled fibres from the FA breakout into four separate 1 m-long fibres. Two different configurations are used to take a measurement. **Configuration 1:** A mechanically chopped single frequency source is coupled through a reflective collimator to one of the fibres in the FA. This fibre is aligned with the input GC of a photonic device. The output GC of the same device is aligned with a different fibre in the FA. The output fibre is coupled to a TEC InAs detector through a reflective collimator. The TEC InAs is used to take a lock-in measurement with the chopper frequency as reference. **Configuration 2:** An MIR broadband Supercountinuum source is coupled through a reflective collimator to one of the fibres in the FA. This fibre is aligned with the input GC of a photonic device. The output GC of the same device is aligned with a different fibre in the FA. The output fibre is fibre coupled to the evacuated detection arm of an FTIR interferometer. An FTIR measurement is taken (see Section 2.6). All instruments are computer-controlled and measurements are automated.

6.1 Fibre array

RITA uses linear 4-channel v-groove FAs consisting of four single-mode fibres spaced 127 ± 1 µm apart. This spacing was chosen to match the spacing of commercially available v-groove clamps [87] and to minimize cross-talk between GCs. A 4-channel array allows simultaneous coupling through four ports. Using one input and three output ports we can characterize multi-port devices like race-track ring resonators or photonic crystal cavities [70, 72]. Currently, the set-up is only capable of using 1 input fibre and 1 output fibre simultaneously. We can scale up the number of ports according to the requirements of future photonic chip designs. Commercially available v-groove clamps permit up to 32 fibres to be mounted. FAs are swapped in and out with a custom FA mount. Therefore, we can use different FAs with optical fibres that transmit over different wavelength ranges. To measure devices operating in the MIR, we use single-mode ZBLAN (Zr_2F_4) fluoride fibres (Le Verre Fluore MIR6.5/125A).

We worked closely with Fibre Tech Optica (FTO) to design the optimal FA that satisfies the stress and strain constraints of the extremely fragile ZBLAN fibres. The fibre block consists of a large rectangular brass (or other machinable metal e.g. stainless steel) ferrule with a tapered end and a protruding quartz v-groove clamp. The GCs have an optical insertion angle that optimizes transmission at specific wavelength regions [88]. The quartz face of the FA and the fibres that are use in this set-up are polished at 8°. Due to changes in index of refraction between the fibre and free-space medium, an 8° polish angle corresponds to an insertion angle in air of 5° at 2900 nm, the predicted optimal insertion angle at this wavelength.

An optical microscope image of a polished FA face is shown in Figure 6.2 a. A manually adjustable rotational degree of freedom, depicted as around the 'x-axis' in Figure 6.1, allows the user to manually adjust insertion angle by rotating the FA face away from the co-planar configuration. The size of the front face of the ferrule limits the range of allowed insertion angles that do not result in collision between the FA and the chip. The tapered end of the ferrule is an attempt to accommodate both ease of fabrication and appropriate strain relief with a wider range of insertion angles and the ability to perform visual alignment using optical microscopes. Upon exiting the ferrule, all four fibres remain bundled before breaking out into four separate connectorized fibres. This design makes handling long fibres easier, reduces strain, and prevents accidental pinching at the ferrule exit point.

We measured the frequency response of each fibre in order to properly normalize transmission through devices. Figure 6.3 displays the jointly normalized frequency response of each fibre in the FA displayed in Figure 6.2, showing excellent consistency between the fibres. Transmission data was taken using the FTIR spectrometer as described in Section 2.6 with a liquid-nitrogen-cooled indium arsenide dector (LN InAs). For this measurement, the detector chamber was not evacuated and the structure in transmission between 1000 and

3700 nm is due to absorption by water vapor in the air. Our set-up is able to minimize the water-vapour in the beam path though evacuation and purging techniques during photonics measurement as discussed in Section 6.3.

The fibres are terminated with standard FC/APC connectors that readily couple to commercially available reflective collimators (Thorlabs RC04FC-P01). Light coupled into the fibre is guided to the end of the fibre face where it exits. Devices to be measured must be designed with grating couplers spaced to match the 127 µm spacing of the fibre cores in the FA.

6.2 Stages

The system gives users 6 mechanical degrees of freedom (DoF) which can be tuned to optimize transmission through devices: 3 motorized linear stages (along x, y, and z in Figure 6.1), 2 manual rotation stages (around x and z in Figure 6.1), and 1 manual goniometer (tip-tilt around y in Figure 6.1). The relevent specification of the DoF are litsted in Table 6.1. The core-to-core fibre spacing accuracy of 1 µm falls within the current FWHM alignment tolerance (approximately 5.5 µm) of our GCs discussed in detail in Section 6.4.

We use lead-screw actuated, motorized stages with an optical feedback strip. The resolution of our stages step size is smaller than the accuracy of fibre array core-to-core spacing and therefore not limiting to the performance of RITA. Rotational alignment is only performed one time per photonic chip, so these degrees of freedom are not motorized. Instead they are manually adjustable which means their accuracy is limited by the person using them. This design choice was taken before much of the photonic simulation work had been performed and is naive in its assumption that the devices will not be very sensitive to rotational misalignment. A future iteration of RITA should implement motorized rotational degrees of freedom for maximal alignment control and repeatibility.

Two telescopic systems coupled to cameras are placed at 90° from each other, along the x and y axes in Figure 6.1. One is aligned parallel to the chip (along y in Figure 6.1) for accurate visualization of the gap between the fibre array face and the surface of the chip. The other is aligned at an angle that can image both the on-chip devices and the edge of the FA. Sources and detectors can be swapped in and out easily, and currently two different configurations have been used to measure devices and assess overall system performance. These two configurations are described in more detail in Section 6.3. The full list of equipment is displayed in Appendix A.

6.3 Sources and detectors

The technology of sources and detectors operating around 2900 nm is underdeveloped compared to the telecom band. The ideal RITA source would be a robust CW, single-mode,

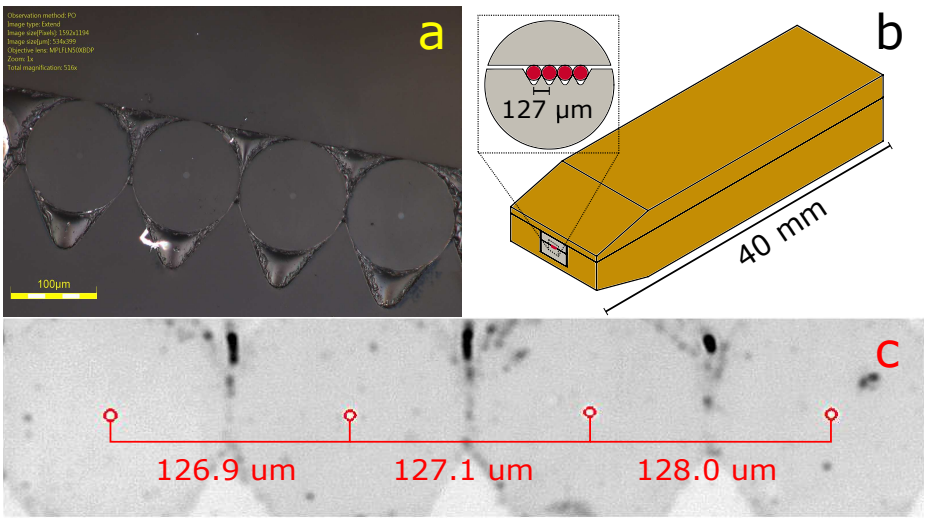

Figure 6.2: **a** Optical microscope image of FA face. **b** Mechanical drawing of brass ferrule enclosure surrounding quartz fibre array (grey) with fibre faces highlighted in red. **Inset:** Close-up of v-groove with fibres spaced with measured core-to-core distances.

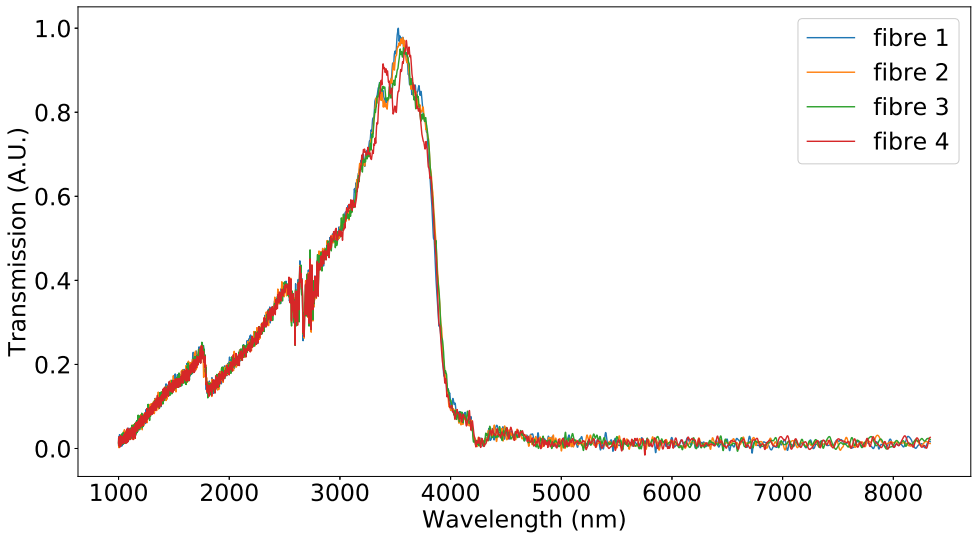

Figure 6.3: Fibre transmission in a fibre block. All fibres are normalized to the largest transmitted value of fibre 1.

broadly tuneable, single-frequency source with linewidths narrower than high-Q cavity bandwidths. Since such a source does not yet exist at 2900 nm, we employ two configurations that each represent alternative compromises on the desired feature-set.

6.3.1 Configuration 1: Single frequency, multi-mode laser source and TEC InAS detector

In this configuration, a mechanically chopped, 3-7% pick-off (< 100 mW from a 1 W main beam) of a tuneable multi-mode laser (IPG Photonics CLT-2400/1100-1) is free-space coupled to one of the FA fibres using a reflective collimator. The IPG laser is tuneable between 1850 and 3050 nm. One of three possible output fibres is coupled to a reflective collimator aligned with a thermo-electrically cooled (TEC) Indium Arsenide (InAs) detector (J12TE4-3CN-R250U). This detector is sensitive over the range 2000-3300 nm. It is used to perform lock-in measurements with the mechanical chopper frequency as its reference.

In order to normalize transmission measurements to the output power of the laser, the main beam is directed into a Thorlabs thermal power sensor (Thorlabs S415C). Furthermore, on-chip 'calibration' devices are used to normalize against slowly varying and static ambient conditions like humidity and inhomogeneities across the chip. These devices consist of a pair of grating couplers, spaced to match FA spacing, connected by 160 µm of waveguide.

This configuration can run continuously and requires little assembly beyond coupling into and out of the FA fibres through a reflective collimator. Moreover, this configuration can be scaled up to measure transmission through multiple ports by coupling the third and fourth fibres to additional TEC InAs detectors.

Unfortunately, the linewidth, water absorption in the air, power fluctuations, and multimode operation of the IPG makes this configuration unsuitable for performing high resolution, low-noise wavelength sweeps. Until a more appropriate single-frequency source is available we use the configuration discussed in Section 6.3.2 to characterize the frequency dependence of our photonic devices. Configuration 2 uses a Supercontinuum source and FTIR spectrometer to measure the frequency response of devices with extremely fine resolution.

6.3.2 Configuration 2: Supercontinuum source and FTIR spectroscopy

A Supercontinuum source (Thorlabs SC4500) produces a broadband (1.3 — 4.5 µm), single-mode, collimated beam. The Supercontinuum source is coupled into one fibre of the FA through a wide aperture reflective collimator. One of the three output fibres is coupled into

Part	Relevant Spec.	Value
Fibre block	Core-core spacing accuracy	± 1 µm
3 Motorized linear motion stages	Resolution	0.05 µm
	Bi-Repeatability	±0.2 µm
	Accuracy	± 6 µm
2x Manual Rotation stage	Fine-adjust range	± 5°
Manual Goniometer (tip/tilt)	Travel Range	2°

Table 6.1: RITA linear and rotational motion specifications

the FTIR spectrometer introduced in Section 2.6 to measure the transmission spectrum of photonic devices. The TEC InAs has a lower detectivity (ratio of detection area to noise-effective-power) compared to a liquid nitrogen-cooled InAs detector (LN InAs), making it less useful for taking high resolution spectroscopy with the FTIR.

Water-vapour absorption is a large source of signal loss and distortion in our system. The Bruker FTIR can be evacuated to eliminate the water-vapour that is present in air. Furthermore, we can 'purge' the region where we free-space couple from the Supercontinuum to the input fibre by replacing the air with nitrogen. The Supercontinuum source includes a back panel gas inlet that exits through the front panel where the collimated beam exits. This feature allows us to fully enclose the path from laser to detector in a water-vapor-free environment. A purge box encloses the front panel of the source. When nitrogen is fed into the gas inlet at the back panel of the Supercontinuum source, the air within the purge box is replaced by nitrogen.

We can see the improvement in signal by comparing calibration device spectra using an un-purged and purged version of configuration 2. The spectrum from purged configuration 2 shows intereference fringes with 4 nm periodicity due to interference from reflections within the photonic device measured, Figure 6.4(b), this fringing is unresolved in the spectrum taken with the un-purged version of configuration 2 as displayed in Figure 6.4(a).

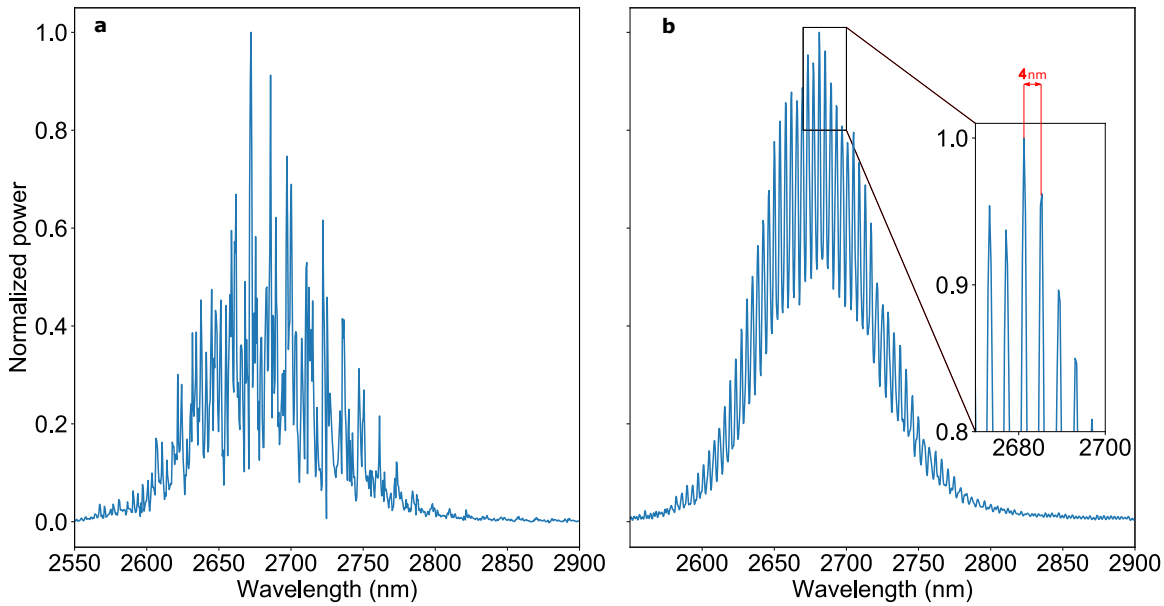

Figure 6.4: **a** Spectrum of a calibration device taken using configuration 2 before purging the source beam path with nitrogen. Here we see water vapour absorption from air in the beam path. **b** Spectrum of the same calibration device taken using a purged configuration 2 displaying interference fringes with 4 nm periodicity. Here we see no distortion from water vapor absorption since the majority of free-space beam path is either in nitrogen or vaccuum.

Unfortunately, there is a trade-off between the resolution gain of an FTIR measurement and the efficiency and scalability possible with a tuneable laser. High resolution, low noise spectra require high averaging rates and therefore long measurement times per device. Furthermore, the LN InAs detector is required to be immersed in liquid nitrogen. The detector can only operate continuously in this state for a few hours before the liquid nitrogen boils off and the detector warms. Lastly, this set-up can only be used with one output port per FTIR apparatus. The long arm of the Bruker FTIR spans over 3.5 m. Therefore, having more than one high-resolution FTIR system is quite rare, and unlikely in this lab.

6.4 Operation and initial alignment

A software suite (SUPER), described in detail in Chapter 7, can be used to automate multiple experiments on a single chip. However, before RITA can operate without supervision, manual alignment must be performed to obtain maximum transmission through a single device. For manual alignment, we use configuration 1.

6.4.1 Sample placement

Experiments with either configuration on a single photonic chip can last multiple days depending on the device density of the chip. In practice, chips remain mounted for a few weeks while multiple characterization experiments are performed. Therefore it is important to secure the photonic chips to maintain alignment while avoiding strain that could negatively effect performance of the devices. The chips are mounted on an aluminum block using a spin-coated layer of PMMA to secure the chip on a flat surface with minimum strain. With the current mounting method, there is no guarantee that any chip will have the same dimensions or be mounted in the same orientation. This method could be improved in a future iteration by having an indented platform with dowel pins to minimize rotational variance when swapping samples in and out. Once the sample is mounted, rough manual adjustment of the rotation stages is performed with visual feedback from the telescopic systems. Next the sample must be brought into alignment with a device using the motorized linear stages.

The light coupling into the chip diverges from the end of the fibre array, so transmission will decrease rapidly with increasing 'working distance', distance from the surface of the chip to face of the array. To avoid damaging the fragile end of the fibre array or the chip, it is important to determine the working distance while avoiding collision between the fibre and the chip. Ideally the process for z-height alignment will adapt to applications in cold environments without visual feedthroughs.

6.4.2 Working distance

NIR versions of the system [86] use physical contact between FA and the chip to determine the absolute height of the fibre array above the surface of the chip with respect to the

system's motor coordinates. However, the ZBLAN fibres are too brittle to perform a contact alignment process, so we use two USB-coupled, telescope mounted, CMOS cameras to infer an approximate height for initial alignment. Here we propose and demonstrate a protocol using vertical sweeps (in the 'z' direction as depicted in Figure 6.1) to determine the working distance. A protocol that can find the working distance across multiple devices on the chip can be used to determine height variations over the surface of the chip, and ensure no costly collisions. We will discuss the two protocols to estimate z-height working distance. During this discussion z-height values will refer to positions as read by our stage, called motor coordinates. We will present the predicted motor coordinate that would result in contact between the fibre array and the grating coupler, called 'z_0'.

The protocol is based on the fact that for a two-port device, in the far-field regime ($\gg \lambda$ working distance), we can model both input fibre and output grating coupler as a point source following an inverse-square drop in intensity (I) as we move away from the chip,

$$I = \frac{\text{const}}{(z - z_0)^2} \ , \tag{6.1}$$

where $z - z_0$ is the working distance from the chip at position z. An example of raw data and the inverse-square fit for an arbitrary calibration device, 'device 1', is displayed in Figure 6.5. Assuming a naive model of an isotropically emitting source of constant power (P) exiting the chip, this means the intensity at a point on the grating coupler with distance z away from the tip of the fibre is given by,

$$I = \frac{P}{4\pi(z - z_0)^2} \ . \tag{6.2}$$

The second protocol tracks the FWHM of the elliptical gaussian transmission footprint in the chip plane ('x-y' plane depicted in Figure 6.1) as it changes with working distance. Intensity over a surface of constant power is the power divided by the area (A) incident on the chip,

$$I = \frac{P}{A} \ . \tag{6.3}$$

We approximate the area of the constant power surface incident on the chip as a circle with radius FWHM/2 ,

$$A = \pi \left(\frac{\text{FWHM}}{2} \right)^2 . \tag{6.4}$$

Using the definition of I from equation 6.2 we can write FWHM in terms of z,

$$\text{FWHM}(z) = \text{const} \times 4\,(z - z_0) \tag{6.5}$$

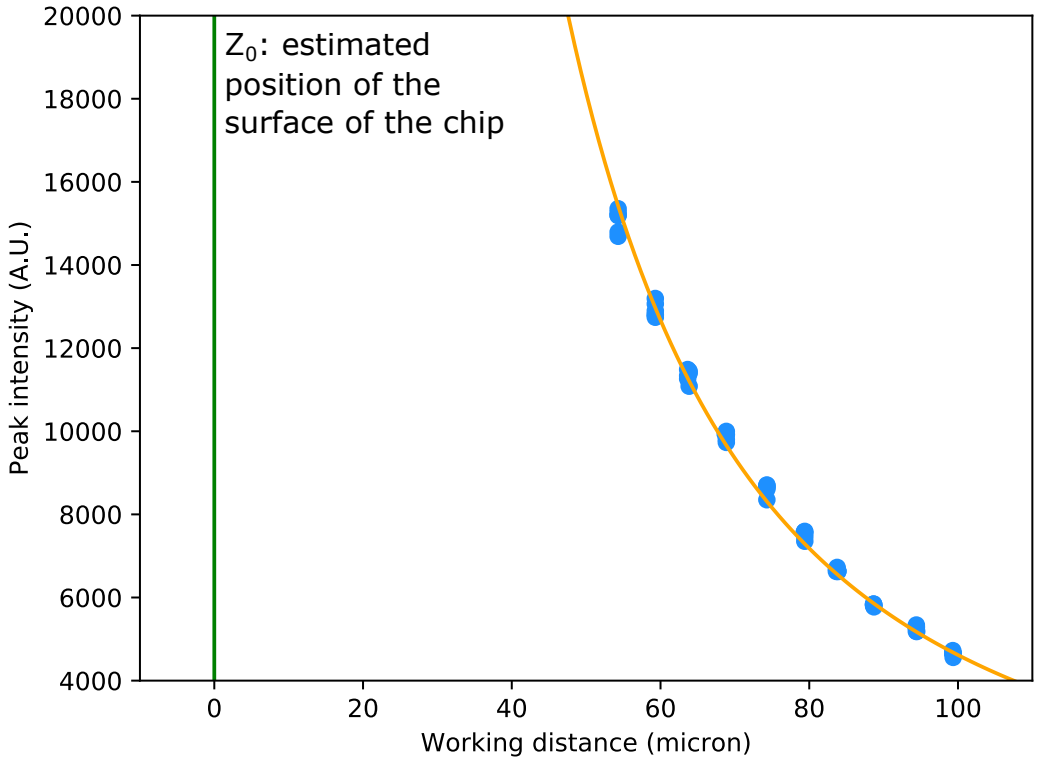

Figure 6.5: Transmission through a calibration device as a function of the FAs distance away from the chip. FA height is shown here as the estimated working distance: the estimated distance away from the chip given the calculated Z_0. Orange line indicates the fit to Equation 6.2. Green line denotes the predicted z_0 from the fit at a working distance of 0. The z distance of each point to the predicted z_0 represents the working distance at that height. The smallest working distance that we have been safely working at for this device is $\sim$ 53 µm.

To verify this linear dependence in working distance we perform a 30 x 30 µm scan over the device in 0.5 µm steps over 10 different z positions. An example of raw data and the linear fit for device 1 is shown in Figure 6.6.

Equation 6.5 would indicate that FWHM($z = z_0$) = 0, which would predict a $z_0 \sim 60$ µm lower than the z_0 prediction of protocol 1. However, in this case it is instructive to go beyond the far-field limit and consider the finite width of our device. Device 1 is a calibration device. A calibration device consists of two grating couplers connected by a waveguide, as illustrated in Figure 6.7. Each GC has a characteristic width of 11 µm. Moving the motors by 1 µm away from the maximum transmission point will misalign both input and output ports in our setup. This will result in a transmission loss twice as high as would be expected by misaligning a single port since both input and output ports will be misaligned by 1 µm.

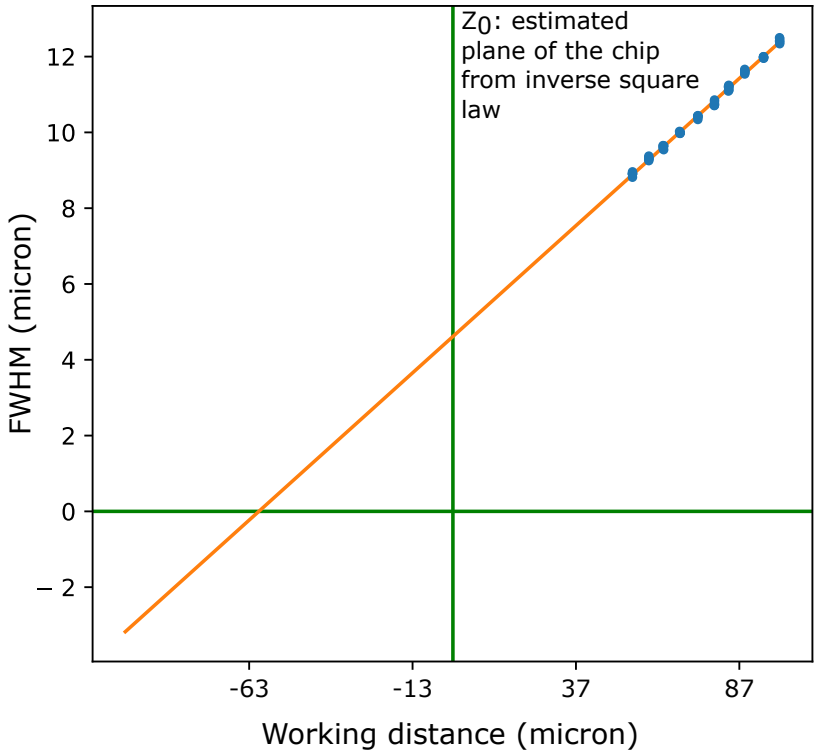

Figure 6.6: FWHM in the y direction of transmission through a calibration device as a function of the estimated FAs z-height away from the chip. Yellow line indicates a fit to Equation 6.5. Green line denotes the predicted z_0 from the previous protocol of 22.762 mm. Fitting to 6.5 would indicate the z_0 to be at the FWHM= 0 point, however taking into account the finite width of the GCs we see agreement between the z_0 extracted from 6.2, shown by the solid black line.

Therefore, we expect the FWHM($z = z_0$) along the x axis to be approximately $^{11}/_2 = 5.5$ µm, and along the y axis to be approximately $^{32}/_2 = 16$ µm. However, instead, we measured, a FWHM$_x$($z = z_0$) of 3.9 µm, and a FWHM$_y$($z = z_0$) of 4.7 µm.

Our preliminary data are well fit by Equations 6.2 and 6.5, indicating that our far-field model of a point-source is sufficiently correct to safely estimate z in the far-field limit to avoid collisions.

Working in the far-field limit, we can use this procedure to determine systematic spatial variation or 'run-out' along the chip. If we perform z-sweeps over calibration structures located at different positions on the chip, we can compare z_0 values extracted from fitting to Equation 6.2 to get the relative height of the chip at different positions. We were able to extract the z_0 parameter for 7 calibration devices on a chip as displayed in Figure 6.8. Here we can see that the devices appear to fall on an otherwise planar slope with the exception of device 101. For reliable z_0 data, this procedure can be used to reduce error in our device characterization due to on-chip height variations.

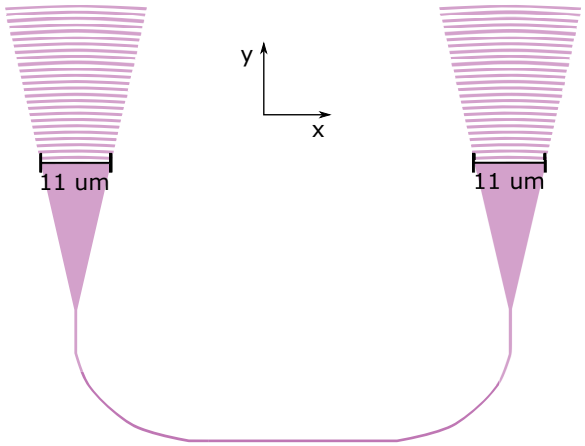

Figure 6.7: Illustration of calibration device. The 'characteristic width' of each grating coupler is approximately 11 µm.

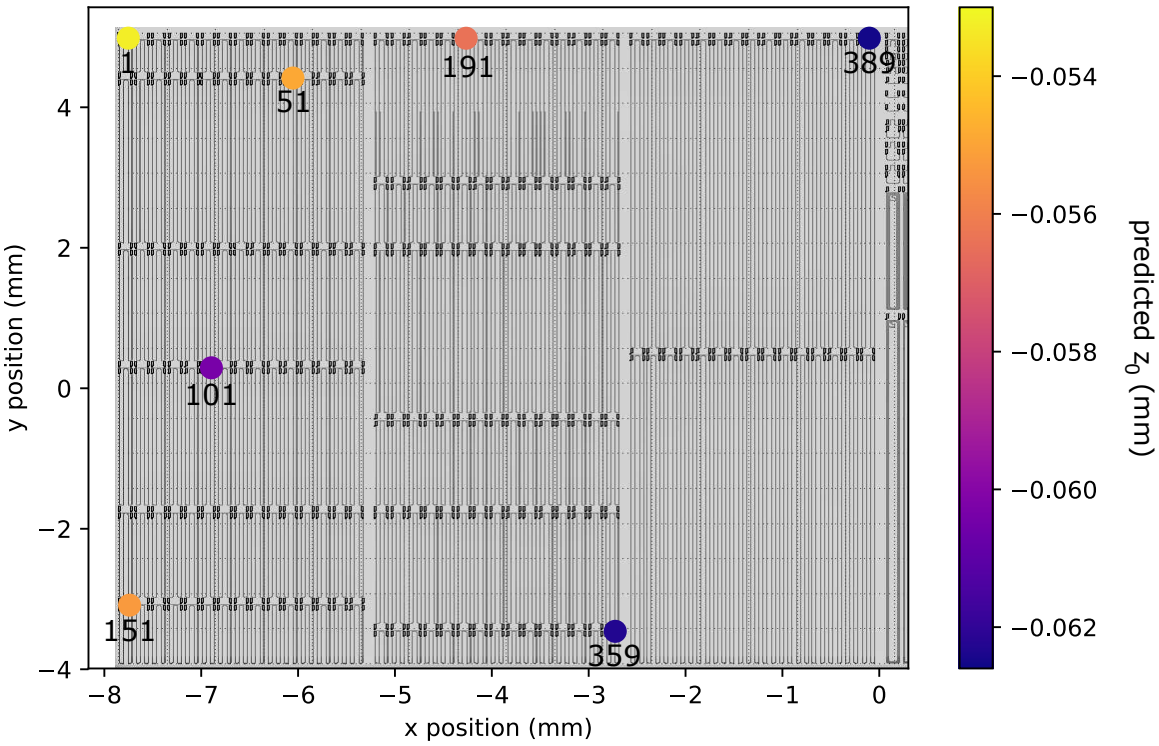

Figure 6.8: Extracted z_0 values (colour scale) from multiple devices (numbered) across the chip as a function of position on the chip. Black and white background is the design-file aligned with the measured devices. Here we see Device 101 as an outlier on an otherwise planar slope.

6.5 Future work

RITA is currently designed to work at room temperature and standard atmospheric conditions. However, the overall design can be replicated in a variety of environments given appropriate stages. As described in more detail in Chapter 7, the software that controls the system is general, allowing for different equipment (cryogenic motors, different sources) to be introduced to the system with minor development.

A future iteration of RITA would incorporate motorized rotational, and tip-tilt stages in order to streamline the alignment process. Furthermore, depending on measurement conditions and the adaptation of RITA to other environments, stability and measurement repeatability might be improved by using polarization maintaining (PM) fibres. Since the on-chip grating couplers are inherently polarization selective, when we do not use PM fibre this makes our system sensitive to vibrations. When the technology is available, an FA using PM MIR fibres should be designed and sourced. The system is modular by design, and any fibre array is easily swapped with another of similar size and shape.

RITA currently uses two configurations to obtain a complete characterization of photonic devices. Configuration 1, using a tuneable laser source and a TEC InAs detector can measure transmission efficiently and without supervision. Configuration 2, using a Supercontinuum source and an FTIR system, can take high-resolution spectra. However, configuration 2 does not scale well, is extremely time-intensive, and requires supervision in order to keep the detector cold. Once initial cavity characterization has been performed, we can incorporate narrow-band sources that are able to scan over high-Q cavity resonance frequencies reliably.

In either configuration, measurements on RITA are sensitive to changes in ambient conditions. We see these effects most drastically in the power output over the bandwidth of the grating couplers. Source output power depends on ambient temperature conditions which cause transmission through the grating couplers to change up to 80% overnight when temperature fluctuations are largest ($> 1^{\circ}$). We also see the effect of temperature changes as a shift in the optimal x-y motor coordinates of on-chip devices. We use SUPER, as presented in Chapter 7, to mitigate these sources of noise by automating periodic measurement of calibration structures over the duration of any experiment. The same software suite implements searching algorithms that adapt to signal changes from spatial shifting due to thermal contractions or expansions of either the motorized stages or the chip itself.

Chapter 7

Automation

Our silicon photonic chips have thousands of devices on them. Manual alignment takes at best tens of seconds and at worst hours. It is therefore advantageous to automate the alignment measurement process so that once a photonic chip is fabricated, we mount it on RITA and let the system characterize it without supervision. In order for such an automated system to be future-proof, the control software must be sufficiently general to encompass all the functionality we want currently, and allow for it to extend easily when other researchers have different characterization tests they want to perform. Furthermore, the software would ideally extend to control other physical configurations beyond RITA. The control software, must be sufficiently clear and robust such that new users are capable of performing customized experiments safely. We designed the Software Upholding Perfect Experimental Reliability (SUPER) to meet these needs.

In this chapter we describe the architecture of SUPER, organized as follows: Section 7.1 presents the high level design of SUPER. Section 7.2 presents a detailed description of the organization of SUPER. Section 7.3 concludes this chapter with an example of how SUPER may be used to measure the transmission and frequency response of all calibration devices printed on an integrated photonics chip.

7.1 High-Level Design

7.1.1 Data Management

We use a relational database data management scheme. Experiments on photonic devices have multiple sources of data: the photonic chip design file, physical parameters of the measurement apparatus, and the results. Information about a photonic chip design is stored within a binary format GDSII file ('GDS' file). This file is then sent to an external foundry for fabrication. We use the GDS file as a blueprint for the photonic chip. SUPER reads GDS files and records information on the design parameters and positions of each photonic device on a chip. This information is saved to a table in a database hosted on a local server.

SUPER uses this chip information in order to coordinate alignment of the fibre array with the on-chip grating couplers.

There are three fully operational apparatuses that are currently controlled using SUPER. The type of instruments SUPER can control are described in more detail in Section 7.2.1. The data that is produced by the measurement apparatus are the scan parameters and results, such as laser frequency and transmission through a photonic device. The metadata of the measurement apparatus includes information such as which instruments were used and the date and time an experiment was started. Data and metadata are stored in separate tables in the same database as the GDS information. A full description of the database structure and how it is accessed by SUPER during experiments and analysis is given in Section 7.2.2.

7.1.2 Safety

We need to ensure SUPER continues to perform as desired while multiple researchers contribute to its code-base. We achieve stability by requiring all new development on the software pass a suite of hardware and software tests. Using virtual equipment and test data, we can safely test how our scripts and algorithms behave. We use a remote repository to store the working copy of SUPER with enforced contribution rules concerning naming-schemes and documentation. We currently implement over 1600 software tests that any new development must pass before being allowed to be tested or implemented on the computer connected to hardware.

7.1.3 User interface

There are three different types of researchers that will run 'sessions' of SUPER, where sessions refer to the period of time SUPER is controlling an automated measurement station. A 'user' is a researcher who passively uses SUPER. A user can start sessions of SUPER through the graphical user-interface (GUI). The GUI only gives the user access to a subset of the full functionality of SUPER. A user can also perform experiments on any of the measurement apparatuses by editing configuration files, written in YAML [89], and using pre-defined measurement sequences we call 'runs', described in more detail in Section 7.2.3. A 'user-developer' is a researcher that wants to develop new runs. SUPER is designed such that a user-developer can use all the functionality of SUPER to design new runs without danger of causing damage to the physical instruments or sample that is being measured. A 'developer' is a researcher who may be building a new instrument or measurement apparatus that they want to control with SUPER or wants to add functionality to SUPER.

7.1.4 Applications

The goal was to create a software platform to run RITA and any future systems with similar operating principles. Currently, SUPER is used to control RITA, a cryogenically compatible version of RITA, and a cryogenically compatible confocal microscope set-up. For the software to be general enough to be used interchangeably with any of these systems, we organized the code according to the principles of abstraction and encapsulation. The physical system is encapsulated within software objects and the complexity of these software objects are abstracted to allow user-developers an intuitive base upon which to build the software behind their experiments.

7.2 Implementation

The main source-code of SUPER is written in Python (v. 3.6) and organized into a class structure. Python does not have any strict typing or function overloading, therefore we take a heuristic approach to abstraction of the system using a folder system. The structural schematic of SUPER is displayed in Figure 7.1. There are 3 layers of abstraction. Each layer of abstraction contains folders, or 'packages' that contain scripts, classes, and modules that all have a common theme. Packages in Figure 7.1 are shown in bold-italics. A 'script' is a file containing a set of instructions that is executed each time the file is run. A 'class' defines the instructions to construct an object and how that object interacts with other objects. A class has properties called 'attributes' and functions called 'methods' that are shared by any 'instance' of the class, a constructed version of the class. A module contains a set of functions that can be imported and used within other libraries, classes or scripts.

The first and second layer of abstraction, level 1 and 2 in Figure 7.1, are meant to be edited and expanded by a developer. Level 1 and 2 are described in Sections 7.2.1 - 7.2.2. The third layer of abstraction, level 3 in Figure 7.1, is meant to be edited and expanded by a user-developer or used directly by a user. Level 3 is described in Section 7.2.3.

7.2.1 Level 1: instruments package

The least abstracted modules, the bottom row of modules in Figure 7.1, interact directly with the equipment. These modules are contained within the *instruments* package. Any system that uses SUPER must have equipment that can be loosely classified as a stage, detector, or source. A stage refers to any equipment with computer controlled motion. This currently includes stages with linear, rotational, or goniometric motion, but may be expanded to include, for example, a heater for temperature dependent experiments. RITA has three lead-screw actuated linear translation stages which are organized into one multi-axis stage object with 3-dimensional control (*class micronix*). A detector refers to any equipment with measured values that cannot be manipulated by the user. RITA uses two different types of detectors, a lock-in amplifier (*class lockin5210*) and an FTIR spectrometer

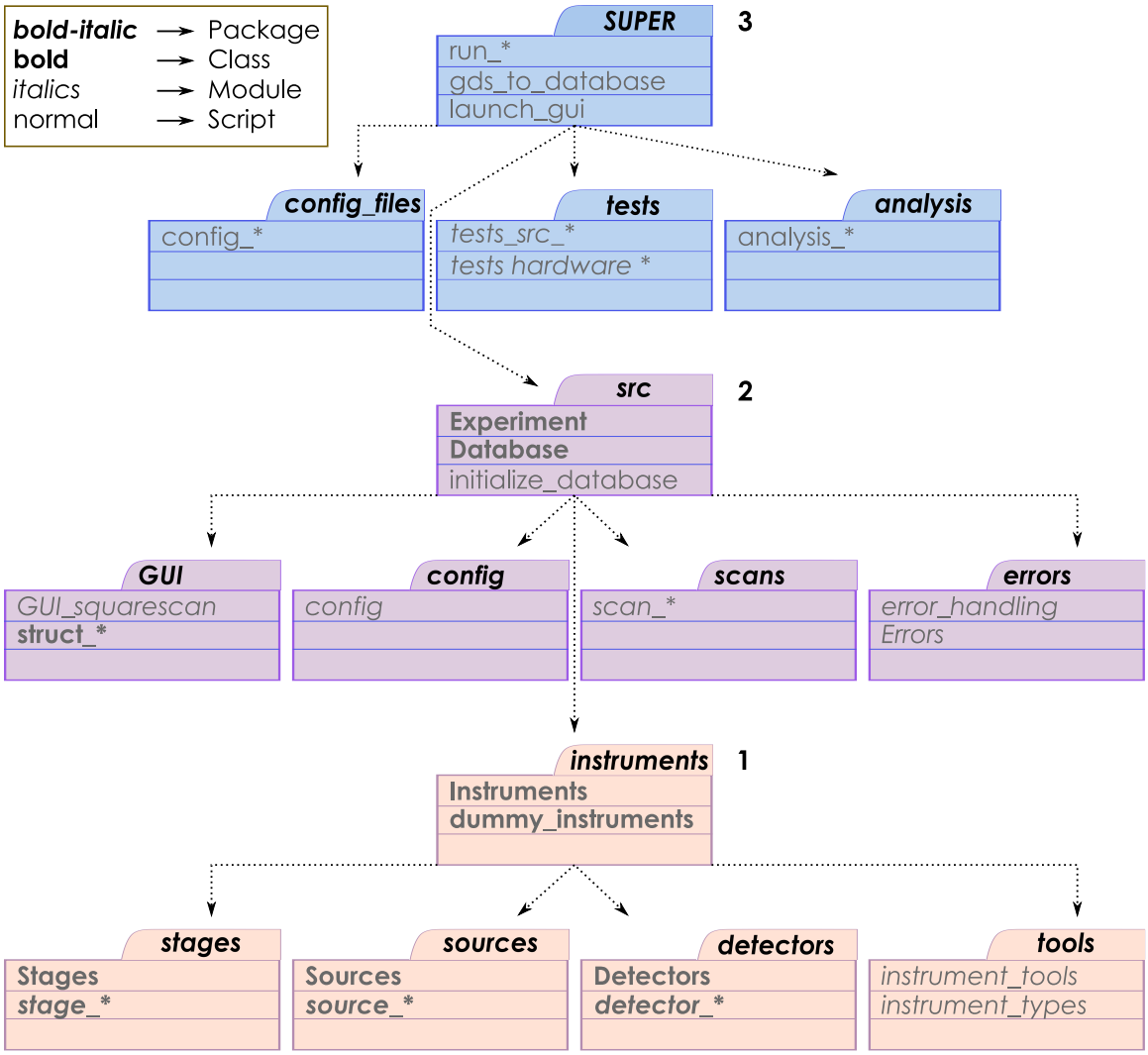

Figure 7.1: Structure of SUPER in layers of abstraction 1,2,3 (see text). Packages (bold-italic), classes (bold), modules (italic), and scripts (normal) are displayed. Arrows denote which packages are directly contained within the higher level packages. Multiple objects that perform similar tasks are lumped together under a common name with _* appended.

(*class opusclicker*) that takes measurements using the FTIR spectrometer. A source refers to pieces of equipment that are not stages with attributes set by a user. Regardless of physical source, the software recognizes only the piece of equipment that it controls as the source. For example, the source used in RITA can be a Supercontinuum source, however SUPER treats the mechanical chopper as the source since turning it on or off is what defines which type of measurement can be recorded: when the chopper is on we can take a lock-in measurement, when the chopper is off we can take an FTIR measurement. Each individual piece of equipment is associated with a class that encapsulates the state of the equipment

itself within its attributes. The specific equipment class also defines the methods to send read and write commands to the physical instrument.

a) Stages example

One example of the encapsulation of a physical instrument is the *Micronix* module, that contains a three-axis stage class, *XYZStage*. *XYZStage* defines a type of stage that has 3-dimensional linear movement. For example, an instance of the *MicronixXYZStage* controls the lead-screw actuated motors of RITA whereas an instance of the *AttocubeXYZStage* controls the piezo-actuated motors used in a cryogenically compatible RITA. Figure 7.1 labels these instrument specific modules as *stage_, source_, detector_*.

The state of the three physical motors encompasses: the position of all three motors as calculated by the position of the lead screw, the position of all three motors as inferred from an optical feedback strip, a flag for whether or not the motors have reached the end of travel, and status messages on whether the motors are operating properly. We store the complete status of each motor as attributes within the class.

Measurements are taken by polling the attributes of an instrument specific class, therefore the update rate of the attributes within an instrument-specific instance, like the *MicronixXYZStage*, can effect the accuracy of a measurement. For example, fluctuations in measured value when the micronix motor has not been sent a move command are artefacts of the firmware and should not be taken into account. As such, the *MicronixXYZStage* class only refreshes the attribute that stores the position of the motor when a move command is sent.

We use 'umbrella' classes to control the instrument-specific classes. This allows us to implement safety checks that apply to all instruments of the same type. For example, an instance of the *MicronixXYZStage* is controlled by a *Stages* instance. When a move command is sent, the *Stages* instance checks whether the new position is within the user-defined soft limits, and at the end of the move, the *Stages* instance checks whether an error has been identified by the motors. Another example of implementing safety checks in *Stages* is when more than one three-axis stage type is used with RITA or a RITA-like set-up. When a rotational three axis stage, with rotation and tip-tilt degrees of freedom, is being used at the same time as a linear three-axis stage, certain coordinates will result in collision between the fibre array and the chip. Before a move command is sent to the physical motors, an instance of *Stages* can be used to compare the coordinates of the rotational three axis stage with the coordinates of the linear three axis stage to block any movements that may result in collision.

Each physical system is encapsulated by SUPER with a similar structure to stages. This means that each physical source has its own class that falls under the umbrella class of *Sources* and likewise for detectors. The class that controls these umbrella classes is the *Instruments* class. An *Instruments* instance is responsible for initializing and coordinating all

instruments associated with a particular session of SUPER as defined by the configuration file (Section 7.2.3).

7.2.2 Level 2: src module

The instruments package is part of the *src* package. Modules, scripts, classes, and libraries contained within *src* are intended for editing only by a developer familiar with both Python and SUPER.

a) errors package

The *errors* package contains the *Errors* module that contains all the SUPER-specific errors like *StagePositionError* and *SourceError*. The *error_handling* module is a library of commonly used functions to handle errors. The *errors* module allows our error handling and testing to be specific. As such, when things go wrong, a researcher will be able to understand where the error occurred and what it means.

b) scans package

The *scans* package is located in *src*. It is a library of *scan* modules that contain scanning functions agnostic to the specific instruments used. Every scan has a similar structure, illustrated in Figure 7.2. Each scan performs a sequence of movements and measurements that can be carried out on any instrument of the same type. For example, a scan intended to act on a *MicronixXYZStage* in a scan must work on any *XYZStage* defined within the stages module.

Every scan must be designed to have either one or two independent variables (S_1 and S_2) that are being swept and at least one dependent variable (V) that is measured. In order to maintain consistency between scans, every scan must have a function *do_scan_name* for a scan object with name 'scan_name' with function inputs S_1*_start*, S_1*_stop*, and S_1 *_step* .

The S_1 and S_2 start, stop, and step are defined upon initialization of a scan object. Initializing a scan object may be done in a run as described in Section 7.2.3. The physical parameters corresponding to S_1, S_2 and V are defined by the configuration file (Section 7.2.3).

c) config package

The *config* package contains only the *config* module. The config module is a library of necessary functions to load a configuration file and extract all the information into a form useable for the *Experiment* (Section 7.2.2) and *Instruments* (Section 7.2.1) classes.

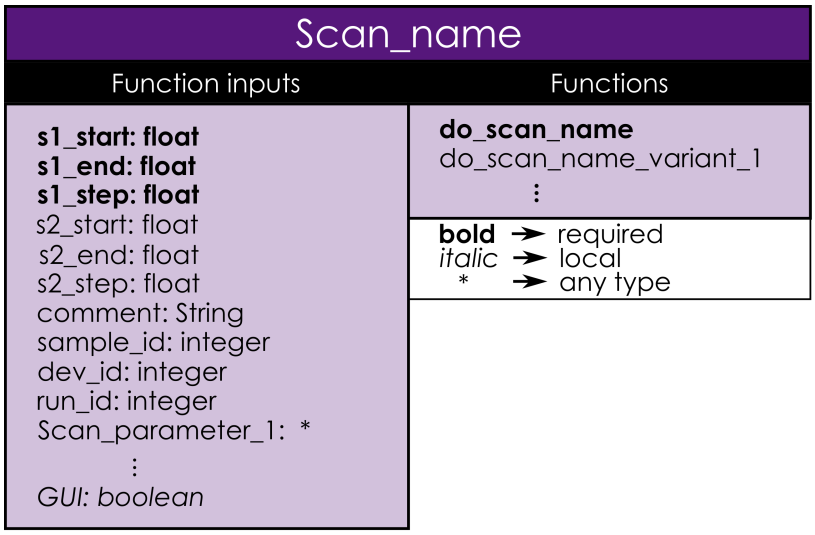

Figure 7.2: The skeleton of a scan module. Every scan is a module with name, *Scan_name*, and has a function *do_scan_name* and function inputs S_1*_start*, S_1*_stop*, and S_1 *_step*, enforced through testing, shown in bold. Each individual scan may have additional functions or function inputs, shown in italics.

d) GUI package

The GUI package contains all classes and functions necessary to run the GUI. The GUI uses PyQt5 backend and currently has a *GUI_Squarescan* library of functions necessary to run a 'square scan', a particular scan where S_1 and S_2 are stage attributes. A square scan is the most commonly used scan in both RITA, a cryogenic version of RITA and a confocal set-up. It is currently the only scan that can be started using the GUI. A SUPER-GUI session can be started by running the *launch_gui* located in the root directory.

e) Experiment class

The *Experiment* class is responsible for configuring the functions that will be used to take and save data. In a configuration file, described in Section 7.2.3, users define the instruments they want to use and the attributes of those instruments that they want to track. For example a user may specify they want to use a lock-in detector and they want to keep track of the 'r' and 'theta' attributes (the attributes tracked in the Si:Se^+ 1s:Γ_7 lifetime measurement) as well as the sensitivity setting. An instance of the *Experiment* class uses this information to define a *measure* function that can be called by scans. By implementing this middle-man class, it allows our scans to be entirely general and agnostic to the physical instrument being used. This drastically reduces the amount of work that needs to be done as we expand to different set-ups.

The *Experiment* class also contains methods that scans can access to write to either a '.csv' (comma delimited file compatible with excel) file, or to the database (Section 7.2.2).

An *Experiment* instance will save any data recorded in a temporary file, and is responsible for saving all software-related meta-data ensuring no important data is lost if an error occurs unexpectedly.

f) Database class

The *Database* class controls access to the database, which is hosted on a local server. The database structure is shown in Figure 7.3 with each block representing a table with the same name as the header, and each row representing an entry field. Each of the 12 tables have a unique identifier (Id). Tables are linked together using these unique Ids, shown in Figure 7.3 as arrows. The tables are populated automatically using methods from the *Database* class. Most entries are read-only for all users except the owner of the database to ensure our data remains un-corrupted. However, some fields have the ability to be edited after the experiment has finished, such as description and comment fields.

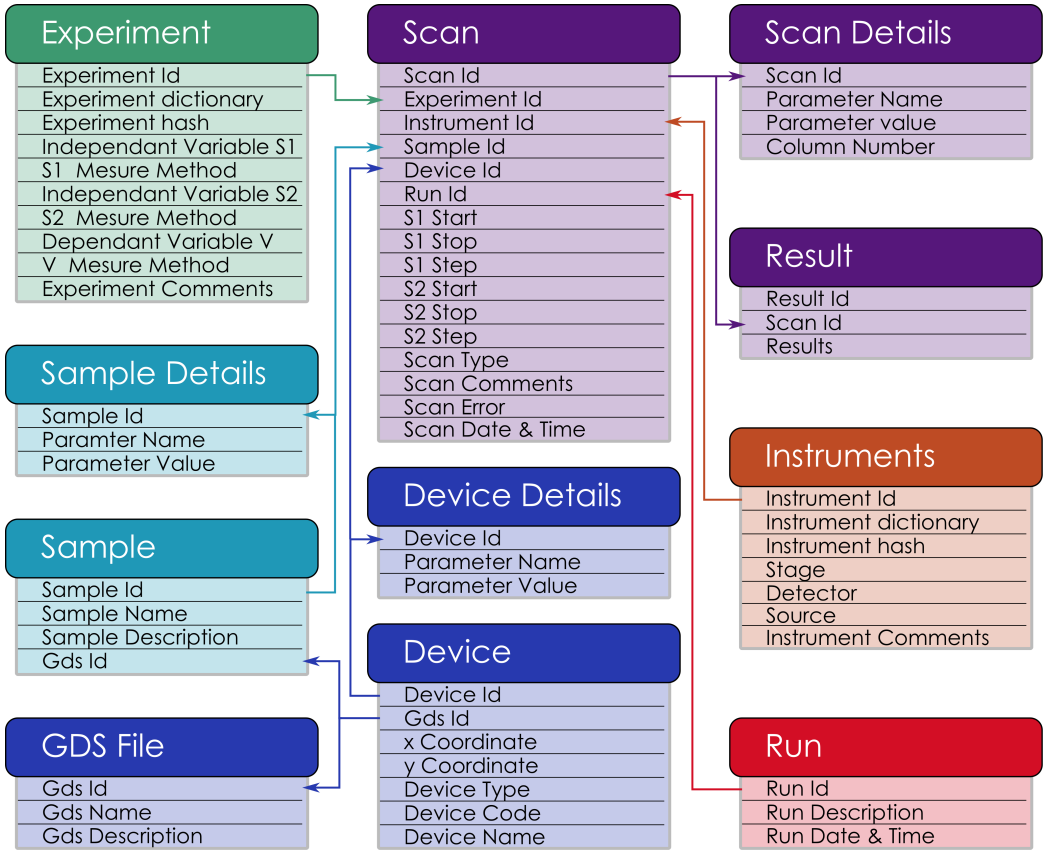

Figure 7.3: Diagram of the 12 tables that make up the database. Full descriptions of each table are given in the main text. Each table is represented by a block with the name in the header. The rows represent information fields that are populated using an instance of the *Database* class. Arrows represent linked field, where the base of the arrow indicates which table the field was generated. Families of tables are linked using color to represent tables with a similar theme.

i - Instruments: The instruments table is shown in orange in Figure 7.3. It contains information about the physical system that SUPER took data with. It is populated from the 'Instruments' dictionary in a configuration file, described in Section 7.2.3. An Instruments dictionary is 'hashed' upon import, a value is assigned to the instrument dictionary based on the contents of the dictionary. We populate a new entry in the Instruments table only when the hash is different. This allows a user performing analysis to easily and efficiently find all the entries in all the tables that are linked to a particular physical configuration.

ii - Experiment: The Experiment table is shown in green in Figure 7.3. The instruments and attributes of the instruments that were measured during the SUPER session (labeled 'Measure Method' in Figure 7.3) are all stored in the Experiment table. Namely, an experiment is defined by the set S_1, S_2, and V, along with any other static or dynamic parameters that are tracked. It is populated from the 'Experiment' dictionary in configuration files, described in Section 7.2.3. An Experiment dictionary is 'hashed' upon import like an Instruments dictionary. This allows a user performing analysis to easily and efficiently find all the entries in all the tables that are linked to a particular Experiment.

iii - Sample and Sample Details: The Sample table, in aquamarine in Figure 7.3, stores information on the physical object being probed by the set-up. A sample is not a strictly defined physical object. A sample on RITA would be an SOI wafer with photonics devices, whereas a sample in a confocal microscopy set-up might be a pure silicon sample with optically active defect sites in it. The Sample Details table stores meta-data on the sample with the same 'Sample Id' entry of its corresponding Sample entry. An example of a Samples Details entry would be whether or not a photonics chip has an oxide layer. For photonics samples associated with a GDS design file, a 'GDS Id' field links the sample to the tables that store information on the design.

iv - Design File, Device, Device Details: The Design File table, in dark blue in Figure 7.3, stores basic information on the name and description of the GDS file used to fabricate a photonics sample. GDS files are loaded into the database using the *gds_to_database* script located in the *root* module of SUPER, described in Section 7.2.3. The *gds_to_database* script from the *root* module uses the functionality in the *Database* class to ensure that a specific design file is only ever loaded into the database once. Basic information about the the specific devices on the processed sample, like their position on the chip and their names, are stored in the Device table. The Device Table is accessed during sessions of SUPER to obtain relative coordinates of devices for alignment purposes. Device parameters are extracted from the device name and stored in the Device Details table. The Device Details table links parameters with devices through the Device ID field shared by the GDS File table and the Device table.

v - Scan, Scan Details, and Result: The Scan table, shown in purple in Figure 7.3, stores all the metadata about a scan. It is the central table through which all other tables are linked. It contains fields for Experiment ID, Instrument ID, Sample ID and Device ID to associate all table entries that are relevant to the specific scan, identified by its Scan ID. The Scan ID field links the scan to both a Results and a Scan Details table. The Results table contains only one field of data which is the Results field. The Results field stores an array of variable size with structure that is recorded in the Scan Details table.

vi - Run: Many scans may be associated with one session of SUPER. For example, one typical use of SUPER is to iterate over all devices on a chip and perform two scans: One to measure the transmission as function of position near a device, and a second to perform an FTIR measurement at the maximum transmission point. Each of these scans for each device will have separate entries in the Scan family of tables (purple in Figure 7.3). A Run ID is automatically generated to associate these scans with the one SUPER session they occurred within. The Run Id, a description of the run, and the start date and time of the run are all recorded in the Run table.

7.2.3 Level 3: root directory

The root directory is the entrance point for a user. It is the folder that contains all of SUPER. Scripts in the root directory are designed for easy access by a user or user-developer. All scripts at the root level have a 'User Setup' Section that can be safely edited by anyone.

a) analysis package

The *analysis* module contains all analysis scripts used to interpret and visualize data.

b) tests package

The *tests* package contains many packages with modules that test specific parts of SUPER. There are two main types of test modules. The source code tests (labeled *tests_src_* in Figure 7.3) verify the logic of scripts and ensure that interactions between classes remain the same when any edits to the source code are implemented. The hardware tests (labeled *tests_hardware* in Figure 7.3) are designed to check that hardware parameters, such as soft limits and end-of-travel-flags, act as expected.

c) configuration files

Configuration files are stored in a subfolder of root. We use configuration files as a way of introducing customization for a user. User-defined configuration files list which set of instruments are to be used and which attributes of these instruments to record. The configuration files include multiple entries defined through indentation, see Section 7.3 for an example.

i - Instruments entry: Each configuration file contains one instruments entry that provides details on the instruments being used and which attributes of those instruments that will be recorded. For example, a RITA configuration file would list the lead-screw actuated stages where the cryo-RITA would list the piezo-actuated stages. Both room-temperature and cryogenic-temperature set-ups would list 'x', 'y', and 'z' as attributes to be measured. This entry is used by an instance of the *Instruments* class (Section 7.2.1) to determine which specific instrument instances to initialize.

ii - Experiments entry: Each configuration file that is used in a scan will contain an experiment entry. The experiment entry specifies which attributes of which instruments in the instruments dictionary will be the S_1, S_2 and V of the scan. The experiment entry also identifies any other attributes/instruments the user wants to measure. This entry is used by an instance of the *Experiment* class (Section 7.2.2) to create the *measure* method that will be used by the scan.

d) run scripts

The root directory contains all the *run* scripts. These scripts begin automated sessions of SUPER that perform repeated sequences of scans. The User Setup portion of a *run* script typically requires a user to specify the configuration file they want to use, where they want to save the data (database or local .csv file), and what parts of the sample they want to perform the tests on. For example, a run script in RITA may require the user to specify which devices on a photonic chip they want to measure.

d) gds_to_database script

The *gds_to_database* script requires a user to specify a GDS design file and loads it into the database. Safety checks are performed in this script that ensure previous information about a fabricated chip is not overwritten in the database. Running this script with a new design file is also used to verify that all devices are labeled in the proper format, and ensure no device metadata is lost once the chip has been fabricated.

f) launch_gui script

The *launch_gui* script can be run without modification directly from the command line to begin a GUI session that will run SUPER.

7.3 Detailed example

Here I present a detailed example in order to illustrate how a user can perform an experiment using SUPER. One example of efficient use of SUPER is to measure the transmission

and frequency response of all calibration devices printed on a new sample. In this Section snippets of python code will be presented where comment lines begin with #.

Loading a design file: The first step to any experiment performed on a new photonic chip is to load the design file into the database. Within the *gds_to_database.py* file, the user must specify the the design file in *.gds* format that they would like to load.

```
""" USER SECTION """
# The path and file name of the GDS to be added to the database.
GDS_FILE = r"\\path\\to\\gds.gds"
```

Once edited, loading the design into the database can be done by running

```
\SUPER > python gds_to_database.py
```

Each device on the gds file has a name and an x and y coordinate corresponding to the location relative to other devices on the chip. The combination of the design file name, x coordinate and y coordinate of each device must be unique to be loaded into the database and an error will notify the user if they are attempting to load a design file that is already stored in the database.

Identifying relevant devices: Once the design file is loaded into the database, the user can then search for the Device Ids of the structures they want to measure. For example, if the user would like to measure a subset of calibration devices, they can search the Device Parameters table to recover all the Device Ids that are associated with structures that were identified as calibration structures by the designer of the chip.

Using a run script and configuration file: Run scripts have been written to accommodate a variety of tests used to characterize photonic devices and RITA as a system. For the purpose of taking transmission and frequency response data from calibration devices, the *chiprun.py* file displayed in full in Appendix B can be used. Within the run script, the user must specify the configuration file that should be used to intialize instruments and define the experimental parameters. In this example, the filename of the configuration file *calibration_study.yaml*.

```
""" User Setup """
# Instruments and experiments are loaded from a config file (.yaml).
inst = Instruments('config_files/calibration_study.yaml')
```

The configuration file is formated to YAML standards [89] where indentation levels denote sub-entries. The first main entry in a configuration file is the *instruments* entry that specifies the names,

```
# Define instrument dictionary
instruments:
  stages:
      micronix_xyz: # Stage name
  sources:
      chopper: # Source name
  detectors:
      lockin: # Detector name
```

initialization parameters,

```
    micronix_xyz:
        # parameters necessary for initialization
        initparams:
          x_limit: -15, 15
          y_limit: -10, 10
          z_limit: 0, 22.709
          port: COM3
```

and attributes to be measured with their specific measurement methods.

```
        # What do you want to measure and how do you want to measure it?
        access:
          # what: how
          x: get_position_x
          y: get_position_y
          z: get_position_z
```

The instruments defined in the instruments entry are all the instruments needed to perform the run, however some scans only need a subset of the instruments. These specific subsets are defined within 'experiment entries'. The subsequent main entries are experiment entries. An experiment entry is defined within the configuration file and specifies subsets of instruments and which variables the user wants to keep track of. One run will contain multiple experiment entries. For example, the main experiment object has attributes according to the experiment entry below.

```
# Define first experiment object
experiment_sqsc: # your own personal name for the experiment
  # name of the instrument you want to use to measure s1 dimension
  ↪ (required)
  s1_instrument_name: micronix_xyz
  # name of the variable you want to measure (must match one key in
  ↪ instruments[instrument name]['access'])
  s1_name: x                        # *(key)
  # name of the instrument you want to use to measure s2 dimension
  ↪ (optional)
  s2_instrument_name: micronix_xyz
  # name of the variable you want to measure (must match one key in
  ↪ instruments[instrument name]['access'])
  s2_name: y
  # name of the instrument you want to use to measure v - dependant
  ↪ dimension (required)
  v_instrument_name: lockin
  # name of the variable you want to measure (must match one key in
  ↪ instruments[instrument name]['access'])
  v_name: power
```

The next edit to *chiprun.py* is to associate experiment entries to their respective variables within the run script.

```
# exp_main is used for general movement, squarescans and gradient scans.
exp_main = Experiment(inst, 'experiment_main', write_to='production
↪ database')
```

Once the instruments configuration has been specified in the configuration file, the following edits to *chiprun.py* are used to configure the run to the users needs. The user must specify which devices they want to measure. Different options exist for this in *chiprun.py*. One option is presented below,

```
# Select which filtering option you want to specify the devices you want
↪ to measure.
# Set "option" to the option number you want to run. Some options require
# parameters to be set
option = 6
```

```
...

# Option 6: get all the devices with a particular type, or code.
if option == 6:
    # measure all devices that are calibration structures
    device_type = 'cal'
```

Finally, the user can run the script using

```
\SUPER > python chiprun.py
```

7.4 Current status of SUPER

SUPER is an ongoing project that is updated regularly with bug-fixes and enhancements. A working version of SUPER is currently operational on three separate set-ups. It is used with RITA, a cryogenically compatible version of RITA, and a cryogenically compatible confocal set-up. We are currently in the testing phase of using SUPER to control a room-temperature confocal set-up. Within the first two months of operation, SUPER successfully controlled the collection of an average of 124 MB of data per week. All data presented in Chapter 6 was collected using SUPER. Recently, SUPER was adapted for use within a unanticipated setting, to perform 'hole burning' experiments like those described by Friedrich [58]. Encouragingly, this latest adaptation demonstrates SUPER's versatility, indicating that SUPER could be adapted for use outside of our laboratory in other research environments.

7.5 Contributions to SUPER

The ongoing project of SUPER is supported by many researchers. The team of developers that worked on the version of SUPER that is presented here are, in alphabetical order: Laurent Bergeron, Camille Chartrand, Adam DeAbreu, Stephen Harrigan, Joshua Kanaganayagam, James Klein, Alex Kurjikan, Kevin J. Morse, Timothy Richards, Leea Stott. My personal contribution was in the development of the SUPER prototype, initial design of the architecture, and co-lead of the development team along with Kevin J. Morse.

Chapter 8

Conclusion and summary

Singly ionized selenium donors in silicon, Si:Se^+, have an optically accessible spin degree of freedom. In order to determine the radiative efficiency of the optical degree of freedom, we performed concentration modulation spectroscopy to measure the lifetime of the 1s:Γ_7 electronic orbital state in Si:Se^+. We measured a lifetime of 7.7(4) ns, corresponding to a radiative efficiency of only 0.80(9)% for the 1s:$\Gamma_7 \Rightarrow$ 1s:A transition. This invalidates previous claims that the centre was an efficient emitter and eliminates the possibility of performing direct optical readout of the spin state without making use of density-of-states engineering through photonic cavities.

The spin degree of freedom of the Si:Se^+ system can still be exploited as an optically accessible qubit within a larger photonics architechture. We built a measurement system (RITA) to efficiently characterize the material properties of SOI operating in the MIR at room temperature such as photonic cavities. The software that runs RITA, SUPER, was developed to be generally applicable to RITA-like systems. This expedites the transition from room-temperature characterization of photonics to cryogenic temperature characterization of photonics.

We will be able to use the cryogenic adaptation of RITA to measure how well implanted or diffused Se^+ integrates with photonic devices. Once we can reliably build cavities with Se^+ located near the mode maximum we can begin to tune the cavities through localized oxide growth or tune the transition frequency of the optical degree of freedom through strain or electric field. Fortunately, SUPER can be used to control these procedures, expediting the process of developing these procedures.

The ultimate goal is to achieve strong coupling in the cavity-qubit system in order to perform indirect optical readout of the Si:Se^+ spin-state. Such a spin-photon interface has applications as the foundation of a global quantum computing network.

Bibliography

[1] Alberto Peruzzo, Jarrod McClean, Peter Shadbolt, Man-Hong Yung, Xiao-Qi Zhou, Peter J. Love, Alán Aspuru-Guzik, and Jeremy L. O'Brien. A variational eigenvalue solver on a photonic quantum processor. *Nature Communications*, 5(1):4213, dec 2014. ISSN 2041-1723. doi: 10.1038/ncomms5213. URL `http://www.nature.com/articles/ncomms5213`.

[2] Chao-Yang Lu, Daniel E. Browne, Tao Yang, and Jian-Wei Pan. Demonstration of a Compiled Version of Shor's Quantum Factoring Algorithm Using Photonic Qubits. *Physical Review Letters*, 99(25):250504, dec 2007. ISSN 0031-9007. doi: 10.1103/PhysRevLett.99.250504. URL `https://link.aps.org/doi/10.1103/PhysRevLett.99.250504`.

[3] T. D. Ladd, F. Jelezko, R. Laflamme, Y. Nakamura, C. Monroe, and J. L. O'Brien. Quantum computers. *Nature*, 464(7285):45–53, mar 2010. ISSN 0028-0836. doi: 10.1038/nature08812. URL `http://www.nature.com/articles/nature08812`.

[4] F. Bloch. Nuclear induction. *Phys. Rev.*, 70:460–474, Oct 1946. doi: 10.1103/PhysRev.70.460. URL `https://link.aps.org/doi/10.1103/PhysRev.70.460`.

[5] A. E. Siegman. *Lasers*. University Science Books, 1986. ISBN 0935702113. URL `https://books.google.ca/books/about/Lasers.html?id=1BZVwUZLTkAC{&}redir{_}esc=y`.

[6] J. Kelly, R. Barends, A. G. Fowler, A. Megrant, E. Jeffrey, T. C. White, D. Sank, J. Y. Mutus, B. Campbell, Yu Chen, Z. Chen, B. Chiaro, A. Dunsworth, I.-C. Hoi, C. Neill, P. J. J. O'Malley, C. Quintana, P. Roushan, A. Vainsencher, J. Wenner, A. N. Cleland, and John M. Martinis. State preservation by repetitive error detection in a superconducting quantum circuit. *Nature*, 519(7541):66–69, mar 2015. ISSN 0028-0836. doi: 10.1038/nature14270. URL `http://www.nature.com/articles/nature14270`.

[7] Jerry M. Chow, Jay M. Gambetta, A. D. Córcoles, Seth T. Merkel, John A. Smolin, Chad Rigetti, S. Poletto, George A. Keefe, Mary B. Rothwell, J. R. Rozen, Mark B. Ketchen, and M. Steffen. Universal Quantum Gate Set Approaching Fault-Tolerant Thresholds with Superconducting Qubits. *Physical Review Letters*, 109(6):060501, aug 2012. ISSN 0031-9007. doi: 10.1103/PhysRevLett.109.060501. URL `https://link.aps.org/doi/10.1103/PhysRevLett.109.060501`.

[8] D Nigg, M Müller, E A Martinez, P Schindler, M Hennrich, T Monz, M A Martin-Delgado, and R Blatt. Quantum computations on a topologically encoded qubit. *Science (New York, N.Y.)*, 345(6194):302–5, jul 2014. ISSN 1095-9203. doi: 10.1126/science.1253742. URL `http://www.ncbi.nlm.nih.gov/pubmed/24925911`.

[9] Thomas Monz, Daniel Nigg, Esteban A Martinez, Matthias F Brandl, Philipp Schindler, Richard Rines, Shannon X Wang, Isaac L Chuang, and Rainer Blatt. Realization of a scalable Shor algorithm. *Science (New York, N.Y.)*, 351(6277): 1068–70, mar 2016. ISSN 1095-9203. doi: 10.1126/science.aad9480. URL `http://www.ncbi.nlm.nih.gov/pubmed/26941315`.

[10] E. Knill, R. Laflamme, and G. J. Milburn. A scheme for efficient quantum computation with linear optics. *Nature*, 409(6816):46–52, jan 2001. ISSN 0028-0836. doi: 10.1038/35051009. URL `http://www.nature.com/articles/35051009`.

[11] Pieter Kok, W. J. Munro, Kae Nemoto, T. C. Ralph, Jonathan P. Dowling, and G. J. Milburn. Linear optical quantum computing with photonic qubits. *Reviews of Modern Physics*, 79(1):135–174, jan 2007. ISSN 0034-6861. doi: 10.1103/RevModPhys.79.135. URL `https://link.aps.org/doi/10.1103/RevModPhys.79.135`.

[12] Kristiaan De Greve, Leo Yu, Peter L. McMahon, Jason S. Pelc, Chandra M. Natarajan, Na Young Kim, Eisuke Abe, Sebastian Maier, Christian Schneider, Martin Kamp, Sven Höfling, Robert H. Hadfield, Alfred Forchel, M. M. Fejer, and Yoshihisa Yamamoto. Quantum-dot spin–photon entanglement via frequency downconversion to telecom wavelength. *Nature*, 491(7424):421–425, nov 2012. ISSN 0028-0836. doi: 10.1038/nature11577. URL `http://www.nature.com/articles/nature11577`.

[13] Lucio Robledo, Lilian Childress, Hannes Bernien, Bas Hensen, Paul F. A. Alkemade, and Ronald Hanson. High-fidelity projective read-out of a solid-state spin quantum register. *Nature*, 477(7366):574–578, sep 2011. ISSN 0028-0836. doi: 10.1038/nature10401. URL `http://www.nature.com/articles/nature10401`.

[14] Manjin Zhong, Morgan P. Hedges, Rose L. Ahlefeldt, John G. Bartholomew, Sarah E. Beavan, Sven M. Wittig, Jevon J. Longdell, and Matthew J. Sellars. Optically addressable nuclear spins in a solid with a six-hour coherence time. *Nature*, 517 (7533):177–180, jan 2015. ISSN 0028-0836. doi: 10.1038/nature14025. URL `http://www.nature.com/articles/nature14025`.

[15] Brendon C Rose, Ding Huang, Zi-Huai Zhang, Paul Stevenson, Alexei M Tyryshkin, Sorawis Sangtawesin, Srikanth Srinivasan, Lorne Loudin, Matthew L Markham, Andrew M Edmonds, Daniel J Twitchen, Stephen A Lyon, and Nathalie P de Leon. Observation of an environmentally insensitive solid-state spin defect in diamond. *Science (New York, N.Y.)*, 361(6397):60–63, jul 2018. ISSN 1095-9203. doi: 10.1126/science.aao0290. URL `http://www.ncbi.nlm.nih.gov/pubmed/29976820`.

[16] David J. Christle, Paul V. Klimov, Charles F. de las Casas, Krisztián Szász, Viktor Ivády, Valdas Jokubavicius, Jawad Ul Hassan, Mikael Syväjärvi, William F. Koehl, Takeshi Ohshima, Nguyen T. Son, Erik Janzén, Ádám Gali, and David D. Awschalom. Isolated Spin Qubits in SiC with a High-Fidelity Infrared Spin-to-Photon Interface. *Physical Review X*, 7(2):021046, jun 2017. ISSN 2160-3308. doi: 10.1103/PhysRevX.7.021046. URL `http://link.aps.org/doi/10.1103/PhysRevX.7.021046`.

[17] Matthias Widmann, Sang-Yun Lee, Torsten Rendler, Nguyen Tien Son, Helmut Fedder, Seoyoung Paik, Li-Ping Yang, Nan Zhao, Sen Yang, Ian Booker, Andrej Denisenko, Mohammad Jamali, S. Ali Momenzadeh, Ilja Gerhardt, Takeshi Ohshima, Adam Gali,

Erik Janzén, and Jörg Wrachtrup. Coherent control of single spins in silicon carbide at room temperature. *Nature Materials*, 14(2):164–168, feb 2015. ISSN 1476-1122. doi: 10.1038/nmat4145. URL http://www.nature.com/articles/nmat4145.

[18] Xiayu Linpeng, Maria L. K. Viitaniemi, Aswin Vishnuradhan, Y. Kozuka, Cameron Johnson, M. Kawasaki, and Kai-Mei C. Fu. Coherence properties of shallow donor qubits in ZnO. feb 2018. URL http://arxiv.org/abs/1802.03483.

[19] Floris A Zwanenburg, Andrew S Dzurak, Andrea Morello, Michelle Y Simmons, Lloyd C L Hollenberg, Gerhard Klimeck, Sven Rogge, Susan N Coppersmith, and Mark A Eriksson. Silicon Quantum Electronics. 2013.

[20] Charles. Kittel. *Introduction to solid state physics*. Wiley, 2005. ISBN 047141526X.

[21] W. Kohn and J. M. Luttinger. Theory of Donor States in Silicon. *Physical Review*, 98 (4):915–922, may 1955. ISSN 0031-899X. doi: 10.1103/PhysRev.98.915. URL https://link.aps.org/doi/10.1103/PhysRev.98.915.

[22] H. G. Grimmeiss, E. Janzén, and K. Larsson. Multivalley spin splitting of 1 s states for sulfur, selenium, and tellurium donors in silicon. *Physical Review B*, 25(4):2627–2632, feb 1982. ISSN 0163-1829. doi: 10.1103/PhysRevB.25.2627. URL https://link.aps.org/doi/10.1103/PhysRevB.25.2627.

[23] B. E. Kane. A silicon-based nuclear spin quantum computer. *Nature*, 393(6681):133–137, may 1998. ISSN 00280836. doi: 10.1038/30156. URL http://www.nature.com/doifinder/10.1038/30156.

[24] Guilherme Tosi, Fahd A. Mohiyaddin, Vivien Schmitt, Stefanie Tenberg, Rajib Rahman, Gerhard Klimeck, and Andrea Morello. Silicon quantum processor with robust long-distance qubit couplings. *Nature Communications*, 8(1):450, dec 2017. ISSN 2041-1723. doi: 10.1038/s41467-017-00378-x. URL http://www.nature.com/articles/s41467-017-00378-x.

[25] Roberto Lo Nardo, Gary Wolfowicz, Stephanie Simmons, Alexei M Tyryshkin, Helge Riemann, Nikolai V Abrosimov, Peter Becker, Hans-Joachim Pohl, Michael Steger, Stephen A Lyon, Mike L W Thewalt, and John J L Morton. Spin relaxation and donor-acceptor recombination of Se + in 28-silicon. *PHYSICAL REVIEW B*, 92: 165201, 2015. doi: 10.1103/PhysRevB.92.165201. URL https://www.ucl.ac.uk/qsd/publications/paper82.pdf.

[26] M Steger, A Yang, M L W Thewalt, M Cardona, H Riemann, N V Abrosimov, M F Churbanov, A V Gusev, A D Bulanov, I D Kovalev, A K Kaliteevskii, O N Godisov, P Becker, H.-J Pohl, E E Haller, and J W Ager Iii. High-resolution absorption spectroscopy of the deep impurities S and Se in 28 Si revealing the 77 Se hyperfine splitting. doi: 10.1103/PhysRevB.80.115204. URL https://journals.aps.org/prb/pdf/10.1103/PhysRevB.80.115204.

[27] E. Janzén, R. Stedman, G. Grossmann, and H. G. Grimmeiss. High-resolution studies of sulfur- and selenium-related donor centers in silicon. *Physical Review B*, 29(4): 1907–1918, feb 1984. ISSN 0163-1829. doi: 10.1103/PhysRevB.29.1907. URL https://link.aps.org/doi/10.1103/PhysRevB.29.1907.

[28] Martin A. Green. Intrinsic concentration, effective densities of states, and effective mass in silicon. *Journal of Applied Physics*, 67(6):2944–2954, mar 1990. ISSN 0021-8979. doi: 10.1063/1.345414. URL http://aip.scitation.org/doi/10.1063/1.345414.

[29] Kevin J. Morse, Rohan J. S. Abraham, Adam DeAbreu, Camille Bowness, Timothy S. Richards, Helge Riemann, Nikolay V. Abrosimov, Peter Becker, Hans-Joachim Pohl, Michael L. W. Thewalt, and Stephanie Simmons. A photonic platform for donor spin qubits in silicon. *Science Advances*, 3(7), 2017. URL http://advances.sciencemag.org/content/3/7/e1700930.

[30] A. DeAbreu, C. Bowness, R. J. S. Abraham, A. Medvedova, K. J. Morse, H. Riemann, N. V. Abrosimov, P. Becker, H.-J. Pohl, M. L. W. Thewalt, and S. Simmons. Characterization of the Si:Se+ spin-photon interface. *ArXiv e-prints*, September 2018.

[31] David A. Hopper, Henry J. Shulevitz, and Lee C. Bassett. Spin readout techniques of the nitrogen-vacancy center in diamond. *Micromachines*, 9(9), 2018. ISSN 2072-666X. doi: 10.3390/mi9090437. URL http://www.mdpi.com/2072-666X/9/9/437.

[32] P. T. Landsberg. Non-Radiative Transitions in Semiconductors. *physica status solidi (b)*, 41(2):457–489, jan 1970. ISSN 03701972. doi: 10.1002/pssb.19700410202. URL http://doi.wiley.com/10.1002/pssb.19700410202.

[33] E. M. Purcell, H. C. Torrey, and R. V. Pound. Resonance Absorption by Nuclear Magnetic Moments in a Solid. *Physical Review*, 69(1-2):37–38, jan 1946. ISSN 0031-899X. doi: 10.1103/PhysRev.69.37. URL https://link.aps.org/doi/10.1103/PhysRev.69.37.

[34] P. Yao, V.S.C. Manga Rao, and S. Hughes. On-chip single photon sources using planar photonic crystals and single quantum dots. *Laser & Photonics Reviews*, 4(4):499–516, jul 2009. ISSN 18638880. doi: 10.1002/lpor.200810081. URL http://doi.wiley.com/10.1002/lpor.200810081.

[35] A. Laucht, T. Günthner, S. Pütz, R. Saive, S. Frédérick, N. Hauke, M. Bichler, M.-C. Amann, A. W. Holleitner, M. Kaniber, and J. J. Finley. Broadband Purcell enhanced emission dynamics of quantum dots in linear photonic crystal waveguides. *Journal of Applied Physics*, 112(9):093520, nov 2012. ISSN 0021-8979. doi: 10.1063/1.4764923. URL http://aip.scitation.org/doi/10.1063/1.4764923.

[36] S. Hughes. Enhanced single-photon emission from quantum dots in photonic crystal waveguides and nanocavities. *Optics Letters*, 29(22):2659, nov 2004. ISSN 0146-9592. doi: 10.1364/OL.29.002659. URL https://www.osapublishing.org/abstract.cfm?URI=ol-29-22-2659.

[37] Dirk Englund, Brendan Shields, Kelley Rivoire, Fariba Hatami, Jelena Vucckovic, Hongkun Park, and Mikhail D. Lukin. Deterministic Coupling of a Single Nitrogen Vacancy Center to a Photonic Crystal Cavity. *Nano Letters*, 10(10):3922–3926, oct 2010. ISSN 1530-6984. doi: 10.1021/nl101662v. URL http://pubs.acs.org/doi/abs/10.1021/nl101662v.

[38] T Lindström, C H Webster, J E Healey, M S Colclough, C M Muirhead, and A Ya Tzalenchuk. Related content Circuit QED with a flux qubit strongly coupled to

a coplanar transmission line resonator. *Supercond. Sci. Technol*, 20:814–821, 2007. doi: 10.1088/0953-2048/20/8/016. URL http://iopscience.iop.org/article/10.1088/0953-2048/20/8/016/pdf.

[39] Hamidreza Siampour and Yaping Dan. Si nanowire phototransistors at telecommunication wavelengths by plasmon-enhanced two-photon absorption. *Optics Express*, 24(5):4601, mar 2016. ISSN 1094-4087. doi: 10.1364/OE.24.004601. URL https://www.osapublishing.org/abstract.cfm?URI=oe-24-5-4601.

[40] David Thomson, Aaron Zilkie, John E Bowers, Tin Komljenovic, Graham T Reed, Laurent Vivien, Delphine Marris-Morini, Eric Cassan, Léopold Virot, Jean-Marc Fédéli, Jean-Michel Hartmann, Jens H Schmid, Dan-Xia Xu, Frédéric Boeuf, Peter O'Brien, Goran Z Mashanovich, and M Nedeljkovic. Roadmap on silicon photonics. *Journal of Optics*, 18(7):073003, jul 2016. ISSN 2040-8978. doi: 10.1088/2040-8978/18/7/073003. URL http://stacks.iop.org/2040-8986/18/i=7/a=073003?key=crossref.4a5bbda045e84b8801eba3e3605b6fb2.

[41] G. T. Reed, G. Mashanovich, F. Y. Gardes, and D. J. Thomson. Silicon optical modulators. *Nature Photonics*, 4(8):518–526, aug 2010. ISSN 1749-4885. doi: 10.1038/nphoton.2010.179. URL http://www.nature.com/articles/nphoton.2010.179.

[42] Hongtao Lin, Lan Li, Fei Deng, Chaoying Ni, Sylvain Danto, J. David Musgraves, Kathleen Richardson, and Juejun Hu. Demonstration of mid-infrared waveguide photonic crystal cavities. *Optics Letters*, 38(15):2779, aug 2013. ISSN 0146-9592. doi: 10.1364/OL.38.002779. URL https://www.osapublishing.org/abstract.cfm?URI=ol-38-15-2779.

[43] Vivek Singh, Pao Tai Lin, Neil Patel, Hongtao Lin, Lan Li, Yi Zou, Fei Deng, Chaoying Ni, Juejun Hu, James Giammarco, Anna Paola Soliani, Bogdan Zdyrko, Igor Luzinov, Spencer Novak, Jackie Novak, Peter Wachtel, Sylvain Danto, J David Musgraves, Kathleen Richardson, Lionel C Kimerling, and Anuradha M Agarwal. Mid-infrared materials and devices on a Si platform for optical sensing. *Science and Technology of Advanced Materials*, 15(1):014603, feb 2014. ISSN 1468-6996. doi: 10.1088/1468-6996/15/1/014603. URL http://www.tandfonline.com/doi/full/10.1088/1468-6996/15/1/014603.

[44] Lumerical - High-Performance Nanophotonic Simulation Software. URL https://www.lumerical.com/.

[45] S Perkowitz', D G Seller, and W M Duncan. Optical Characterization in Microelectronics Manufacturing. Technical Report 5. URL https://pdfs.semanticscholar.org/1801/1025ebdd039bcfcfa667b30f681a838ceaf4.pdf.

[46] Yoon-Suk Kim, Martijn Marsman, Georg Kresse, Fabien Tran, and Peter Blaha. Towards efficient band structure and effective mass calculations for III-V direct band-gap semiconductors. *Physical Review B*, 82(20):205212, nov 2010. ISSN 1098-0121. doi: 10.1103/PhysRevB.82.205212. URL https://link.aps.org/doi/10.1103/PhysRevB.82.205212.

[47] Sokrates T. Pantelides. The electronic structure of impurities and other point defects in semiconductors. *Reviews of Modern Physics*, 50(4):797–858, oct 1978. ISSN 0034-6861. doi: 10.1103/RevModPhys.50.797. URL https://link.aps.org/doi/10.1103/RevModPhys.50.797.

[48] Yang Song, Oleg Chalaev, and Hanan Dery. Donor-Driven Spin Relaxation in Multivalley Semiconductors. 2014. doi: 10.1103/PhysRevLett.113.167201. URL https://journals.aps.org/prl/pdf/10.1103/PhysRevLett.113.167201.

[49] Theodore G. Castner. Orbach Spin-Lattice Relaxation of Shallow Donors in Silicon. *Physical Review*, 155(3):816–825, mar 1967. ISSN 0031-899X. doi: 10.1103/PhysRev.155.816. URL https://link.aps.org/doi/10.1103/PhysRev.155.816.

[50] Leonard Hanssen, Simon Kaplan, and Raju Datla. Infrared Optical Properties of Materials. doi: 10.6028/NIST.SP.250-94. URL http://dx.doi.org/10.6028/NIST.SP.250-94.

[51] Donald A. (Donald Allan) McQuarrie and John D. (John Douglas) Simon. *Physical chemistry : a molecular approach*. University Science Books, 1997. ISBN 0935702997.

[52] A. M. Tyryshkin, Zhi-Hui Wang, Wenxian Zhang, E. E. Haller, J. W. Ager, V. V. Dobrovitski, and S. A. Lyon. Dynamical Decoupling in the Presence of Realistic Pulse Errors. nov 2010. URL http://arxiv.org/abs/1011.1903.

[53] Malcolm H. Levitt. *Spin dynamics : basics of nuclear magnetic resonance*. Wiley, 2008. ISBN 0470511176.

[54] E. L. Hahn. Spin Echoes. *Physical Review*, 80(4):580–594, nov 1950. ISSN 0031-899X. doi: 10.1103/PhysRev.80.580. URL https://link.aps.org/doi/10.1103/PhysRev.80.580.

[55] A Bohm, N L Harshman, and H Walther. Relating the Lorentzian and exponential: Fermi's approximation, the Fourier transform and causality. Technical report, 2002. URL https://arxiv.org/pdf/quant-ph/0206145.pdf.

[56] B K Ridley. Multiphonon, non-radiative transition rate for electrons in semiconductors and insulators. *Journal of Physics C: Solid State Physics*, 11(11):2323–2341, jun 1978. ISSN 0022-3719. doi: 10.1088/0022-3719/11/11/023. URL http://stacks.iop.org/0022-3719/11/i=11/a=023?key=crossref.b6816b6d2c72a969e302d9d1dfd97ffb.

[57] L. (Leslie) Allen and J. H. Eberly. *Optical resonance and two-level atoms*. Dover, 1987. ISBN 0486655334.

[58] Josef Friedrich and Dietrich Haarer. Photochemical Hole Burning: A Spectroscopic Study of Relaxation Processes in Polymers and Glasses. *Angewandte Chemie International Edition in English*, 23(2):113–140, feb 1984. ISSN 0570-0833. doi: 10.1002/anie.198401131. URL http://doi.wiley.com/10.1002/anie.198401131.

[59] G. G. Devyatykh, A. D. Bulanov, A. V. Gusev, I. D. Kovalev, V. A. Krylov, A. M. Potapov, P. G. Sennikov, S. A. Adamchik, V. A. Gavva, A. P. Kotkov, M. F. Churbanov, E. M. Dianov, A. K. Kaliteevskii, O. N. Godisov, H. J. Pohl, P. Becker, H. Riemann, and N. V. Abrosimov. High-purity single-crystal monoisotopic silicon-28 for precise

determination of avogadro's number. *Doklady Chemistry*, 421(1):157–160, Jul 2008. ISSN 1608-3113. doi: 10.1134/S001250080807001X. URL https://doi.org/10.1134/S001250080807001X.

[60] G Dolling and R A Cowley. The thermo namic and optical germanium, silicon, diamond an arsenide. Technical report. URL http://iopscience.iop.org/article/10.1088/0370-1328/88/2/318/pdf.

[61] Gordon Davies. The optical properties of luminescence centres in silicon. *Physics Reports*, 176(3-4):83–188, may 1989. ISSN 0370-1573. doi: 10.1016/0370-1573(89)90064-1. URL https://www.sciencedirect.com/science/article/abs/pii/0370157389900641.

[62] . V N Mochalin, O Shenderova, D Ho, Y Gogotsi, ; P Maletinsky, S M Hong, M S Grinolds, B Hausmann, M D Lukin, R L Walsworth, M Loncar, A L Yacoby, ; T Wolf, P Neumann, K Nakamura, H Sumiya, T Ohshima, J Isoya, and J Wrachtrup. Ultralong spin coherence time in isotopically engineered diamond. *Nat. Nanotechnol*, 8(24):14, 2009. doi: 10.1364/OE.24.027715. URL http://dx.doi.org/10.1364/OE.24.027715.

[63] Faraz A. Inam, Michael D. W. Grogan, Mathew Rollings, Torsten Gaebel, Jana M. Say, Carlo Bradac, Tim A. Birks, William J. Wadsworth, Stefania Castelletto, James R. Rabeau, and Michael. J. Steel. Emission and Nonradiative Decay of Nanodiamond NV Centers in a Low Refractive Index Environment. *ACS Nano*, 7(5):3833–3843, may 2013. ISSN 1936-0851. doi: 10.1021/nn304202g. URL http://pubs.acs.org/doi/10.1021/nn304202g.

[64] J. Langley, R. A. Beaman, J. Baran, A. N. Davies, and W. Jeremy Jones. Concentration-modulated absorption spectroscopy. *Optics Letters*, 10(7):327, jul 1985. ISSN 0146-9592. doi: 10.1364/OL.10.000327. URL https://www.osapublishing.org/abstract.cfm?URI=ol-10-7-327.

[65] Albert Stolow, Arthur E. Bragg, and Daniel M. Neumark. Femtosecond time-resolved photoelectron spectroscopy. *Chemical Reviews*, 104(4):1719–1758, 2004. doi: 10.1021/cr020683w. URL https://doi.org/10.1021/cr020683w. PMID: 15080710.

[66] Zeev Burshtein. Radiative, nonradiative, and mixed-decay transitions of rare-earth ions in dielectric media. *Optical Engineering*, 49(9):091005, sep 2010. ISSN 0091-3286. doi: 10.1117/1.3483907. URL http://opticalengineering.spiedigitallibrary.org/article.aspx?doi=10.1117/1.3483907.

[67] Adam Deabreu. *Optical characterization of the Si:Se + spin-photon interface*. PhD thesis, Simon Fraser University, 2018. URL https://theses.lib.sfu.ca/file/thesis/4818.

[68] David Lide. CRC Handbook of Chemistry and Physics, 91th Edition. URL http://scienide2.uwaterloo.ca/{~}rleroy/c209/HBPC{_}atomic{_}isotope{_}masses.pdf.

[69] Serge Haroche and Daniel Kleppner. Cavity Quantum Electrodynamics. *Physics Today*, 42(1):24–30, jan 1989. ISSN 0031-9228. doi: 10.1063/1.881201. URL http://physicstoday.scitation.org/doi/10.1063/1.881201.

[70] Lukas Chrostowski and Michael Hochberg. *Silicon Photonics Design*. Cambridge University Press, Cambridge, 2015. ISBN 9781316084168. doi: 10.1017/CBO9781316084168. URL http://ebooks.cambridge.org/ref/id/CBO9781316084168.

[71] Yun Wang. Grating coupler design based on silicon-on-insulator. 2013. doi: 10.14288/1.0073806. URL https://open.library.ubc.ca/cIRcle/collections/ubctheses/24/items/1.0073806.

[72] Raji Shankar, Rick Leijssen, Irfan Bulu, and Marko Lončar. Mid-infrared photonic crystal cavities in silicon. *Optics express*, 19(6):5579–86, mar 2011. ISSN 1094-4087. doi: 10.1364/OE.19.005579. URL https://www.osapublishing.org/oe/abstract.cfm?uri=oe-19-6-5579http://www.ncbi.nlm.nih.gov/pubmed/21445197.

[73] A. Imamoğlu, H. Schmidt, G. Woods, and M. Deutsch. Strongly Interacting Photons in a Nonlinear Cavity. *Physical Review Letters*, 79(8):1467–1470, aug 1997. ISSN 0031-9007. doi: 10.1103/PhysRevLett.79.1467. URL https://link.aps.org/doi/10.1103/PhysRevLett.79.1467.

[74] J D Thompson, T G Tiecke, N P de Leon, J Feist, A V Akimov, M Gullans, A S Zibrov, V Vuletić, and M D Lukin. Coupling a single trapped atom to a nanoscale optical cavity. *Science (New York, N.Y.)*, 340(6137):1202–5, jun 2013. ISSN 1095-9203. doi: 10.1126/science.1237125. URL http://www.ncbi.nlm.nih.gov/pubmed/23618764.

[75] Seiko Mitachi, Ohishi Yasutake, and Shiro Takahashi. Fabrication of Low OH and Low Loss Fluoride Optical fibre. *Japanese Journal of Applied Physics*, 23(9):726–727, 1984. URL http://iopscience.iop.org/article/10.1143/JJAP.23.L726/pdf.

[76] Yurii A. Vlasov and Sharee J. McNab. Losses in single-mode silicon-on-insulator strip waveguides and bends. *Optics Express*, 12(8):1622, apr 2004. ISSN 1094-4087. doi: 10.1364/OPEX.12.001622. URL https://www.osapublishing.org/oe/abstract.cfm?uri=oe-12-8-1622.

[77] Qimin Quan, Parag B. Deotare, and Marko Loncar. Photonic crystal nanobeam cavity strongly coupled to the feeding waveguide. *Applied Physics Letters*, 96(20):203102, may 2010. ISSN 0003-6951. doi: 10.1063/1.3429125. URL http://aip.scitation.org/doi/10.1063/1.3429125.

[78] Donghwan Ahn, Jurgen Michel, and Lionel C. Kimerling. Evanescent Coupling Device Design for Waveguide-Integrated Group IV Photodetectors. *Journal of Lightwave Technology, Vol. 28, Issue 23, pp. 3387-3394*, 28(23):3387–3394, dec 2010. URL https://www.osapublishing.org/jlt/abstract.cfm?uri=jlt-28-23-3387.

[79] Alexander W. Fang, Richard Jones, Hyundai Park, Oded Cohen, Omri Raday, Mario J. Paniccia, and John E. Bowers. Integrated AlGaInAs-silicon evanescent race track laser and photodetector. *Optics Express*, 15(5):2315, mar 2007. ISSN 1094-4087. doi: 10.1364/OE.15.002315. URL https://www.osapublishing.org/oe/abstract.cfm?uri=oe-15-5-2315.

[80] Bradley J. Frey, Douglas B. Leviton, and Timothy J. Madison. Temperature-dependent refractive index of silicon and germanium. volume 6273, page 62732J.

International Society for Optics and Photonics, jun 2006. doi: 10.1117/12.672850. URL http://proceedings.spiedigitallibrary.org/proceeding.aspx?doi=10.1117/12.672850.

[81] Douglas B Leviton and Bradley J Frey. Temperature-dependent absolute refractive index measurements of synthetic fused silica. Technical report. URL https://arxiv.org/ftp/arxiv/papers/0805/0805.0091.pdf.

[82] Riccardo Marchetti, Cosimo Lacava, Ali Khokhar, Xia Chen, Ilaria Cristiani, David J. Richardson, Graham T. Reed, Periklis Petropoulos, and Paolo Minzioni. High-efficiency grating-couplers: demonstration of a new design strategy. *Scientific Reports*, 7(1): 16670, dec 2017. ISSN 2045-2322. doi: 10.1038/s41598-017-16505-z. URL http://www.nature.com/articles/s41598-017-16505-z.

[83] Minhao Pu, Liu Liu, Haiyan Ou, Kresten Yvind, and Jørn M. Hvam. Ultra-low-loss inverted taper coupler for silicon-on-insulator ridge waveguide. *Optics Communications*, 283(19):3678–3682, oct 2010. ISSN 0030-4018. doi: 10.1016/J.OPTCOM.2010.05.034. URL https://www.sciencedirect.com/science/article/pii/S0030401810005018?via{%}3Dihub.

[84] Shuo Sun, Hyochul Kim, Zhouchen Luo, Glenn S Solomon, and Edo Waks. A single-photon switch and transistor enabled by a solid-state quantum memory. *Science (New York, N.Y.)*, 361(6397):57–60, jul 2018. ISSN 1095-9203. doi: 10.1126/science.aat3581. URL http://www.ncbi.nlm.nih.gov/pubmed/29976819.

[85] J. (John) Wilson and J. F. B. Hawkes. *Optoelectronics : an introduction*. Prentice Hall Europe, 1998. ISBN 013103961X.

[86] CMC MIP si-photonics variant. https://www.cmc.ca/WhatWeOffer/Prototyping/HighPerformance/MIP/Si-Photonic.aspx. Accessed: 2018-11-21.

[87] V-Groove Chips. URL https://www.ozoptics.com/ALLNEW{_}PDF/DTS0077.pdf.

[88] Yun Wang, Xu Wang, Jonas Flueckiger, Han Yun, Wei Shi, Richard Bojko, Nicolas A. F. Jaeger, and Lukas Chrostowski. Focusing sub-wavelength grating couplers with low back reflections for rapid prototyping of silicon photonic circuits. *Optics Express*, 22(17):20652, aug 2014. ISSN 1094-4087. doi: 10.1364/OE.22.020652. URL https://www.osapublishing.org/oe/abstract.cfm?uri=oe-22-17-20652.

[89] The Official YAML Web Site. URL http://yaml.org/.

Appendix A

Components List - Automated photonics characterization system

A.0.1 Component list

- 3 axis linear motors - Stepper Motor
  - Micronix VT-50L
  - xy: 50 mm, z: 30 mm
- 2 Manual rotation stages
  - OptoSigma KSP-406M
- Tip-Tilt Stage
  - OptoSigma AIS-40B
- Optical Microscope
  - 12x Zoom lense
  - 2x Adapter tube
- 2x CMOS USB camera
  - Thorlabs Color - DCC1645C
  - Thorlabs Monochrome - DCC1545M
- Custom adaptor plates
- Fibre array
  - Sourced from Fibre Tech Optica
  - Fibres supplied by Le Verre Fluore - ZBLAN MIR6.5/125A

Appendix B

chiprun.py

```python
"""Repeated Chiprun."""
import numpy as np
import argparse
import time

from src.instruments.stages import coordtransform as ct
from src.instruments import Instruments
from src.experiment import Experiment
from src.scans import squarescan, gradient_ascent, opus_scan
from src import database
from src.errors.errors import assert_error, CoordinateCollisionError

# Write a description comment for your chip run by using -c or --comment flags in the command prompt.
# example: python chiprun.py --comment 'this is probably fine'

"""
---------------------------------------------------------------------------------------------------- """
""" User Setup """
# Instruments and experiments are loaded from the config file (.yaml).
inst = Instruments('config_files/manual_align.yaml')

# exp_main is used for general movement, squarescans and gradient scans.
exp_main = Experiment(inst, 'experiment_sqsc', write_to='production database')

# exp_wlsc is a wavelength sweep experiment
exp_wlsc = Experiment(inst, 'experiment_sqsc', write_to='nowhere')

# exp_opus is an opus scan experiment
```

```
exp_opus = Experiment(inst, 'experiment_sqsc', write_to='production database')

# Define your origin device
# origin_device_id = 1670  # lower left CAL structure of top half of Gollum
origin_device_id = 1189  # calibration device in the corner right bottom, middle of the chip itself

# Note this position should change if the wavelength is changed
# origin_device_motor_coordinates = (2.554, -5.109)  # for 1670
origin_device_motor_coordinates = (2.555, 2.894)  # for 1189

"""
------------------------------------------------------------------------------------------
------------ """
""" Get GDS Coords """
""" Whatever you do in the "Get GDS Coords" section, you must end up with a list named "gds_coords"
that has the form: [[x_coord, y_coord, device_id]]. """

# Get all of the device_ids and GDS coordinates for a specific GDS file in the database.
# This is always done.
gds_file = 'Gollum_flattened'
db = database.Database()  # use default user and database as defined within Database class
gds_coords_temp = db.get_chip_gds_coords(gds_file)
gds_origin_x, gds_origin_y = db.get_device_gds_coords(origin_device_id)
db.close()

# Select which filtering option you want to specify the devices you want to measure.
# Set "option" to the option number you want to run. Some options require
# parameters to be set (e.g. xmin in option 2).
# DO NOT change the logic in these options. If you need other logic, create
# a new option!
option = 2

# Option 1: do the whole chip.
if option == 1:
    gds_coords = gds_coords_temp

# Option 2: specify a range of x-coordinates and/or y-coordinates to only measure
# devices with GDS coordinates that fall in these ranges.
if option == 2:
    xmin = -3.485
```

```
66      xmax = 4.712
67      ymin = -3.256
68      ymax = 4.502
69      gds_coords = [coord for coord in gds_coords_temp if ((float(coord[0]) >
        ↪  xmin and float(coord[0]) < xmax)
70                                                          and
                                                            ↪  (float(coord[1])
                                                            ↪  > ymin and
                                                            ↪  float(coord[1])
                                                            ↪  < ymax))]
71
72  # Option 3: specify a list of GDS coordinates (e.g. loaded from a file).
73  if option == 3:
74      example_list = [[0.365, 0.182], [0.265, 0.352]]
75      gds_coords = [coord for coord in gds_coords_temp if [float(coord[0]),
        ↪  float(coord[1])] in example_list]
76
77  # Option 4: specify a list of device_ids (e.g. loaded from a file).
78  if option == 4:
79      example_list = list(range(1, 16, 1))
80      # example_list = [91, 91, 1, 91, 151, 91, 101, 101, 11, 101, 161, 101,
        ↪  191, 191, 1, 191, 389, 191]
81      gds_coords = [coord for coord in gds_coords_temp if coord[2] in
        ↪  example_list]
82
83  # Option 5: get all the devices that have a particular parameter value.
84  if option == 5:
85      param_key = 'blocknumber'
86      param_value = '7'
87
88      db = database.Database()  # use default user and database as defined
        ↪  within Database class
89      gds_coords = [coord for coord in gds_coords_temp if
        ↪  db.device_has_param_value(coord[2], param_key, param_value)]
90      db.close()
91
92  # Option 6: get all the devices with a particular type, or code.
93  if option == 6:
94      # If you are not using one of these parameters, set it to None.
95      device_type = 'cal'
96      device_code = None
97
98      gds_coords = []
99      db = database.Database()  # use default user and database as defined
        ↪  within Database class
100     for coord in gds_coords_temp:
101         device_data = db.query_from_device([coord[2]])
```

```
102         if (((device_data[0][4] == device_type) or device_type is None) and
103                 ((device_data[0][5] == device_code) or device_code is
                    ↪ None)):
104             gds_coords.append(coord)
105     db.close()
106
107 """
    ↪ ----------------------------------------------------------------------------
    ↪ ---------- """
108 """ User Variables """
109
110 # Number of times to repeat the chiprun
111 num_of_repeats = 1
112
113 # The hold time (in seconds) of the detector before a refill is needed and
    ↪ the script pauses.
114 hold_time = 4*60*60
115
116 # The database sample id of the sample being measured.
117 sample_id = 3
118
119 # Set the resolution (IN MILLIMETRES, mm) of the squarescans and gradient
    ↪ ascent.
120 sqsc_step = 0.004
121 grad_step = 0.001
122
123 # The operating z-coordinate motor position. This is an ABSOLUTE motor
    ↪ position,
124 # and IS NOT RELATIVE to the sample.
125 # Millimetres (mm)!
126 set_z = 20.23
127
128 # Starting angle offset (chip rotation to stages).
129 # Angle is in RADIANS (rad)
130 start_beta = 0.0034 + 3.14/2
131
132 # The size of the squarescans (in mm) used to find devices.
133 sqsc_size = 0.020
134
135 # Do a fine gradient scan?
136 fine = False
137
138 # Peck distance - how far (in mm!) up to raise the z-stage while pecking.
139 # Currently must be negative for our stages (the more positive the
    ↪ z-coordinate
140 # of the stage is, the smaller the distance between the chip and
    ↪ measurement
```

```
141 # optics)
142 peck_distance = 0.2
143 peck_distance = -1*abs(peck_distance)
144
145 # Parameters for wavelength scan.
146 # Wavelength is determined by the laser's "set point".
147 # Set point is in the laser-specific coordinate, shown below.
148 # "Laser" | "Set Parameter"
149 # ITC4001 | Current (amps)
150 # SRS LDC500 | Current (amps)
151 # IPG | Stepper Motor Position (mm)
152 wlscan = False  # If True, do_wavelength_sweep() is called.
153 start_sp = 0  # Starting set point.
154 stop_sp = 0  # End set point for the scan.
155 sp_step_size = 0  # The step size
156 return_sp = None  # The laser will be returned to the set point "return_sp"
    ↪ after the scan is
157 # finished. Leave as None to use the laser's current set point (at start of
    ↪ scan).
158
159 # Is a brukerscan being used?
160 # brukerscan = True implies "Do a bruker scan!"
161 brukerscan = True
162 bruker_start_wn = 0  # Bruker start wavenumber (cm^-1) for Bruker scan
163 bruker_stop_wn = 0  # Bruker stop wavenumber (cm^-1) for Bruker scan
164 bruker_res_wn = 0  # Bruker resolution (wavenumber, cm^-1)
165
166 """
    ↪ ----------------------------------------------------------------------------------
    ↪ ---------- """
167 """
    ↪ ----------------------------------------------------------------------------------
    ↪ ---------- """
168 """
    ↪ ----------------------------------------------------------------------------------
    ↪ ---------- """
169 """ Main logic """
170 # Parse an eventual --comment flag
171 parser = argparse.ArgumentParser()
172 parser.add_argument('-c', dest='run_desc', type=str, help='description for
    ↪ the chiprun')
173 parser.add_argument('--comment', dest='run_desc', type=str,
    ↪ help='description for the chiprun')
174 args = parser.parse_args()
175 run_desc = args.run_desc
176
```

```
177 # Get a new run_id. All writes to the Scan table in this script will have
    ↪ this same run_id.
178 # run_desc is populated by using "-c" when calling the script (e.g. python
    ↪ chiprun.py -c 'run description')
179 # run_desc can be None and this is fine - a record in the Run table is
    ↪ still added and a new run_id is
180 # obtained.
181 db = database.Database()  # use default user and database as defined within
    ↪ Database class
182 # Create a record in the Run table and get the run_id.
183 run_id = db.generate_run(run_desc)
184 db.close()
185 print('Starting run with run_id = ' + str(run_id))
186
187
188 # Get the stage for movement.
189 stages = exp_main.instruments.stages
190 stage_name = exp_main.s1_instrument_name
191 stage = getattr(stages, stage_name)
192 assert_error((set_z >= stage.zstage.limit[0]) and (set_z <=
    ↪ stage.zstage.limit[1]),
193              CoordinateCollisionError('set_z value outside of stage
                 ↪ bounds!'))
194
195 # Get the current position.
196 curr_x = stage.get_position_x()
197 curr_y = stage.get_position_y()
198
199 # Move to the starting z position.
200 stages.move_absolute(stage_name=stage_name, axis='z', pos=set_z)
201 curr_z = stage.get_position_z()
202
203
204 # Variable initialization and checking.
205 beta = np.zeros(len(gds_coords))
206 origin_x = origin_device_motor_coordinates[0]
207 origin_y = origin_device_motor_coordinates[1]
208 beta_mean = start_beta
209 sqsc_size = np.abs(sqsc_size)  # make sure the squarescan size is positive
210 sqsc_step = np.abs(sqsc_step)  # make sure step is positive
211 grad_step = np.abs(grad_step)  # make sure step is positive
212
213 # Time the run was started.
214 start_time = time.time()
215
216 # repeat the chiprun 'num_of_repeats' times
217 for jj in range(num_of_repeats):
```

```
218     for ii, coord in enumerate(gds_coords):
219         # Always measure the origin device between device measurements.
220         print('Measuring origin device for reference.')
221         stages.move_relative(stage_name=stage_name, axis='z',
            ↪  dpos=peck_distance)
222         stages.move_absolute(stage_name=stage_name, axis='x', pos=origin_x)
223         stages.move_absolute(stage_name=stage_name, axis='y', pos=origin_y)
224         stages.move_absolute(stage_name=stage_name, axis='z', pos=set_z)
225         sqsc_result = squarescan.do_squarescan_from_centre(exp_main,
            ↪  centre_x=origin_x, centre_y=origin_y,
226
                                                               ↪  length=sqsc_size,
                                                               ↪  step_size=sqsc_step,
227
                                                               ↪  sample_id=sample_id,
228
                                                               ↪  dev_id=origin_device_id,
                                                               ↪  run_id=run_id)
229         sqsc_power = [s[exp_main.exp_dict['v_name']] for s in sqsc_result]
230         sqsc_x = [s[exp_main.exp_dict['s1_name']] for s in sqsc_result]
231         sqsc_y = [s[exp_main.exp_dict['s2_name']] for s in sqsc_result]
232         set_x = sqsc_x[sqsc_power.index(max(sqsc_power))]
233         set_y = sqsc_y[sqsc_power.index(max(sqsc_power))]
234         gradient_ascent.do_gradient_ascent(exp_main,
235                                            set_x, set_y,
                                               ↪  sample_id=sample_id,
                                               ↪  dev_id=origin_device_id,
                                               ↪  run_id=run_id,
236                                            step_size=grad_step,
                                               ↪  maxsteps=20, threshold=100,
                                               ↪  fine=fine, comment='REF',
237                                            normalise=False, p1_name=None,
                                               ↪  p2_name=None,
                                               ↪  sensitivity_name=None)
238         peak_x = stage.get_position_x()
239         peak_y = stage.get_position_y()
240         origin_x = peak_x
241         origin_y = peak_y
242
243         # If specified, run a Bruker scan by using the opusclicker package.
244         if brukerscan is True:
245             # Get the stopper chopper.
246             sources = exp_main.instruments.sources
247             choppa = getattr(sources, 'choppa')
248
249             # Stop the stopper-chopper.
250             choppa.stop_chopper()
```

```
251
252             # Make sure the stopper-chopper is open.
253             choppa.open_chopper()
254
255             # Run the Bruker scans via OPUS window. Will change the focus
                ↪  to the OPUS window and click menu options.
256             opus_scan.do_opusscan(exp_opus, bruker_start_wn,
                ↪  bruker_stop_wn, bruker_res_wn,
257                                   sample_id=sample_id,
                                      ↪  dev_id=origin_device_id,
                                      ↪  run_id=run_id, comment=None)
258
259             # Start up the stopper-chopper again.
260             choppa.start_chopper(100)
261
262         # End of measuring the origin device.
263
264         set_gdsx = float(coord[0])
265         set_gdsy = float(coord[1])
266         dev_id = coord[2]
267         print('Measuring device: ' + str(dev_id))
268         # IF YOU CHANGE THE DIRECTION OF THE FIBER ARRAY YOU MUST CHANGE
            ↪  THE GDS TO MOTOR
269         # FUNCTION
270         set_x, set_y = ct.gds_to_motor(start_beta, set_gdsx -
            ↪  float(gds_origin_x),
271                                        set_gdsy - float(gds_origin_y))
272
273         set_x += float(origin_x)
274         set_y += float(origin_y)
275
276         stages.move_relative(stage_name=stage_name, axis='z',
            ↪  dpos=peck_distance)
277         stages.move_absolute(stage_name=stage_name, axis='x', pos=set_x)
278         stages.move_absolute(stage_name=stage_name, axis='y', pos=set_y)
279         stages.move_absolute(stage_name=stage_name, axis='z', pos=set_z)
280
281         print('Starting Square Scan')
282         print('x: ' + str(set_x) + ', y: ' + str(set_y))
283         sqsc_result = squarescan.do_squarescan_from_centre(exp_main,
            ↪  centre_x=set_x, centre_y=set_y,
284
                                                               ↪  length=sqsc_size,
                                                               ↪  step_size=sqsc_step,
285
                                                               ↪  sample_id=sample_id,
```

```
                                                    dev_id=dev_id,
                                                    ↪ run_id=run_id)

        # end scan returns a list of dictionaries
        # these list comprehensions grab the v (in this case power), x, and
        ↪ y
        # from each data row measurement and put them in their appropriate
        ↪ list
        sqsc_power = [s[exp_main.exp_dict['v_name']] for s in sqsc_result]
        sqsc_x = [s[exp_main.exp_dict['s1_name']] for s in sqsc_result]
        sqsc_y = [s[exp_main.exp_dict['s2_name']] for s in sqsc_result]

        set_x = sqsc_x[sqsc_power.index(max(sqsc_power))]
        set_y = sqsc_y[sqsc_power.index(max(sqsc_power))]

        # move to the suspected device location by pecking
        stages.move_relative(stage_name=stage_name, axis='z',
        ↪ dpos=peck_distance)
        stages.move_absolute(stage_name=stage_name, axis='x', pos=set_x)
        stages.move_absolute(stage_name=stage_name, axis='y', pos=set_y)
        stages.move_absolute(stage_name=stage_name, axis='z', pos=set_z)

        # start the gradient ascent scan to narrow in on the peak
        print('Starting scan sequences')
        gradient_ascent.do_gradient_ascent(exp_main,
                                           set_x, set_y,
                                           ↪ sample_id=sample_id,
                                           ↪ dev_id=dev_id,
                                           ↪ run_id=run_id,
                                           step_size=grad_step,
                                           ↪ maxsteps=20, threshold=100,
                                           ↪ fine=fine, comment=None,
                                           normalise=False, p1_name=None,
                                           ↪ p2_name=None,
                                           ↪ sensitivity_name=None)

        '''
        peak_x = stage.get_position_x()
        peak_y = stage.get_position_y()
        if ii == 0:
            origin_x = peak_x
            origin_y = peak_y
        else:
            beta[ii] = ct.beta(peak_x - origin_x, peak_y - origin_y,
                               set_gdsx - float(gds_origin_x), set_gdsy -
↪ float(gds_origin_y))
        if ii == 0:
```

```
321             # This needs to be here so that the "else" statement does not
    ↪ include the first iteration.
322             # This could have been pass, but we have set it as beta_mean =
    ↪ start_beta so it's clear that
323             # beta_mean has the value in "start_beta" for the first two
    ↪ iterations.
324             beta_mean = start_beta
325         elif ii == 1:
326             beta_mean = beta[ii]
327         else:
328             beta_mean = np.mean(np.asarray(beta[1:ii]))
329         # print('I calculated a beta of : %s' % str(np.rad2deg(beta[ii])))
330         # print('%s: beta mean = %s' % (str(ii),
    ↪ str(np.rad2deg(beta_mean))))
331         '''
332
333         '''
334         # move to peak position by pecking before starting wl scan
335         stages.move_relative(stage_name=stage_name, axis='z',
    ↪ dpos=peck_distance)
336         stages.move_absolute(stage_name=stage_name, axis='x', pos=peak_x)
337         stages.move_absolute(stage_name=stage_name, axis='y', pos=peak_y)
338         stages.move_absolute(stage_name=stage_name, axis='z', pos=set_z)
339
340         if wlscan is True:
341             # If return_sp is not specified, the scan returns the laser to
    ↪ the set point it was
342             # before the scan was called. Otherwise, return to the value
    ↪ specified in
343             # return_sp.
344             if return_sp is None:
345                 # Refresh the internally stored measurements
346                 for refresh_fun in
    ↪ exp_wlsc.refreshing_access_function_list:
347                     refresh_fun()
348                 # Get the s1 measurement (wavelength)
349                 return_sp = exp_wlsc.access_function_list[1]()
350
351             wavelength_sweep.do_wavelength_sweep(exp_wlsc, start_sp,
    ↪ stop_sp,
352                                                  sp_step_size, wait=0.3,
    ↪ comment=None,
353                                                  sample_id=sample_id,
    ↪ dev_id=dev_id,
354                                                  run_id=run_id,
    ↪ return_wl=return_sp)
355         '''
```

```
356         # If specified, run a Bruker scan by using the opusclicker package.
357         if brukerscan is True:
358             # Get the stopper chopper.
359             sources = exp_main.instruments.sources
360             choppa = getattr(sources, 'choppa')
361 
362             # Stop the stopper-chopper.
363             choppa.stop_chopper()
364 
365             # Make sure the stopper-chopper is open.
366             choppa.open_chopper()
367 
368             # Run the Bruker scans via OPUS window. Will change the focus
                ↪  to the OPUS window and click menu options.
369             opus_scan.do_opusscan(exp_opus, bruker_start_wn,
                ↪  bruker_stop_wn, bruker_res_wn,
370                                   sample_id=sample_id, dev_id=dev_id,
                                      ↪  run_id=run_id, comment=None)
371 
372             # Start up the stopper-chopper again.
373             choppa.start_chopper(100)
374 
375         #
376         run_time = time.time() - start_time
377         if run_time > hold_time:
378             input("Refill the detector and then press ENTER.")
379             start_time = time.time()
380 
381 
382 print('End of run with run_id = ' + str(run_id))
```